Politecnico di Torino

ScuDo
Scuola di Dottorato ~ Doctoral School
WHAT YOU ARE, TAKES YOU FAR

Doctoral Dissertation

Doctoral Program in Electrical, Electronics and Communications Engineering

(35^{th}cycle)

Nonlinear Interference Generation in Wideband and Disaggregated Optical Network Architectures

By

Elliot London

******

Supervisor(s):

Prof. Vittorio Curri, Supervisor

Doctoral Examination Committee:

Prof. Georg Rademacher, University of Stuttgart

Dr. Mingming Tan, Aston University

Politecnico di Torino

2023

Declaration

I hereby declare that, the contents and organization of this dissertation constitute my own original work and does not compromise in any way the rights of third parties, including those relating to the security of personal data.

Elliot London
2023

* This dissertation is presented in partial fulfillment of the requirements for **Ph.D. degree** in the Graduate School of Politecnico di Torino (ScuDo).

Acknowledgements

Finishing a PhD is a monumental task that is not possible without crucial support given by friends, family and colleagues. Firstly, I give great thanks to my supervisor Vittorio Curri and my industrial mentor Antonio Napoli for their highly motivated and enthusiastic guidance. Thanks are due to my friends who have helped me through the low points of this project, and have always featured in the high points: the "Juice Crew" in England; Dan Cox, Yasmin Oakley and Tom Loader, who I have shared many incredible experiences with, improving morale when it was needed the most. In a similar way, I thank Alex Edwards, Ed Perring, Jack Belger and Thomas Uglow, who provided laughs, fun, and support, both in person and remotely. No acknowledgement is complete without mention of the support given by my family; I thank my parents and sister for their invaluable emotional support and the relaxation and comfort they provided every time I returned to England.

Many thanks are also given to my colleagues, firstly, within the PLANET team I extend very special thanks to Andrea D'Amico, Bruno Correia, Rasoul Sadeghi, Emanuele Virgillito and Giacomo Borracini, who I have shared many long discussions, moments of relaxation, and frantic deadlines. Additionally, the invaluable technical IT support provided by Marco Bertino during this project cannot be ignored, and was not taken for granted! I also give thanks to the many members of the WON European research group, in particular to Aleksandr Donodin, Mattheus Sena, Caio Santos, Rafael Kraemer, André Nunes and Pratim Hazarika, with whom I shared work environments, ideas, and many fun times. I also express sincere gratitude to Tatiana Kilina and Elisabetta Racca, who gave essential advice and help when faced with countless tasks of impossible bureaucracy, and during a period of sickness within my study.

This project was funded by the European Union's Horizon 2020 research and innovation programme under the Marie Skłodowska-Curie grant agreement 814276.

Abstract

To account for unprecedented rises in capacity and throughput, network operators are seeking to exploit network components and structures in the most cost-effective way possible. One of the most promising methods to achieve this is the expansion of coherent transmission into currently-unused wideband frequencies, which would permit significant capacity increases. Wideband transmission goes hand-in-hand with simultaneous advances in network structures towards open and multi-vendor approaches, which correspond to increasing levels of network disaggregation.

Practical implementation of wideband transmission is currently hindered by a lack of maturity in both modelling and component technologies: frequency-dependent effects such as stimulated Raman scattering (SRS) and nonlinear interference (NLI) require careful consideration, along with the development of reliable and scalable devices. Creation of an accurate and reliable wideband NLI model that also supports disaggregated architectures is therefore a desirable requirement to handle advancements in network technology, but requires that all wavelengths and fiber spans can be modelled independently, across the entire wideband spectrum.

Within this thesis a wideband and disaggregated NLI model is introduced and subsequently validated using modelling tools that include split-step Fourier method (SSFM) simulations and the open-source GNPy library. A wide variety of disaggregated network configurations are investigated, including non-uniform disaggregated and dispersion-managed network segments, demonstrating full spectral and spatial separability of the NLI. Transmission impairments through an experimental set-up are then evaluated, consisting of propagation through a single fiber span over the L-, C-, S-, and E-bands, amplified with a hybrid Raman pump and bismuth-doped fiber amplifier (BDFA). The intricacies of power optimization, amplification, and the interactions between quality of transmission impairments are then discussed, along with techniques for optimising wideband and disaggregated transmission.

List of Publications

During the course of this doctoral program the following articles were published in international journals and conferences. As a result of funding mandates, these publications are fully open source and available to the public.

Peer-Reviewed International Journals

1. Andrea D'Amico, Stefano Straullu, Antonino Nespola, Ihtesham Khan, Elliot London, Emanuele Virgillito, Stefano Piciaccia, Aberto Tanzi, Gabriele Galimberti, and Vittorio Curri. Using machine learning in an open optical line system controller. *Journal of Optical Communications and Networking*, 12(6):C1–C11, 2020

2. Elliot London, Emanuele Virgillito, Andrea D'Amico, Antonio Napoli, and Vittorio Curri. Simulative assessment of non-linear interference generation within disaggregated optical line systems. *OSA continuum*, 3(12):3378–3389, 2020

3. Andrea D'Amico, Stefano Straullu, Giacomo Borraccini, Elliot London, Stefano Bottacchi, Stefano Piciaccia, Alberto Tanzi, Antonino Nespola, Gabriele Galimberti, Scott Swail, and Vittorio Curri. Enhancing lightpath qot computation with machine learning in partially disaggregated optical networks. *IEEE Open Journal of the Communications Society*, 2:564–574, 2021

4. Andrea D'Amico, Elliot London, Bertrand Le Guyader, Florian Frank, Esther Le Rouzic, Erwan Pincemin, Nicolas Brochier, and Vittorio Curri. Experimental validation of gnpy in a multi-vendor flex-grid flex-rate wdm optical transport scenario. *Journal of Optical Communications and Networking*, 14(3):79–88, 2022

5. Andrea D'Amico, Bruno Correia, Elliot London, Emanuele Virgillito, Giacomo Borraccini, Antonio Napoli, and Vittorio Curri. Scalable and disaggregated ggn approximation applied to a c+ l+ s optical network. *Journal of Lightwave Technology*, 2022

6. Elliot London, Andrea D'Amico, Emanuele Virgillito, Antonio Napoli, and Vittorio Curri. Modelling non-linear interference in non-periodic and disaggregated optical network segments. *Optics Continuum*, 1(4):793–803, 2022

7. Rasoul Sadeghi, Bruno Correia, Elliot London, Antonio Napoli, Nelson Costa, João Pedro, and Vittorio Curri. Performance comparison of optical networks exploiting multiple and extended bands and leveraging reinforcement learning. In *2023 International Conference on Optical Network Design and Modeling (ONDM)*, pages 1–6. IEEE, 2023

International Conferences

1. Andrea D'Amico, Elliot London, Emanuele Virgillito, Antonio Napoli, and Vittorio Curri. Quality of transmission estimation for planning of disaggregated optical networks. In *2020 International Conference on Optical Network Design and Modeling (ONDM)*, pages 1–3. IEEE, 2020

2. Andrea D'Amico, Elliot London, Bertrand Le Guyader, Florian Frank, Esther Le Rouzic, Erwan Pincemin, Nicolas Brochier, and Vittorio Curri. Gnpy experimental validation on flex-grid, flex-rate wdm optical transport scenarios. In *Optical Fiber Communication Conference*, pages W1G–2. Optical Society of America, 2021

3. Emanuele Virgillito, Elliot London, Andrea D'Amico, Bruno Correia, Antonio Napoli, and Vittorio Curri. Single-vs. multi-band optimized power control in c+ l wdm 400g line systems. In *2021 Optical Fiber Communications Conference and Exhibition (OFC)*, pages 1–3. IEEE, 2021

4. Andrea D'Amico, Elliot London, Emanuele Virgillito, Antonio Napoli, and Vittorio Curri. Inter-band gsnr degradations and leading impairments in c+ l band 400g transmission. In *2021 International Conference on Optical Network Design and Modeling (ONDM)*, pages 1–3. IEEE, 2021

5. Rasoul Sadeghi, Bruno Correia, Emanuele Virgilito, Elliot London, Nelson Costa, João Pedro, Antonio Napoli, and Vittorio Curri. Optimized translucent s-band transmission in multi-band optical networks. In *2021 European Conference on Optical Communication (ECOC)*, pages 1–4. IEEE, 2021

6. Elliot London, Emanuele Virgillito, Andrea D'Amico, Antonio Napoli, and Vittorio Curri. Observing cross-channel nli generation in disaggregated optical line systems. In *Asia Communications and Photonics Conference*, pages W3B–3. Optical Society of America, 2021

Contents

List of Figures x

List of Tables xxi

Nomenclature xxii

1 Introduction 1

1.1 Motivation 2

1.2 Introduction to Modern Optical Networks 5

1.3 Disaggregated Optical Networks 8

1.4 Wideband Optical Networks 10

1.5 Thesis Outline 13

2 Evaluating Propagation Impairments 15

2.1 Physical Behaviour of Signal Propagation 17

2.1.1 Fiber Loss Coefficient 18

2.1.2 Fiber Dispersion 20

2.1.3 Nonlinear Coefficient 22

2.1.4 Nonlinear Interference 22

2.1.5 Birefringence in Optical Fiber 25

2.1.6 Stimulated Raman Scattering 25

2.2 Recent Works in NLI Modelling . . . 26
2.2.1 Current Limitations . . . 28
2.3 Disaggregated and Wideband NLI Modelling . . . 29
2.3.1 QoT Estimation . . . 30
2.3.2 Abstracting Optical Networks . . . 32

3 Simulation Framework **34**
3.1 Computational Requirements . . . 35
3.2 Workflow and Physical Layer Abstraction . . . 37
3.2.1 OLS Abstraction and Initialisation . . . 37
3.2.2 Propagation Block . . . 40
3.2.3 Digital Signal Processing Block . . . 41
3.3 Configurations . . . 43
3.3.1 Full-Spectrum . . . 43
3.3.2 Single-Channel . . . 44
3.3.3 Pump-and-Probe . . . 45
3.3.4 Limited-Bandwidth . . . 46

4 Modelling Disaggregated Network Segments **48**
4.1 Chapter Overview . . . 50
4.2 Impact of Fiber Span Length . . . 51
4.2.1 Periodic Scenario . . . 52
4.2.2 Single-Span Scenario . . . 54
4.2.3 Full Results for Other Investigated Cases . . . 57
4.3 Impact of Fiber Dispersion . . . 59
4.4 Impact of Residual Dispersion . . . 67
4.4.1 Simulation Settings . . . 68

4.4.2 Investigating XPM Accumulation 70
4.4.3 Dispersive Coherency Factor 80
4.5 Chapter Summary 85

5 Modelling LSCE-Band Experimental Transmission 87
5.1 Wideband Transmission Parameters 87
5.2 Power Optimization 89
5.3 Abstraction of Experimental Set-up 90
5.4 Experimental Parameter Characterisation 92
5.5 Simulation Set-up 96
5.6 Results and Discussion 98
5.6.1 Simulated OSNR Results 99
5.6.2 Simulated NLI Results 100
5.6.3 Comparing GSNRs 101
5.7 Optimising Wideband Amplification 103

6 Conclusion 106
6.1 Future Works 107

References 109

List of Figures

1.1 An illustration showing the three conventional planes of an optical network: the data plane, which consists of the physical layer, the control plane, where routing and wavelength assignment is performed, and the management plane, where the network as a whole is managed. 3

1.2 An abstraction of an optical network architecture: core nodes are connected by OLSs, enabling transmission of optical signals along an LP from a source to a destination. 6

1.3 The typical workflow of an OLS embedded within an optical network. Transponders are used to route signals through ROADMs, and after initial amplification by a terminal amplifier, the signal then passes through N_s fiber span and amplifier pairs. The signal then may pass through a final amplifier, before being received or passing onward through another ROADM node towards its destination. 7

1.4 A diagram showing a region within a disaggregated optical network, with a LP passing through OLSs that are controlled by three different vendors on its way from nodes B to E. 9

1.5 A diagram showing a disaggregated network segment, with nodes labelled A through H and exit links in light blue. In orange, a newly deployed LP is shown, originating at node G and passing through the network to its destination at node C. The presence of an alien wavelength passing through the network simultaneously is shown with a dashed green line. 10

1.6 A schematic of a wideband-enabled OLS as part of a wideband optical network. Transponders are used to route signals through ROADMs, with amplification handled on a per-band basis, as different strategies are required for each band. The signal passes through N_s fiber span and amplifier pairs, before optionally passing through a final amplifier and then into the ROADM to either be received or forwarded towards its destination. 12

2.1 The spectrum of a simulated DWDM signal at 0 dBm of power per channel and a spectral separation of 100 GHz, prior to transmission. 16

2.2 The constellations of (a): a QPSK signal, and (b): a 16-QAM signal, generated by a coherent TRX and before transmission, for a single polarisation. 17

2.3 The total loss in dB / km, α_{dB}, against frequency for the ITU-T G.652D fiber, for the wideband spectrum ranging from the U- to O-bands. 20

2.4 The chromatic dispersion of ITU-T G.652D fiber given in terms of D and β_2, for the wideband spectrum ranging from the U- to O-bands. 21

2.5 The nonlinear coefficient, γ, for ITU-T G.652D fiber over a wideband spectrum that ranges from the U- to O-bands. 22

2.6 The Raman gain profile for the ITU-T G.652D fiber type. 26

3.1 A diagram showing the SSFM methodology. First, a DWDM signal is generated and passes into a portion of the fiber span of length dz_1, where nonlinear and linear operations are performed. The signal then passes into the next portion, with this process repeated until the entire length of the fiber has been traversed. Amplification is then performed and the entire process is repeated as necessary 36

3.2 The workflow of the SSFM library used in this project, with optional stages given in yellow. The four parameter files are provided to the SSFM in JSON format, which is then used to construct the corresponding MATLAB® objects. After initialisation is finished, the signal in DWDM format is propagated through the fiber and amplifier cascade, which at its termination is passed into the RX and DSP model, providing the SNR values of all CUTs. 38

3.3 The constellation of a 16-QAM signal after propagation through 10 spans of SSMF fiber, each followed by a transparent amplifier. . . . 42

3.4 A diagram showing a full spectrum SSFM configuration for one CUT and 10 interfering channels. In this scenario, all channels transmit with an equal power, providing the total SPM and XPM impairments. 44

3.5 A diagram showing how the SSFM operates when in single channel mode, where only the CUT is propagated through the system abstraction, in order to quantify solely the SPM impairment. 45

3.6 A diagram showing the configuration for pump-and-probe simulations, which are used to investigate the XPM contribution. Here, five separate simulations are performed, with one channel turned on at a time, with the third channel currently transmitting. The power of the CUT is lowered with respect to the interfering channels in order to limit SPM contributions. 45

3.7 A diagram showing a limited bandwidth SSFM configuration for one CUT and 10 interfering channels, but with only 3 channels on either side of the CUT considered for estimating the NLI impairment. . . . 46

4.1 An example disaggregated optical network infrastructure. Data is transmitted along LPs that pass through successive OLSs from a source to a destination. A disaggregated network segment is highlighted in orange. 50

4.2 The results of a pump-and-probe simulation campaign along a 40-span periodic OLS, for both pump and probe transmitted with QPSK modulation. Four span length scenarios are presented: L_s =50, 80, 100 and 200 km, all with $D = 16\,\text{ps}/(\text{nm}\cdot\text{km})$. The level given by the GN model is shown as a red line. 53

4.3 The results of a pump-and-probe simulation campaign along a 40-span periodic OLS, for transmission of a pump with 16-QAM modulation, and a probe with QPSK modulation. Four span length scenarios are presented: L_s =50, 80, 100 and 200 km, all with $D = 16\,\text{ps}/(\text{nm}\cdot\text{km})$. The level given by the GN model is shown as a red line. 53

4.4 Two diagrams which show the methodology between the periodic and single-span simulations, respectively. For the former, the signal is propagated through the entire optical system, whereas for the latter, a single span is considered at a time. Before transmission, the signal in the single-span scenario is predistorted by a value equal to transmission through a single span, Θ_{pd}, multiplied by the current considered span index, i. 55

4.5 The results of a pump-and-probe simulation campaign corresponding to 40 fiber-amplifier pairs, with a progressively increasing amount of digital predistortion applied, up to a quantity corresponding to 40 spans. Both pump and probe are transmitted with QPSK modulation. Four span length scenarios are presented: L_s =50, 80, 100 and 200 km, all with $D = 16\,\text{ps}/(\text{nm}\cdot\text{km})$. The level given by the GN model is shown as a red line, and the result for a pump transmitted with Gaussian modulation shown in black. 55

4.6 The results of a pump-and-probe simulation campaign corresponding to 40 fiber-amplifier pairs, with a progressively increasing amount of digital predistortion applied, up to a quantity corresponding to 40 spans. The pump and probe are transmitted with 16-QAM and QPSK modulation formats, respectively. Four span length scenarios are presented: L_s =50, 80, 100 and 200 km, all with $D = 16$ ps / (nm·km). The level given by the GN model is shown as a red line, and the result for a pump transmitted with Gaussian modulation shown in black. 56

4.7 The results of a pump-and-probe simulation campaign corresponding to 40 fiber-amplifier pairs, with a progressively increasing amount of digital predistortion applied, up to a quantity corresponding to 40 spans. Both pump and probe are transmitted with QPSK modulation, separated by 150 GHz. Four span length scenarios are presented: L_s =50, 80, 100 and 200 km, all with $D = 4$ ps / (nm·km). The level given by the GN model is shown as a red line, and the result for a pump transmitted with Gaussian modulation shown in black. 57

4.8 The results of a pump-and-probe simulation campaign corresponding to 40 fiber-amplifier pairs, with a progressively increasing amount of digital predistortion applied, up to a quantity corresponding to 40 spans. Both pump and probe are transmitted with QPSK modulation, separated by 150 GHz. Four span length scenarios are presented: L_s =50, 80, 100 and 200 km, all with $D = 8$ ps / (nm·km). The level given by the GN model is shown as a red line, and the result for a pump transmitted with Gaussian modulation shown in black. 58

4.9 The results of a pump-and-probe simulation campaign including the periodic (solid line) and single-span (dashed line) scenarios. Both pump and probe are transmitted with QPSK modulation, separated by 300 GHz. Four span length scenarios are presented: L_s =50, 80, 100 and 200 km, all with $D = 4$ ps / (nm·km) The level given by the GN model is shown as a red line, and the result for a pump transmitted with Gaussian modulation shown in black. 58

4.10 The results of a pump-and-probe simulation campaign including the periodic (solid line) and single-span (dashed line) scenarios. Both pump and probe are transmitted with QPSK modulation, separated by 300 GHz. Four span length scenarios are presented: L_s =50, 80, 100 and 200 km, all with $D = 8\,\mathrm{ps/(nm{\cdot}km)}$ The level given by the GN model is shown as a red line, and the result for a pump transmitted with Gaussian modulation shown in black. 59

4.11 The gradient of the $\mathrm{SNR_{NL}}$ accumulation, $\Delta\,\mathrm{SNR_{NL}}$, in Scenario 1, for a single propagating channel. The boundaries of the three OLSs are highlighted with dashed lines, and an implementation of the disaggregated GN model is shown with the blue dashed-dotted lines. 61

4.12 The gradient of the $\mathrm{SNR_{NL}}$ accumulation, $\Delta\,\mathrm{SNR_{NL}}$, in Scenario 1, for 5 selected pump-and-probe simulations. The boundaries of the three OLSs are highlighted with dashed lines, and an implementation of the disaggregated GN model is shown for each pump, with dashed-dotted lines with colours that correspond to the pumps that they are modelling. 63

4.13 The gradient of the $\mathrm{SNR_{NL}}$ accumulation, $\Delta\,\mathrm{SNR_{NL}}$, in Scenario 1 for the full-spectrum results, compared to a superposition of all pump-and-probe results. The boundaries of the three OLSs are highlighted with dashed lines, and an implementation of the disaggregated GN model is shown with the blue dashed-dotted lines. . . . 64

4.14 The $\mathrm{SNR_{NL}}$ accumulation in Scenario 1 for the full-spectrum results, compared to a superposition of all pump-and-probe results. OSNR values are calculated by considering ideal amplification, enabling GSNR estimates for the full spectrum, superposition and GNPy simulations. The boundaries of the three OLSs are highlighted with dashed lines. 65

4.15 The gradient of the $\mathrm{SNR_{NL}}$ accumulation, $\Delta\,\mathrm{SNR_{NL}}$, in Scenario 2, for a single propagating channel. The boundaries of the three OLSs are highlighted with dashed lines, and an implementation of the disaggregated GN model is shown with the blue dashed-dotted lines. 65

4.16 The gradient of the SNR_{NL} accumulation, ΔSNR_{NL}, in Scenario 2, for 5 selected pump-and-probes simulations. The boundaries of the three OLSs are highlighted with dashed lines, and an implementation of the disaggregated GN model is shown for each pump, with dashed-dotted lines with colours that correspond to the pumps that they are modelling. 66

4.17 The gradient of the SNR_{NL} accumulation, ΔSNR_{NL}, in Scenario 2 for (a): the full spectrum results, compared to a superposition of all pump-and-probe results. The boundaries of the three OLSs are highlighted with dashed lines, and an implementation of the disaggregated GN model is shown with the blue dashed-dotted lines. 66

4.18 The SNR_{NL} accumulation in Scenario 2 for the full spectrum results, compared to a superposition of all pump-and-probe results. OSNR values are calculated by considering ideal amplification, enabling GSNR estimates for the full spectrum, superposition and GNPy simulations.The boundaries of the three OLSs are highlighted with dashed lines. 67

4.19 A SSFM line configuration that corresponds to a disaggregated optical network segment. This segment is composed of two OLSs that feature in-line dispersion compensation in the form of DCUs. 69

4.20 The ΔSNR_{NL} versus span index for a single interfering pump, with $\Delta f = 150\,\text{GHz}$ and $R_s = 32\,\text{GBaud}$, through a dispersion-managed segment. Results are presented for the entire segment (blue lines), for the final 20 spans (red lines), each span evaluated independently (green lines) and a GN model implementation (black dashed lines), for $\alpha = 0.2\,\text{dB/km}$, $L_s = 80\,\text{km}$, $D_1 = 4\,\text{ps/(nm·km)}$, $D_2 = 16\,\text{ps/(nm·km)}$, and $D_{\text{RES}} = 40\,\text{ps/nm}$. 71

4.21 The ΔSNR_{NL} versus span index for a single interfering pump, with $\Delta f = 150\,\text{GHz}$ and $R_s = 32\,\text{GBaud}$, through a dispersion-managed segment. Results are presented for the entire segment (blue lines), for the final 20 spans (red lines), each span evaluated independently (green lines) and a GN model implementation (black dashed lines), for $\alpha = 0.2\,\text{dB/km}$, $L_s = 80\,\text{km}$, $D_1 = 16\,\text{ps/(nm·km)}$, $D_2 = 4\,\text{ps/(nm·km)}$, and $D_{\text{RES}} = 40\,\text{ps/nm}$. 71

4.22 The $\Delta\text{SNR}_{\text{NL}}$ versus span index for a single interfering pump, with $\Delta f = 150\,\text{GHz}$ and $R_s = 32\,\text{GBaud}$, through a dispersion-managed segment. Results are presented for the entire segment (blue lines), for the final 20 spans (red lines), each span evaluated independently (green lines) and a GN model implementation (black dashed lines), for $\alpha = 0.2\,\text{dB/km}$, $L_s = 80\,\text{km}$, $D_1 = 4\,\text{ps/(nm·km)}$, $D_2 = 16\,\text{ps/(nm·km)}$, and $D_{\text{RES}} = 80\,\text{ps/nm}$. 73

4.23 The $\Delta\text{SNR}_{\text{NL}}$ versus span index for a single interfering pump, with $\Delta f = 150\,\text{GHz}$ and $R_s = 32\,\text{GBaud}$, through a dispersion-managed segment. Results are presented for the entire segment (blue lines), for the final 20 spans (red lines), each span evaluated independently (green lines) and a GN model implementation (black dashed lines), for $\alpha = 0.2\,\text{dB/km}$, $L_s = 80\,\text{km}$, $D_1 = 16\,\text{ps/(nm·km)}$, $D_2 = 4\,\text{ps/(nm·km)}$, and $D_{\text{RES}} = 80\,\text{ps/nm}$. 74

4.24 The $\Delta\text{SNR}_{\text{NL}}$ versus span index for a single interfering pump, with $\Delta f = 150\,\text{GHz}$ and $R_s = 32\,\text{GBaud}$, through a dispersion-managed segment. Results are presented for the entire segment (blue lines), for the final 20 spans (red lines), each span evaluated independently (green lines) and a GN model implementation (black dashed lines), for $\alpha = 0.2\,\text{dB/km}$, $L_s = 80\,\text{km}$, $D_1 = 4\,\text{ps/(nm·km)}$, $D_2 = 16\,\text{ps/(nm·km)}$, and $D_{\text{RES}} = 160\,\text{ps/nm}$. 74

4.25 The $\Delta\text{SNR}_{\text{NL}}$ versus span index for a single interfering pump, with $\Delta f = 150\,\text{GHz}$ and $R_s = 32\,\text{GBaud}$, through a dispersion-managed segment. Results are presented for the entire segment (blue lines), for the final 20 spans (red lines), each span evaluated independently (green lines) and a GN model implementation (black dashed lines), for $\alpha = 0.2\,\text{dB/km}$, $L_s = 80\,\text{km}$, $D_1 = 16\,\text{ps/(nm·km)}$, $D_2 = 4\,\text{ps/(nm·km)}$, and $D_{\text{RES}} = 160\,\text{ps/nm}$. 75

4.26 The $\Delta\text{SNR}_{\text{NL}}$ versus span index for a single interfering pump, with $\Delta f = 300\,\text{GHz}$ and $R_s = 32\,\text{GBaud}$, through a dispersion-managed segment. Results are presented for the entire segment (blue lines), for the final 20 spans (red lines), each span evaluated independently (green lines) and a GN model implementation (black dashed lines), for $\alpha = 0.2\,\text{dB/km}$, $L_s = 80\,\text{km}$, $D_1 = 4\,\text{ps/(nm·km)}$, $D_2 = 16\,\text{ps/(nm·km)}$, and $D_{\text{RES}} = 160\,\text{ps/nm}$. 76

4.27 The $\Delta\text{SNR}_{\text{NL}}$ versus span index for a single interfering pump, with $\Delta f = 300\,\text{GHz}$ and $R_s = 32\,\text{GBaud}$, through a dispersion-managed segment. Results are presented for the entire segment (blue lines), for the final 20 spans (red lines), each span evaluated independently (green lines) and a GN model implementation (black dashed lines), for $\alpha = 0.2\,\text{dB/km}$, $L_s = 80\,\text{km}$, $D_1 = 16\,\text{ps/(nm·km)}$, $D_2 = 4\,\text{ps/(nm·km)}$, and $D_{\text{RES}} = 160\,\text{ps/nm}$. 76

4.28 The $\Delta\text{SNR}_{\text{NL}}$ versus span index for a single interfering pump, with $\Delta f = 150\,\text{GHz}$ and $R_s = 32\,\text{GBaud}$, through a dispersion-managed segment. Results are presented for the entire segment (blue lines), for the final 20 spans (red lines), each span evaluated independently (green lines) and a GN model implementation (black dashed lines), for $\alpha = 0.15\,\text{dB/km}$, $L_s = 80\,\text{km}$, $D_1 = 4\,\text{ps/(nm·km)}$, $D_2 = 16\,\text{ps/(nm·km)}$, and $D_{\text{RES}} = 160\,\text{ps/nm}$. 77

4.29 The $\Delta\text{SNR}_{\text{NL}}$ versus span index for a single interfering pump, with $\Delta f = 150\,\text{GHz}$ and $R_s = 32\,\text{GBaud}$, through a dispersion-managed segment. Results are presented for the entire segment (blue lines), for the final 20 spans (red lines), each span evaluated independently (green lines) and a GN model implementation (black dashed lines), for $\alpha = 0.15\,\text{dB/km}$, $L_s = 80\,\text{km}$, $D_1 = 16\,\text{ps/(nm·km)}$, $D_2 = 4\,\text{ps/(nm·km)}$, and $D_{\text{RES}} = 160\,\text{ps/nm}$. 77

4.30 The $\Delta\text{SNR}_{\text{NL}}$ versus span index for a single interfering pump, with $\Delta f = 150\,\text{GHz}$ and $R_s = 32\,\text{GBaud}$, through a dispersion-managed segment. Results are presented for the entire segment (blue lines), for the final 20 spans (red lines), each span evaluated independently (green lines) and a GN model implementation (black dashed lines), for $\alpha = 0.2\,\text{dB}/\text{km}$, $L_s = 50\,\text{km}$, $D_1 = 4\,\text{ps}/(\text{nm}\cdot\text{km})$, $D_2 = 16\,\text{ps}/(\text{nm}\cdot\text{km})$, and $D_{\text{RES}} = 160\,\text{ps}/\text{nm}$. 78

4.31 The $\Delta\text{SNR}_{\text{NL}}$ versus span index for a single interfering pump, with $\Delta f = 150\,\text{GHz}$ and $R_s = 32\,\text{GBaud}$, through a dispersion-managed segment. Results are presented for the entire segment (blue lines), for the final 20 spans (red lines), each span evaluated independently (green lines) and a GN model implementation (black dashed lines), for $\alpha = 0.2\,\text{dB}/\text{km}$, $L_s = 50\,\text{km}$, $D_1 = 16\,\text{ps}/(\text{nm}\cdot\text{km})$, $D_2 = 4\,\text{ps}/(\text{nm}\cdot\text{km})$, and $D_{\text{RES}} = 160\,\text{ps}/\text{nm}$. 78

4.32 The $\Delta\text{SNR}_{\text{NL}}$ versus span index for a single interfering pump, with $\Delta f = 300\,\text{GHz}$ and $R_s = 64\,\text{GBaud}$, through a dispersion-managed segment. Results are presented for the entire segment (blue lines), for the final 20 spans (red lines), each span evaluated independently (green lines) and a GN model implementation (black dashed lines), for $\alpha = 0.2\,\text{dB}/\text{km}$, $L_s = 80\,\text{km}$, $D_1 = 4\,\text{ps}/(\text{nm}\cdot\text{km})$, $D_2 = 16\,\text{ps}/(\text{nm}\cdot\text{km})$, and $D_{\text{RES}} = 160\,\text{ps}/\text{nm}$. 79

4.33 The $\Delta\text{SNR}_{\text{NL}}$ versus span index for a single interfering pump, with $\Delta f = 300\,\text{GHz}$ and $R_s = 64\,\text{GBaud}$, through a dispersion-managed segment. Results are presented for the entire segment (blue lines), for the final 20 spans (red lines), each span evaluated independently (green lines) and a GN model implementation (black dashed lines), for $\alpha = 0.2\,\text{dB}/\text{km}$, $L_s = 80\,\text{km}$, $D_1 = 16\,\text{ps}/(\text{nm}\cdot\text{km})$, $D_2 = 4\,\text{ps}/(\text{nm}\cdot\text{km})$, and $D_{\text{RES}} = 160\,\text{ps}/\text{nm}$. 79

4.34 The plot of the correlation factor, C_{ij}, against $\theta_{\text{span}}^2\theta_{\text{eff}}$, which quantifies the behavior of the XPM accumulation depending upon the scaled fiber parameters, for $\Delta f = 150\,\text{GHz}$. Three different residual dispersion values are shown; $D_{\text{RES}} = 40$, 80 and $160\,\text{ps}/\text{nm}$ are given by the blue, orange and green dots, respectively. 82

4.35 The plot of the correlation factor, C_{ij}, against $\theta_{\text{span}}^2 \theta_{\text{eff}}$, which quantifies the behavior of the XPM accumulation depending upon the scaled fiber parameters, for $\Delta f = 300\,\text{GHz}$. Three different residual dispersion values are shown; $D_{\text{RES}} = 40$, 80 and 160 ps / nm are given by the blue, orange and green dots, respectively. 83

4.36 A closer view of the dense region of interest centered about the origin within Fig. 4.34. 83

4.37 A closer view of the dense region of interest centered about the origin within Fig. 4.35. 84

5.1 An abstraction of the experimental set-up used for L-, C-, S-, E-band transmission. 91

5.2 The loss coefficients, α, of the SMF and IDF types for the wideband spectral region under consideration. 93

5.3 The group velocity dispersion, β_2, of the SMF and IDF types for the wideband spectral region under consideration. 94

5.4 The nonlinear coefficient, γ of the SMF and IDF types for the wideband spectral region under consideration. 94

5.5 The reference Raman gain coefficient, g_0, corresponding to the Raman gain at a reference frequency, $f_{\text{ref}} = 203.9\,\text{THz}$, for the SMF and IDF types for the wideband spectral region under consideration. 95

5.6 The gain and NF profiles calculated with the hybrid amplifier model, across the wideband spectral region under consideration. 96

5.7 The power profile, $\rho(z, f)$, of the propagated signal shown at the input of the line, and after each optical element. 99

5.8 The OSNR and SNR_{NL} values after propagation and amplification using the combined L-, C-, S-band Raman amplifier system and the E-band BDFA. 100

5.9 The experimentally achieved SNR and numerically calculated GSNR values after propagation and amplification using the combined L-, C-, S-band Raman amplifier system and the E-band BDFA. 102

List of Tables

4.1 A summary of the two disaggregated network scenarios. Each OLS consists of 5x80 km fiber spans, each followed by a transparent amplifier. 60

5.1 The wavelengths and powers for each of the pumps used within the experimental Raman amplifier. 92

Nomenclature

Roman symbols

$\mathscr{F}$	Fourier transform operator
$\mathscr{F}^{-1}$	Inverse Fourier transform operator
A_{eff}	Fiber effective mode area
B_{ch}	Channel bandwidth
c	Speed of light in a vacuum
C_{∞}	Asymptotic coherent accumulation coefficient
C_N	Nth span coherent accumulation coefficient
C_{ij}	Coherent coupling factor
D	Fiber dispersion (in ps / (nm·km))
D_{DCU}	DCU-added dispersion
D_{RES}	Residual dispersion (in ps / (nm·km))
f	Frequency
f_c	Channel central frequency
f_p	Pump frequency
f_s	Stokes wave frequency
f_{ref}	Dispersion reference frequency

G	Amplifier gain
g_0	Reference Raman gain
g_R	Raman gain coefficient
h	Planck constant
k_{pol}	Pump-Stokes polarisation mode difference
L_{eff}	Fiber effective length
L_s	Fiber span length
M	Modulation format order
n_2	Nonlinear fiber index
n_p	PRBS polynomial degree
N_s	Number of spans
P_{ASE}	ASE noise power
P_{ch}	Channel power
P_{CUT}	Channel under test power
P_{NLI}	NLI noise power
P_λ	Channel power at a wavelength λ
R_s	Symbol rate

Greek symbols

α	Optical loss (fiber attenuation)
α_{dB}	Total optical loss (fiber attenuation), in dB / km
β	Fiber dispersion (in s^2 / m)
β_2	2nd-order fiber dispersion (group velocity dispersion)
β_3	3rd-order fiber dispersion (group velocity dispersion gradient)

β_{RES} Residual dispersion (in s^2 / m)

$\Delta\eta$ NLI efficiency gradient

η NLI efficiency

γ Fiber nonlinearity coefficient

γ_R Raman gain coefficient (mode intensity)

$\imath$ Imaginary unit

λ Wavelength

λ_{ref} Fiber reference wavelength

μ Equalizer adaptation coefficient

ρ Gain/loss profile

σ_i Inherent XPM Contribution for span index i

θ Asymptotic accumulation coefficient

θ_{eff} Effective theta

Θ_{pd} Signal predistortion

θ_{span} Fiber span residual dispersion coefficient

ζ Amplifier noise figure profile

Acronyms & Abbreviations

ADC Analog-to-Digital Converter

API Application Programming Interface

ASE Amplified Spontaneous Emission

AWGN Additive White Gaussian Noise

BDFA Bismuth-Doped Fiber Amplifier

BVT Bandwidth Variable Transponder

CPE Carrier Phase Estimator

CPU Central Processing Unit

CUT Channel Under Test

DAC Digital-to-Analog Converter

DCU Dispersion Compensation Unit

DP Dual Polarization

DSP Digital Signal Processing

DWDM Dense Wavelength Division Multiplexing

EDFA Erbium-Doped Fiber Amplifier

EVM Error Vector Magnitude

FFT Fast Fourier Transform

GN Gaussian Noise

GPU Graphics Processing Unit

GSNR Generalized Signal-to-Noise Ratio

GVD Group Velocity Dispersion

IDF Inverse Dispersion Fiber

ILA In-line Amplifier

IMDD Intensity-Modulated Direct Detected

IR Infrared

LMS Least Mean Squares

LOGO Local-Optimisation Global-Optimisation

LP Lightpath

MBT Multi-Band Transmission

NF Noise Figure

NLI Nonlinear Interference

NLSE Nonlinear Schrödinger Equation

OBPF Optical Bandpass Filter

OLS Optical Line System

ONC Optical Network Controller

OOK On-Off Keying

OSA Optial Spectrum Analyzer

OTDR Optical Time-Domain Reflectometer

P2P Point-To-Point

PM Polarization Multiplexed

PMD Polarization Mode Dispersion

PRBS Pseudo-Random Binary Sequence

PSD Power Spectral Density

QAM Quadrature Amplitude Modulation

QoT Quality of Transmission

QPSK Quadrature Phase Shift Keying

ROADM Re-configurable Optical Add-Drop Multiplexer

RWA Routing and Wavelength Assignment

RX Receiver

SDM Spatial-Division Multiplexing

SDN Software-Defined Networking

SMF Single Mode Fiber

SNR Signal-to-Noise Ratio

SPM Self-Phase Modulation

SRS Stimulated Raman Scattering

SSFM Split-step Fourier Method

SSMF Standard Single-Mode Fiber

TDFA Thulium-Doped Fiber Amplifier

TX Transmitter

UV Ultraviolet

VOA Variable Optical Attenuator

WDM Wavelength Division Multiplexing

WSS Wavelength Selective Switch

XPM Cross-Phase Modulation

Chapter 1

Introduction

One of the fundamental enablers of advanced modern technology is the vast global network of optical fibers that enable high-throughput data transfer, providing a heightened level of global inter-connectivity that forms a foundation for innovation and progress. These fibers enable coherent transmission of light over vast distances with minimal losses as part an optical network, thanks to properties such as low dispersion, wide bandwidths, and low-loss amplification methods. Such features permit both short- and long-haul connections with high reliability and performance, which range from metro connections with minimal latency that may be used for speed-critical financial services [14], all the way to trans-continental submarine cable networks that enable responsive global communication [15].

Further innovations in device and network technology are continually being made, expanding internet access and next-generation technologies to even more users, and correspondingly creating a demand for progressively larger amounts of capacity and bandwidth from the underlying infrastructure. As an example, the average WiFi speed tripled between 2018 and 2023 [16], reflecting a significant growth in user demand for high-speed data transmission. This growing demand stems from multiple sources, partly driven by concurrent technological developments in consumer software services, including virtual- and augmented-reality [17], cloud-based computing and storage [18], and 5G-enabled services [19, 20], all of which require large bandwidth allocations. Furthermore, there have been significant advances in public-facing AI-assisted services [21] and steps towards feasible low-latency computing [22, 23] have been made within the last couple of years. Both of these applications also

require large amounts of data transfer, causing additional contributions to network capacity and throughput demands. All of these developments are progressively increasing strains on existing network infrastructures, and as these innovations lead to the development of even more bandwidth-hungry technologies, the result is that current and future technological demands are producing an ever-increasing and accelerating stress upon the requirements of deployed networks.

Going even beyond the predictions given by increasing internet access and technological advances, capacity demands have exceeded all expectations as a result of the COVID-19 pandemic [24], which has caused a mass adoption of cloud-based and remote services starting from 2020, and significantly altering data usage habits worldwide [25, 26]. One particular impact of this pandemic has been the normalisation of remote work [27], with this change persisting even as COVID-19 restrictions have ended [28]. These developments have produced a scenario where networks are facing unprecedented throughput requirements and are placed under record levels of strain [29].

1.1 Motivation

Clearly, the multifaceted problem of meeting network capacity and throughput demands must be addressed swiftly to ensure that digital services remain reliable, fast, and accessible [30]. The simplest solution to these problems would be the installation of additional fiber spans and related infrastructure, directly increasing network capacity by providing more bandwidth for data transmission. Unfortunately, installing new fiber spans is often a prohibitively expensive endeavor [31, 32]; with an estimation of approximately $20,000 required to lay a single kilometer of fiber found in 2018 [33]. The result is that new fiber installation is usually performed when all other alternatives have been exhausted. Consequently, eking out additional capacity and throughput by optimal usage of existing network infrastructure has become a more desirable goal than ever before.

Optimising network capacity and throughput is something which may be approached from many perspectives; transmission quality in the data plane, algorithmic performance in the control plane, and software monitoring in the management plane are all avenues of investigation. A simplified illustration of these layers is shown in Fig. 1.1: the data plane consists of the physical layer where the propagation of the

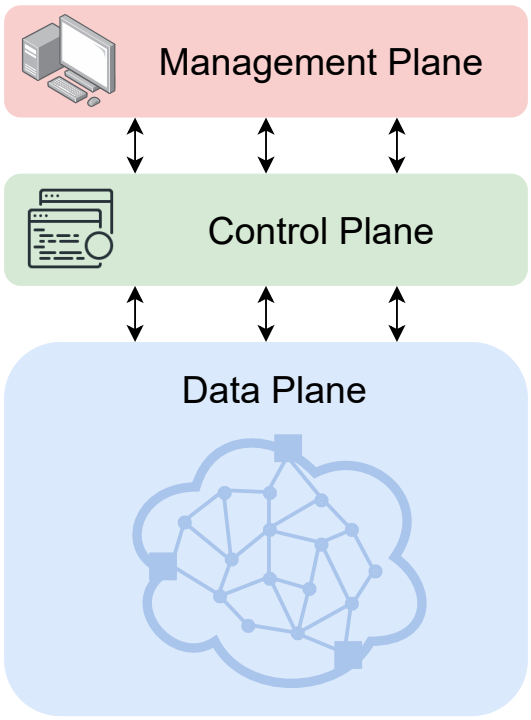

Fig. 1.1 An illustration showing the three conventional planes of an optical network: the data plane, which consists of the physical layer, the control plane, where routing and wavelength assignment is performed, and the management plane, where the network as a whole is managed.

signals takes place, passing between various points from the source to the eventual destination. The control plane is where algorithmic processes take place to determine the routes of these signals and to handle transmission requests. At the top is the management plane, where a unification of optical network controllers and network control software manage the network as a whole.

Achieving maximum possible capacity and throughput requires not only that these planes are optimised individually, but that the interactions between these layers is also orchestrated efficiently. Primarily, this requires that design, transmission and routing of signals is as efficient as possible, and that any uncertainties present in the network are minimised, as these introduce margins that may prevent optimal performance from being achieved. As an example, to prevent any unexpected interruption of service, margins of up to several dB may be imposed if there are doubts about the amount of noise introduced during signal propagation between two points within the network [34]. Naturally, increasing the accuracy of models may

lead to a reduction in margins, as uncertainties concerning propagation are reduced and transmission parameters are optimised [35].

Uncertainty reduction within a network and optimisation of its transmission parameters may afford multiple dB of improvements to the signal quality, but much more than this is needed to tackle the aforementioned capacity requirement problems. The result is that innovations in the structure, transmission capabilities, and management strategies of optical networks are being actively investigated in order to provide the substantial required capacity gains. Of these innovations, three main approaches are being considered: spatial-division multiplexing (SDM), using higher-order modulation formats, and multi-band transmission (MBT). Considering first SDM, this technique motivates the implementation of multi-fiber and multi-mode/multi-core fibers, with the former making use of existing single-mode fibers, and those which have already been deployed but are not in use. Transmission through multi-mode/multi-core fibers unfortunately requires significant improvements to existing infrastructure, including the aforementioned expensive deployment of new fiber in scenarios where deployed fibers do not suit SDM requirements, along with a variety of novel components. Secondly, increasing the modulation format of signals would increase data transfer speeds, with multiple recent works demonstrating transmission that makes use of this technique to provide impressive throughput increases [36, 37]. The main limitation with this approach is that it may not be a long-term solution, as increasing modulation format scales logarithmically with the signal-to-noise ratio (SNR), with the nonlinear Shannon limit as an upper bound [38], leading to diminishing returns.

The third proposal for increasing network capacity without requiring the installation of new fiber spans, which represents the topic of this thesis, is by transmitting data through bands that are currently not in use, in what is known as wideband transmission [39–41]. Historically, these bands were not considered for large-scale transmission, primarily due to concerns about low signal qualities, meaning that technologies for transmission beyond the standard use case of the C-band have remained underdeveloped. If these regions are able to be utilised in a comparable manner to the C-band, massive improvements in capacity and throughput may be enabled. For example, the available bandwidth within the standard C-band is approximately 4.8 THz, and inclusion of the nearest feasible bands of the L-, S-, and E-bands would provide a total bandwidth of approximately 26 THz, or more than five times larger.

Unfortunately, making use of this additional bandwidth is not a simple task, with many obstacles being present. Firstly, as these bands have only recently been considered for large-scale transmission, device technology has not yet fully reached maturity. In particular, the S-band requires alternative amplification techniques to the C- and L-bands, amplification of the E-band is currently under investigation, and the O-band remains unexplored. Some example recent advances have been the development of various doped-fiber amplifiers [42, 43], Raman amplifiers [44], parametric amplifiers [45], and semiconductor optical amplifiers [46], paving the road for feasible transmission across the entire wideband spectrum.

In terms of modelling transmission impairments, significant progress is required; quality of transmission (QoT) is significantly impacted by the presence of high linear losses in other transmission bands, significant stimulated Raman scattering (SRS) effects, a greater quantity of nonlinear interference (NLI) noise that is induced by the Kerr effect, and the interplay between each of these effects [40, 47, 48, 5]. Furthermore, the aforementioned new amplification strategies must also be integrated into the wideband model; each of these devices introduce additional impairments, in turn affecting the power distribution, SRS, and NLI generation, further complicating the generation of transmission impairments in a wideband scenario. The result is that a wide variety of impairments may occur within a wideband transmission scenario, meaning that in-depth investigations of each of these effects are required to enable a model which is both robust and reliable.

Before moving onto how transmission impairments are modelled within wideband and disaggregated networks, first, modern optical network architectures will be outlined, followed by a definition of disaggregated and wideband infrastructures, which forms the content of the rest of this introductory chapter.

1.2 Introduction to Modern Optical Networks

A backbone global infrastructure of interconnected and international optical networks has been formed to provide low-latency and high-volume data transfer. These networks continue to grow in size to match increasing demands, and are by no means unified in terms of components, equipment, or the underlying fiber span infrastructure, but may broadly be described in terms of their common structures. An optical network may be abstracted as a graph, with re-configurable optical add-drop

multiplexers (ROADM)s representing nodes that are linked by optical line systems (OLSs) that serve as edges [49, 50]. An example optical network layout is shown in Fig. 1.2, with edge nodes providing access to computational resources and end users. Most standard OLSs that support coherent transmission consist of successive fiber spans and in-line amplifiers (ILAs), with an example set-up shown in Fig. 1.3. ILAs enable signal power to be regenerated after transmission, recovering losses that are incurred during propagation of the signal through the preceding fiber span, and providing a transparent medium where additional losses due to this amplification are minimal. For the vast majority of optical networks, ILAs are erbium-doped fiber amplifiers (EDFAs), which provide a high level of gain with low noise figure (NF) values. The propagation and amplification process is repeated through the OLS over many tens of kilometers, creating a connection between two nodes.

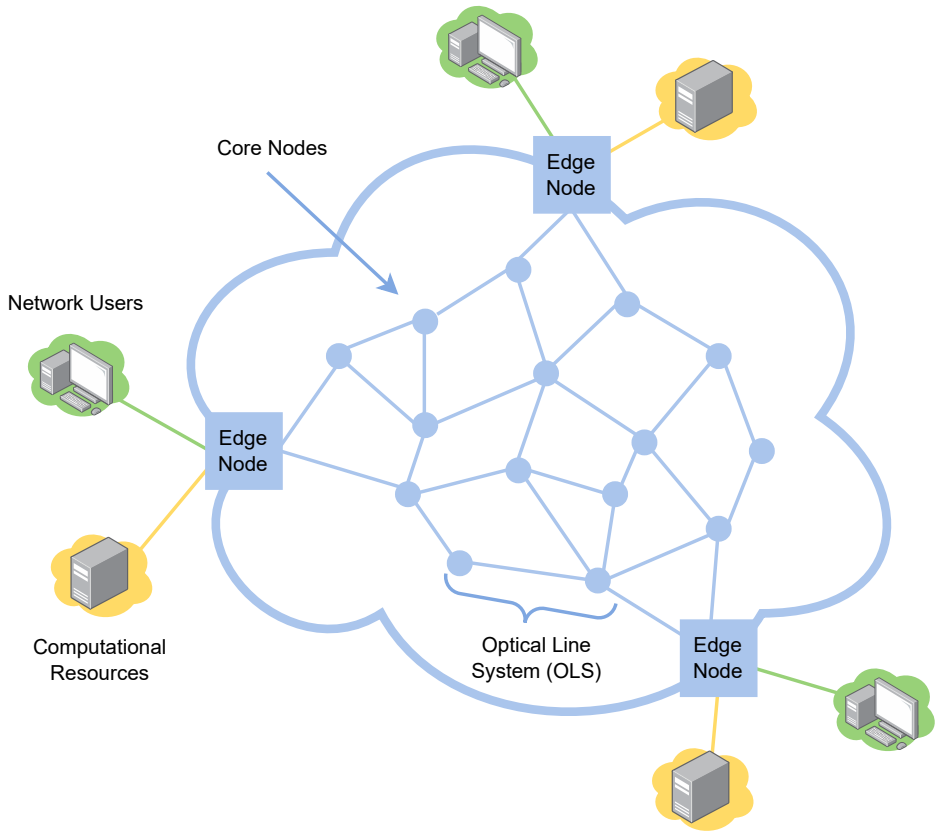

Fig. 1.2 An abstraction of an optical network architecture: core nodes are connected by OLSs, enabling transmission of optical signals along an LP from a source to a destination.

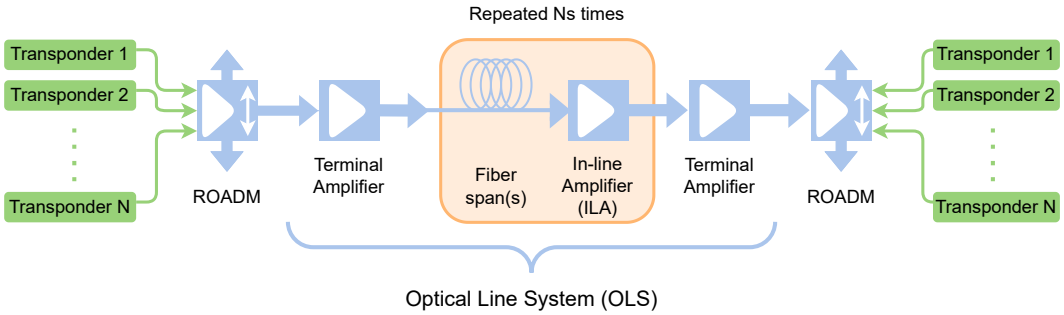

Fig. 1.3 The typical workflow of an OLS embedded within an optical network. Transponders are used to route signals through ROADMs, and after initial amplification by a terminal amplifier, the signal then passes through N_s fiber span and amplifier pairs. The signal then may pass through a final amplifier, before being received or passing onward through another ROADM node towards its destination.

Transmission of signals is performed first by assigning a lightpath (LP) through the network from the source to the destination, which is a process performed using routing and wavelength assignment (RWA) algorithms. These algorithms evaluate path feasibility through available wavelengths, ensuring that QoT is not prohibitively impaired and that the network continues to function tolerably whenever a new LP is assigned. Once this assignment occurs, transmission of the signal is performed using a transmitter (TX), with the signal then propagating through the subsequent OLSs and intermediate nodes, eventually reaching the destination and being received by a receiver (RX), which employs advanced digital signal processing (DSP) algorithms to help mitigate the losses incurred. Other necessary devices include digital-to-analog converters (DACs), analog-to-digital converters (ADCs), connectors, filters, and equalisers, and along with the aforementioned components, all incur unique penalties which further reduce signal quality and must be monitored and compensated for in order to reach the highest possible QoT values.

The standard network architecture described here is typically aggregated, where the network as a whole is managed by a single or small consortium of network providers, simplifying deployment by ensuring that standardisation is enforced. In this scenario, transmission between a source and destination node may therefore be considered as a single link, and modelled by considering a direct abstraction of the route taken. This approach greatly simplifies new LP assignment and QoT modelling, but significantly limits the flexibility and openness of the network, which has led to the aforementioned requests for network disaggregation.

1.3 Disaggregated Optical Networks

Moves towards partial and later full disaggregation within optical networks is a topic of growing academic interest, as this change within network structure and management will help to increase flexibility, reduce costs, more easily enable localised wideband upgrades, and permit the implementation of software-defined networking (SDN) approaches [51–55]. The use of SDN permits the top-level management of a network to be programmable and automated, subsequently enabling a network to perform dynamic functions [56, 57]. Varying levels of SDN are present within most networks, but a shift towards greater levels of disaggregation in turn opens up avenues for a greater level of decision automation. The use of a deeply integrated SDN system affords many benefits over standard approaches, such as faster command execution and a better integration of the control plane [58, 59].

The first step in realising network disaggregation is to move towards a partially disaggregated regime. Under this definition, the OLSs which compose the network are defined as open, which means that device and components parameters are made available to the network as a whole, providing a degree of information transparency and allowing the QoT to be estimated by external tools. These parameters are visible to the control/management planes, but some information may remain confidential, and physical layer management such as assignment of ILA working points remains under the control of OLS controllers.

Partial disaggregation has already been realised in some existing networks with the introduction of wavelength selective switches (WSSs) and bandwidth variable transponders (BVTs) [60], enabling a form of SDN technology where the optimal modulation format can be selected for a given LP. The end goal of full disaggregation is a scenario where device and component information is completely open and available to all network layers, where the SDN controller is able to directly control all devices, acting as an entity which knows all information about every part of the network, with unrestricted access. The result is that optimal network configurations are able to be found much more easily, and reactions to changing network demands are able to be made much faster, increasing network flexibility.

Compared to aggregated networks, disaggregated networks enable a multi-vendor approach, where certain OLSs and network regions may be managed by different vendors who use their own devices, making network-wide standardisation more

difficult and not guaranteed. An example disaggregated optical network with a LP that passes through regions where three different vendors are present is shown in Fig. 1.4. To model the QoT of this LP it is necessary to have detailed information about each crossed OLS between B and E, such as working points of the amplifiers and the fiber parameters. As a result, each OLSs must be considered independently, as an LP such as this passes through a variety of equipment, each of which imparting a variety of different QoT impairments. From a modelling perspective, this statement is the defining characteristic for a disaggregated optical network.

It is important to note that a multi-vendor scenario also enables transmission of so-called alien wavelengths. When considering a region within a disaggregated network, an alien wavelength is defined as a LP which is operated by a third-party vendor originating from outside of the region in question, with a destination that is also potentially unknown [61, 62]. An example network structure where a new LP is deployed through a network which also features an alien wavelength is shown in Fig. 1.5. In addition to complicating wavelength assignment, the presence of alien wavelengths also presents a challenge for QoT estimation, as they mean that the QoT of signals with an unknown history must be quantified. Vendors may also not be willing to share information about the equipment in use within their OLSs, as this may be confidential, private, or unavailable [63], causing further complications.

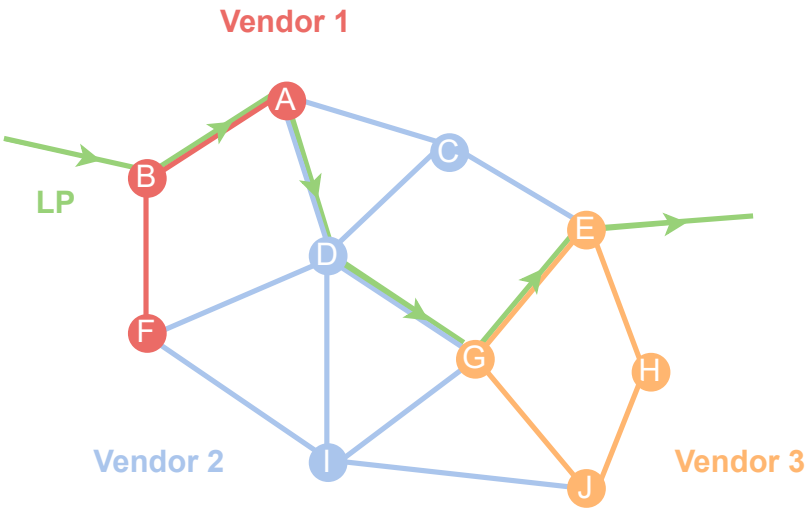

Fig. 1.4 A diagram showing a region within a disaggregated optical network, with a LP passing through OLSs that are controlled by three different vendors on its way from nodes B to E.

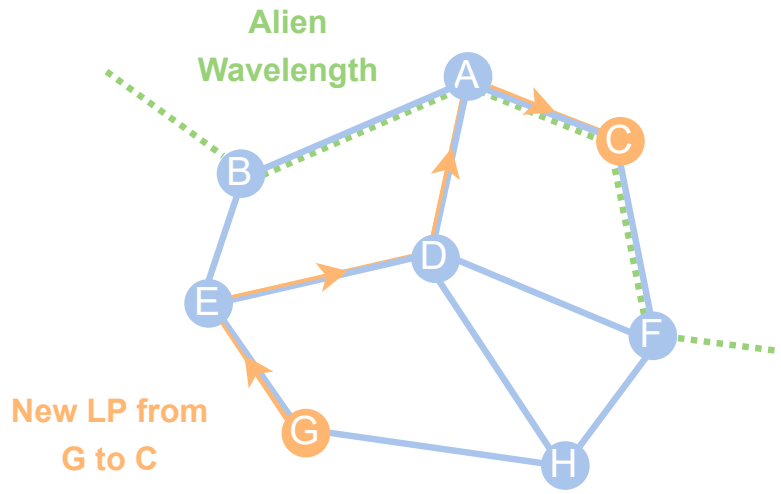

Fig. 1.5 A diagram showing a disaggregated network segment, with nodes labelled A through H and exit links in light blue. In orange, a newly deployed LP is shown, originating at node G and passing through the network to its destination at node C. The presence of an alien wavelength passing through the network simultaneously is shown with a dashed green line.

A consequence of these details is that a disaggregated NLI model must be able to account for inaccuracies that arise from wavelengths with histories that are unknown or lack physical layer information. It is further required that the QoT estimation provided by the model has a high degree of accuracy (to prevent the inclusion of excessive network margins), reliability (to prevent unexpected loss-of-service), and can provide estimations at real-time speeds (to enable integration into a SDN controller). Going beyond these requirements, the progressive disaggregation of optical networks allows wideband transmission upgrades, which further complicate NLI modelling.

1.4 Wideband Optical Networks

The majority of standard bandwidth optical networks transmit signals within the C-band region of the optical spectrum, which has a 4.8 THz total capacity, ranging from 1530 to 1565 nm. This spectral region was originally chosen as it corresponded to a low-loss region within a wide range of easy to produce optical fibers – a good example being the ITU-T G.652D type of standard single mode fiber (SSMF), which is currently the most commonly deployed fiber in the world. Initial investigations

into wideband upgrades have explored use of the L-band; a region bordering the C-band that stretches from 1565 to 1625 nm [64]. Of all the potential wideband transmission candidates, the L-band is the most promising, as it is the most similar to the C-band: amplification is able to be performed with EDFAs that feature high gain and reasonable NF values [65, 66], and linear losses are manageably different to the C-band. Mature commercial technologies are available within the L-band, permitting C-band networks to be progressively upgraded to handle C+L-band transmission [67, 64]. Partial upgrades are already being implemented in limited scenarios within the field [68, 69], concurrent to a large amount of research interest into the logistics, cost and feasibility of these systems.

Widening transmission to include two optical bands (such as in the C+L-band scenario) already presents problems when compared to C-band transmission. Firstly, the effects of SRS may no longer be ignored; this effect transfers power from higher to lower frequencies according to the characteristics of the fiber, channel powers, and frequencies of the transmitting channels. As power is transferred, this in turn has a knock-on effect upon the NLI generation, thereby creating a scenario where using flat input powers across the entire spectrum becomes sub-optimal, with more complex power optimisation procedures required for the best possible QoT values. Secondly, although the C- and L-bands make use of EDFAs, other bands requires use of different amplification sources. For example, in the S-band the two most feasible amplification methods are Raman amplifiers, which may cause disadvantageous power transfer or NLI generation [70, 71], and thulium-doped fiber amplifiers (TDFAs), which do not yet have low NF values, further impacting the overall QoT and requiring optimization [72, 73].

Moving onto the E- and O-bands, bismuth doped fiber amplifiers (BDFAs) become an option, providing an amplification profile with high efficiency and similar gain and NF values as C-band EDFAs, however the presence of higher fiber losses within this region of the spectrum causes complications, and mass production of these devices is not yet available [74–76]. In addition to these problems, transmission within these bands is still in its infancy, with components such as filters, equalisers and switches requiring research, development, and commercial deployment. In particular, transmission experiments are generally still limited in scope to the L-, C-, S-, and E-bands, with feasibility and potential QoT values in the O- and U-bands poorly defined. Furthermore, the zero-dispersion point of commonly-used fiber types, such as ITU-T G.652D SSMF, is located within the O-band, which

requires careful consideration with respect to NLI modelling, and poses a significant challenge besides the lack of device maturity. An example wideband-enabled OLS is shown in Fig. 1.6, where transmission is supported in three different optical bands.

To summarise, the effects of the SRS, the NLI, amplification impairments, and frequency-dependent fiber parameters must all be considered within a wideband model, additionally considering all channels and fiber spans to be independent in order to permit a disaggregated approach. The most accurate method of NLI calculation is by use of split-step Fourier method (SSFM) simulations, which use solutions of the nonlinear Schrödinger equation (NLSE) to compute the signal as it propagates through the fiber in a step-wise manner [77–79]. When the end of the fiber span is reached, it may then be compared to the transmitted signal, and the NLI may be computed. SSFM simulations are computationally expensive, and are typically performed on graphics processing units (GPUs), potentially taking days or weeks to complete the most complex simulations that generally correspond to full spectral load, where every channel is undergoing transmission. As one extends the transmission bandwidth, the complexity of the system under investigation is likewise increased, which increases the amount of time required to perform SSFM simulations to prohibitively large values, depending upon accuracy and resolution requirements. The development of a fast and accurate NLI approximation is highly desirable tool for a wideband and disaggregated transmission scenario, enabling

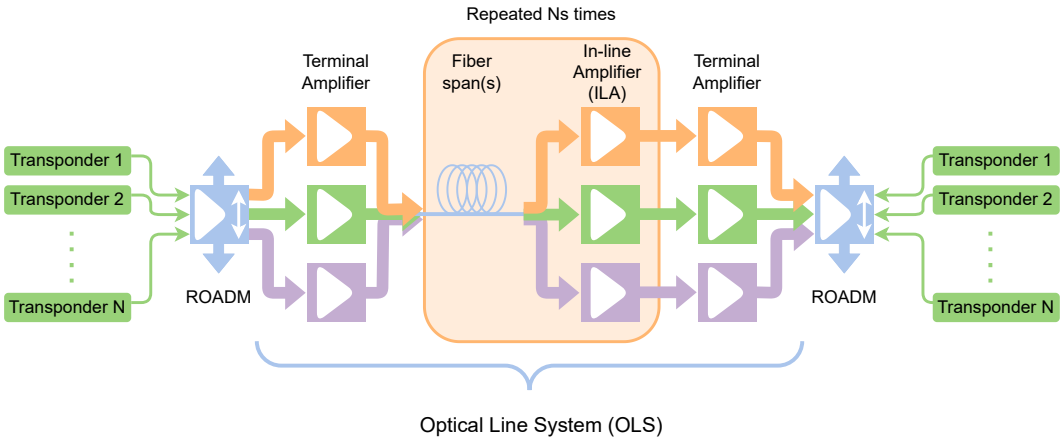

Fig. 1.6 A schematic of a wideband-enabled OLS as part of a wideband optical network. Transponders are used to route signals through ROADMs, with amplification handled on a per-band basis, as different strategies are required for each band. The signal passes through N_s fiber span and amplifier pairs, before optionally passing through a final amplifier and then into the ROADM to either be received or forwarded towards its destination.

planning and monitoring for networks which are have undergone, are undergoing, or will undergo wideband upgrades.

1.5 Thesis Outline

This primary focus of this thesis is upon NLI modelling within disaggregated and wideband optical networks, in order to reliably predict and improve transmission quality, to subsequently enable higher capacities and throughputs without the installation of new fiber spans.

In Chapter 2 a description of the relevant spectral and fiber parameters required for NLI modelling is given, along with the origins and behaviour of the various linear and nonlinear impairments which arise during coherent transmission. The necessary modifications to enable a fully disaggregated and wideband network model are then outlined, followed by the presentation of a wideband and disaggregated model that is used throughout this work, along with the definition of the GSNR, which is used as a top-level QoT estimator.

In Chapter 3 an overview of the SSFM simulation framework used to evaluate signal quality after propagation through wideband and disaggregated network segments is given. As many simulation campaigns have been performed as part of this thesis, the general workflow and structure of the simulation tools is presented, with specific transmission details provided within the corresponding later chapters.

In Chapter 4 the disaggregated NLI model is applied to a variety of disaggregated and dispersion-managed network frameworks in order to perform validation, and to observe the behaviour of the NLI in these regimes. Changes to the fiber parameters within a periodic OLS are investigated to characterise the behaviour of the NLI accumulation, along with the effects of signal Gaussianisation, leading to an upper bound being found for cases where LPs have unknown history. Following this, this methodology is then extended to include two subsets of a disaggregated network infrastructure: for non-periodic segments, where two OLSs with distinct fiber configurations intersect, and for dispersion-managed segments, where the presence of dispersion compensation units (DCUs) induces small amounts of residual dispersion during propagation, affecting the NLI generation.

In Chapter 5 attention is shifted to wideband transmission scenarios, starting from this disaggregated framework. The model is used to estimate the QoT of a wideband transmission experiment performed by collaborators at Aston University, which corresponds to an optimised L-, C-, S-, E-band transmission scenario over a total of 25.8 THz of bandwidth, including 221 coherent channels, additionally making use of a hybrid Raman and BDFA amplifier. A discussion is then initiated on how best to optimise power distribution and amplification in an ultra-wideband scenario such as this one, bearing in mind the complex interactions between the SRS, NLI, and amplification penalties.

In Chapter 6 this thesis is concluded with a summary of the findings and results from the previous sections, along with remarks about future work which can be performed to further refine the disaggregated and wideband model.

Chapter 2

Evaluating Propagation Impairments

To quantify network performance and estimate future LP feasibility it is necessary to evaluate the QoT of LPs that pass through the network, enabling network operators to provide optimised and uninterrupted service [80]. Before establishing a common QoT estimator, some transmission details must first be outlined. For a standard C-band network, propagation over a total bandwidth of up to 4.8 THz is made possible by implementing a wavelength division multiplexed (WDM) grid [81, 82]. Within a WDM grid the LPs and the signals transmitting through them are assigned a spectral region that functions as an occupation slot, with each slot correspond to a channel. To ensure the greatest possible density of information transfer, WDM grids may be set up such that all channels are maximally occupying their respective bandwidths, creating what is known as a dense wavelength division multiplexed grid (DWDM).

An example C-band DWDM grid with 11 channels, spectrally separated by 100 GHz and given in terms of power spectral density (PSD) is shown in Fig. 2.1. The PSD can be simply defined as:

$$\mathrm{PSD} = \frac{P_{\mathrm{ch}}}{B_{\mathrm{ch}}}\,, \tag{2.1}$$

where P_{ch} is the total channel power, and B_{ch} is the channel bandwidth. Within this thesis, a convention where the central frequency of a given channel, f_c, is used, enabling channels to be indexed by an integer, n, where the channel corresponding to $n = 1$ has the lowest central frequency. In the scenario given in Fig. 2.1, there are a total of N_{ch} channels, with each channel having its parameters set by the OLS or SDN controllers, depending upon the level of disaggregation within the network. This

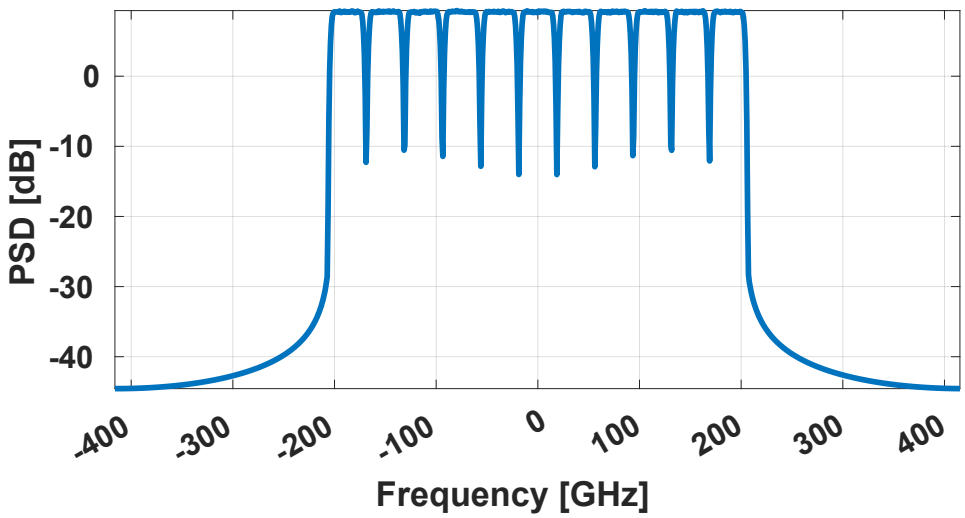

Fig. 2.1 The spectrum of a simulated DWDM signal at 0 dBm of power per channel and a spectral separation of 100 GHz, prior to transmission.

simple example consists of uniform channels, all with equal B_{ch} and symbol rate, R_s, values, whereas in realistic deployment, non-uniform features such as flex-grid, flex-rate implementations and a non-flat power distribution are possible, primarily driven by advances towards disaggregated infrastructures [9, 83, 84]. An assessment on the maximum possible throughput for a given optical network is provided in [85].

Information is transmitted from a source to a destination through the constituent network OLSs by the transmitter, which encodes successive bits into a data stream, which passes into the first fiber span within the OLS. As throughput requirements have risen, so too has the desired information density of the signal; modern transmission standards require dual-polarisation coherent signals, where both the X and Y polarisation states of the signal and the amplitude and phase of the signal are used for encoding. Within certain key metro networks, LPs which make use of direct-detection intensity modulated (IMDD) transmission with on-off keying (OOK) modulation techniques still prevail, often being transmitted alongside coherent signals in a mixed coherent-incoherent network infrastructure [86–88]. For coherent transmission, a variety of modulation formats are used for signal encoding, with common formats including quadrature phase-shift keying (QPSK) and various quadrature amplitude modulation (QAM) formats, such as 8-QAM, 16-QAM, and beyond [89, 90]. These formats encode data upon the amplitude and phase of the signal and may therefore be visualised as a constellation in the complex plane, with examples of ideal QPSK and 16-QAM constellations given in Fig. 2.2.

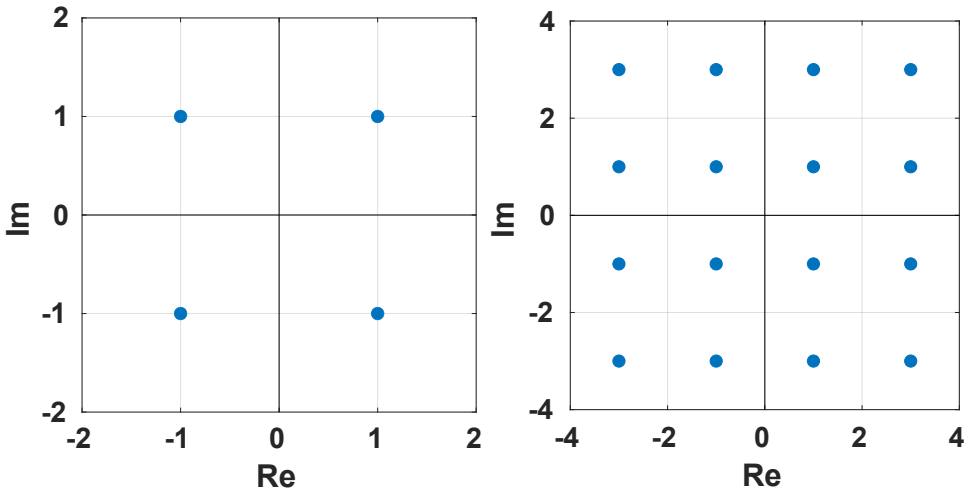

(a) (b)

Fig. 2.2 The constellations of (a): a QPSK signal, and (b): a 16-QAM signal, generated by a coherent TRX and before transmission, for a single polarisation.

2.1 Physical Behaviour of Signal Propagation

To classify the various noise contributors that arise due to signal propagation, it is useful to start by inspecting the dual-polarisation coupled NLSE, which dictates the physical behaviour of an electromagnetic wave (a multiplexed signal) as it propagates through an optical medium (a dispersive fiber span). The dual-polarization coupled NLSE is defined as [91]:

$$\partial_z \psi(z,t) = -\left(\alpha + \frac{\imath\beta}{2}\partial_t^2\right)\psi(z,t) + \imath\gamma|\psi(z,t)|^2\psi(z,t)\,, \tag{2.2}$$

where $\imath$ is the imaginary unit (a convention maintained throughout this thesis), α is the gain/loss coefficient of the fiber, commonly referred to as the fiber attenuation, β is the fiber dispersion, and γ is the fiber nonlinear coefficient. To best describe and inspect these parameters and to break down the general behaviour of the linear and nonlinear parts, the NLSE may be expressed in terms of angular frequency, $\omega = 2\pi f$, by performing a Fourier transform upon t within Eq. 2.2, giving:

$$\partial_z \psi(z,\omega) = -\left(\alpha + \frac{\imath\beta}{2}\partial_\omega^2\right)\psi(z,\omega) + \imath\gamma|\psi(z,\omega)|^2\psi(z,\omega)\,. \tag{2.3}$$

The linear part of Eq. 2.3, $\bar{\psi}$, is found simply by setting $\gamma = 0$:

$$\partial_z \bar{\psi}(z,\omega) = -\left(\alpha + \frac{\imath}{2}\beta\partial_\omega^2\right)\psi(z,\omega)\,, \tag{2.4}$$

which demonstrates that the linear propagation impairments are dictated by the parameters α and β. In the following sections, the linear and nonlinear contributors to Eq. 2.2 will be explained, along with other important effects that are not immediately evident from this equation that also impact QoT.

2.1.1 Fiber Loss Coefficient

The fiber loss coefficient, α, takes into account a variety of effects which directly contribute to the evolution of the signal power profile as it propagates through the fiber. For a given frequency, f, a profile may be created that describes the gain/loss of the fiber along the z axis, $\rho(z,f)$, taking into account a variety of linear loss-inducing effects that are due to the fiber composition and arise from the fiber manufacturing process [92, 93]. Concerning current feasible wideband transmission scenarios that stretch from the L- to the E-bands, the significant linear loss contributors arise from Rayleigh scattering, infrared (IR) absorption, and the absorption peaks of OH^- ions present within the fiber [94]. Less significant contributors include losses due to macrobending within the fiber, and the presence of other ions (such as phosphorous, cadmium, and iron) that enter the fiber core during creation of the preform, and ultraviolet (UV) absorption. These losses may be ignored within our QoT model, as macrobending is minimised in practical use cases by proper fiber management, and UV/other ion contributions are small, and are only significant for frequencies that lie outside of current deployable wideband bandwidths.

The largest linear loss contributor is Rayleigh scattering, which is mainly caused by microscopic variations to the fiber composition along its length and cross-section. These variations in density cause a corresponding change in refractive index, which in turn causes a proportion of photons that propagate through the fiber to be scattered in random directions. Practically, this induces a frequency-dependent loss in signal power [95]. Rayleigh scattering also includes Rayleigh backscattering, which is a subset of this effect that concerns only the photons which travel back towards the TX, and is an effect which is particularly relevant in certain scenarios that make use of Raman pumps/amplification [96, 97].

IR absorption loss is explained by silica glass fiber having inherent absorptive properties in the IR region of the electromagnetic spectrum. Concerning OH^- absorption, during the manufacturing process OH^- ions may be irreversibly absorbed into the fiber core. The result is a large linear loss centered around the OH^- absorption peaks, which lie close to or within parts of the wideband spectrum [98]. Two prominent OH^- peaks are at 1.24 and 1.38μm, with the latter able to impart very large losses within the O- and E-bands, and historically being a major reason why transmission was not undertaken within these bands [99]. Advancing production techniques have led to the creation of fibers with greatly reduced losses due to OH^- peaks; the common ITU-G.652D fiber type features a greatly reduced OH^- peak, with very small loss contributions, and variants such as pure silica core fiber having near-zero loss due to OH^- ions [85].

These various losses may be combined to give a total loss in dB / km, α_{dB}, with use of a parametric model (described in [100]), for a given λ_{ref}:

$$\alpha_{\text{dB}} \approx \alpha_s + \alpha_{\text{IR}} + \alpha_{13} \,, \tag{2.5}$$

where the loss coefficients on the right hand side are, correspondingly; the Rayleigh scattering loss coefficient [101], IR absorption, and the 1.32μm OH^- peak:

$$\alpha_s = A\lambda^{-4} + B \,, \tag{2.6}$$

$$\alpha_{\text{IR}} = K_{\text{IR}} e^{-\frac{C_{\text{IR}}}{\lambda}} \,, \tag{2.7}$$

$$\alpha_{13} = \sum_{a=0}^{3} A_a e^{-\frac{(\lambda-\lambda_a)^2}{2\sigma_a^2}} \,, \tag{2.8}$$

with the parameters A, B, K_{IR}, and C_{IR} providing the weights for the Rayleigh scattering and IR absorption contributors, respectively, and the parameters within the sum of Eq. 2.8 defining the location, amplitude and width of the OH^- peak contributor. These parameters may be determined experimentally, and the separate effects may be isolated by fitting the experimental data according to the relations given above. Consequently, α_{dB} can be quantified, most easily with aid of product data sheets [3, 100, 102]. An example for ITU-T G.652D SSMF fiber is given in Fig. 2.3, with the lowest loss region including the L-, C- and partial S-bands.

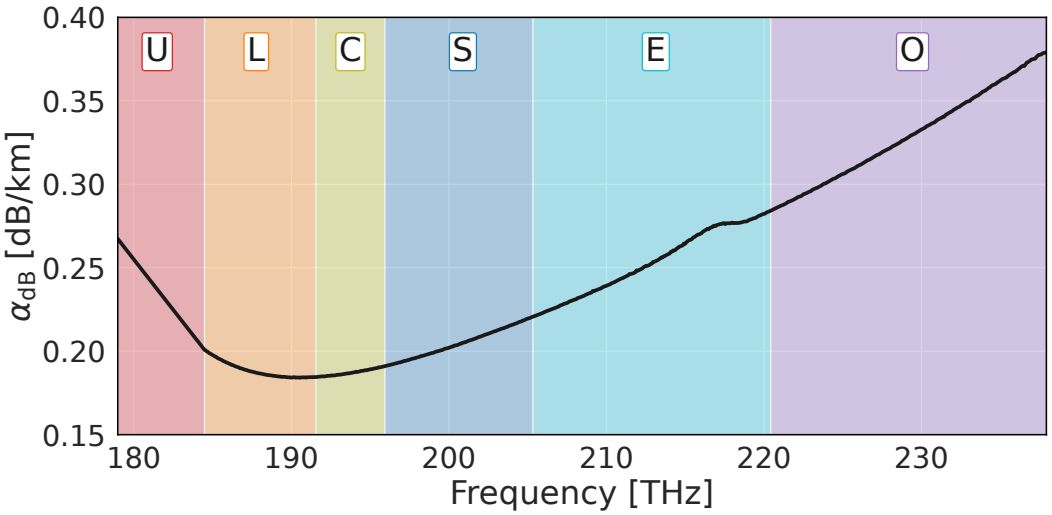

Fig. 2.3 The total loss in dB / km, α_{dB}, against frequency for the ITU-T G.652D fiber, for the wideband spectrum ranging from the U- to O-bands.

2.1.2 Fiber Dispersion

The parameter β quantifies all dispersive effects which take place within the fiber. Dispersive effects arise from the group-velocity dispersion (GVD) of the signal pulse having a frequency dependence, which causes different frequencies of the signal to propagate with different relative speeds within the fiber. The result is that the signal gradually stretches in time, causing neighbouring signals to overlap, which produces a corresponding interference that distorts the signal through pulse broadening. β is most often given as a function of angular frequency, $\omega = 2\pi f$, and a Taylor expansion may be performed about a central frequency, $\omega_0 = 2\pi f_0$, to give its leading-order contributors [5, 91]:

$$\begin{aligned}\beta(\omega) &= \beta_0 + \frac{\partial\beta}{\partial\omega}(\omega-\omega_0) + \frac{1}{2}\frac{\partial^2\beta}{\partial\omega}(\omega-\omega_0)^2 + \frac{1}{6}\frac{\partial^2\beta}{\partial\omega}(\omega-\omega_0)^3 + \cdots \\ &= \beta_0 + \beta_1(\omega-\omega_0) + \frac{1}{2}\beta_2(\omega-\omega_0)^2 + \frac{1}{6}\beta_3(\omega-\omega_0)^3 + \cdots,\end{aligned} \tag{2.9}$$

where β_0, β_1, β_2, and β_3 are the first four leading contributors. The parameter of greatest relevance is β_2, known as the chromatic dispersion parameter, which dictates the interference between neighbouring symbols which occurs as a result of pulse broadening. Values of β_2 may be measured experimentally or obtained from data sheets provided by the fiber manufacturers, who conventionally give β_2 in terms of

the optical pulse wavelength using the dispersion parameter, D, defined as:

$$D = -\frac{2\pi c}{\lambda_2}\beta_2 \,, \tag{2.10}$$

where c is the speed of light in a vacuum. A plot of the D and β_2 parameters for ITU-T G.652D fiber is shown in Fig. 2.4, with dispersion reaching low and eventually negative levels as frequency is increased into the O-band, which has important implications for NLI modelling that are discussed in Sec. 2.1.4.

Dispersion may be compensated for either in-line or at the RX with use of DSP. Rx-side compensation is advantageous for modern coherent transmission, as in-line DCUs are not required, resulting in lower installation requirements and complexity, and avoiding changes in nonlinear contributions that arise from residual dispersion [6, 103]. The topic of residual dispersion as a result of mismatches between DCU and fiber dispersions is described and investigated in further detail in Sec. 4.4.2.

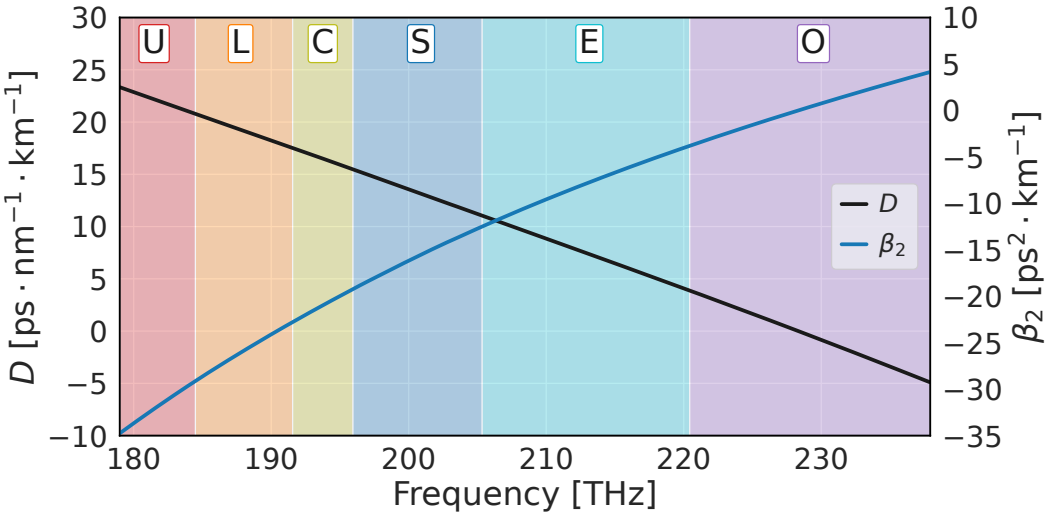

Fig. 2.4 The chromatic dispersion of ITU-T G.652D fiber given in terms of D and β_2, for the wideband spectrum ranging from the U- to O-bands.

2.1.3 Nonlinear Coefficient

Moving onto the nonlinear part of Eq. 2.3, this effect is weighted by the nonlinear coefficient, γ, which is given by:

$$\gamma(\lambda) = \frac{2\pi}{\lambda}\frac{n_2}{A_{eff}}, \tag{2.11}$$

where n_2 is the nonlinear Kerr parameter, and $A_{\text{eff}} = \pi w^2$ is the effective mode area, defined for a Gaussian pulse propagating through the fiber, with w being the field radius/spot size, which depends upon the central wavelength of the pulse and the fiber geometry [104]. A plot of γ for ITU-T G.652D fiber is shown in Fig. 2.5, with the parameter observed to evolve near-linearly and doubling in value between the U- and O-bands, which is significantly less variable than the linear parameters, α and β. The effect of this small, linear change in γ across a wideband spectrum is described in further detail in Sec. 5.1.

2.1.4 Nonlinear Interference

The product $|\psi(z,\omega)|^2\,\psi(z,\omega)$ in Eq. 2.3 gives rise to complex behaviour that characterises the accumulation of the nonlinear interference noise, or NLI noise,

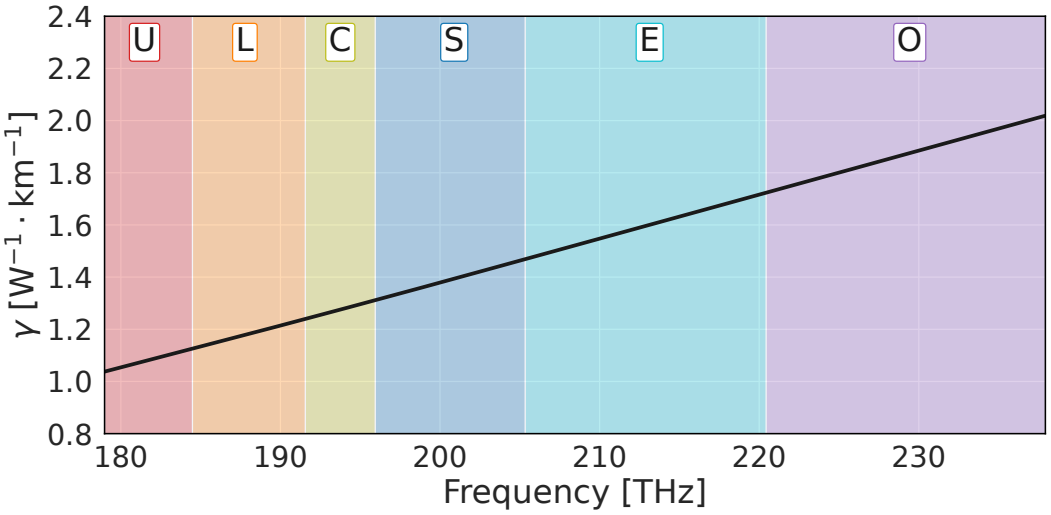

Fig. 2.5 The nonlinear coefficient, γ, for ITU-T G.652D fiber over a wideband spectrum that ranges from the U- to O-bands.

during propagation, most broadly described as the optical Kerr effect [105]. To investigate the behaviour of the NLI it is necessary to solve Eq. 2.3, which can be done using a variety of different approaches, the most common being a perturbation upon the linear solution to Eq. 2.4, which is:

$$\bar{\psi}(z,\omega) = \bar{\psi}(0,\omega)e^{-z\left(\alpha+\frac{\imath}{2}\beta\omega^2\right)} . \tag{2.12}$$

To make effective progress in finding a compact and general solution to Eq. 2.3 for propagating DWDM signals, a key assumption is made that the channels within the WDM grid are additive and white Gaussian noise (AWGN) sources. Practically, this assumption is enabled by treating all noise sources as able to be summed together, with a uniform power across the entire frequency spectrum, and both the noise and signal itself as being Gaussian in shape. From a physical perspective, assuming that the signal is Gaussian in shape is valid after the signal has propagated through a short distance within a dispersive fiber span due to an effect known as Gaussianisation. During this process, which occurs within the first few spans of propagation, the signal is shaped in the constellation plane towards a Gaussian centered about the origin as a result of dispersive effects [106, 107].

Although the additive approach is not entirely accurate when considering the NLI, this loss of accuracy is small and greatly simplifies modelling, which has led to the creation of a family of models known as Gaussian noise (GN) models [106, 108–111]. The original GN model and its various adaptations represented a major breakthrough for NLI modelling, providing accurate approximations of the total NLI for a wide range of scenarios that have been extensively verified [107, 112, 113], with implementations of this model now being widespread and publicly available; we highlight in particular the open-source GNPy repository [114–116]. By inspecting the result of the GN model a posteriori, the contributions to the NLI can be grouped into three categories, depending upon the location of the interferent frequencies of the noise with respect to the channel under test (CUT) [117–120].

Self-Phase Modulation

Firstly, noise originating from the channel interfering with itself is known as self-phase modulation (SPM), scaling with P_{CUT}^2. The most noteworthy feature of the SPM is that it is always present at the location of the CUT, and exhibits coherent

behaviour. This coherency means that the SPM generated at a given span is dependent upon the SPM generated within previously crossed spans, due to a correlation between accumulated phase noise during propagation. The original GN model is completely incoherent, meaning that this effect is not taken into account, resulting in an underestimation of the SPM that worsens proportionally (but not linearly) to the number of crossed fiber spans. Further issues arise when disaggregation is required, as the coherency of a given signal may be difficult to predict accurately if the history or origin point of the signal is unknown. As symbol rates rise, so too does the SPM contribution, with some next-generation transmission scenarios having a dominant SPM contribution [121]. The result is that SPM coherency is expected to become an increasingly important issue to manage as advancements in transmission standards are implemented.

Cross-Phase Modulation

The second type of NLI contributor is cross-phase modulation (XPM), which originates from other channels within the WDM grid interfering with the CUT, and, for a given interferent channel, scales with $P_{\mathrm{CUT}}P_{\mathrm{ch}}^2$. Unlike SPM, under normal circumstances this effect is completely incoherent, meaning that the XPM of a given fiber span is completely uncorrelated with that of the previous fiber spans [122]. The magnitude of the XPM contribution scales with the number of interferent channels and their distances from a given CUT, falling off with an approximately $1/x^2$ relation [5].

Four-Wave Mixing

All other contributions to the NLI are grouped into the classification of other four-wave mixing (FWM) effects. For scenarios where the fiber dispersion is well outside of the low-dispersion regime, which corresponds to most normal operating cases, these contributions are typically negligible [2, 123–125]. In any case, as new bandwidths are explored, there is the potential for transmission through regions where the fiber dispersion approaches zero and FWM effects may be significant, which should be taken into account accordingly. Fig. 2.4 demonstrates that FWM is expected to be relevant when transmission is attempted well within the O-band, and beyond, for SSMF [85].

2.1.5 Birefringence in Optical Fiber

An additional detail that must be mentioned is that optical fiber media exhibit birefringence, whereby the refractive index of the fiber at a given point depends upon the polarisation of the light passing through it [91, 126, 127]. As a result of inevitable small deformities or irregularities within the fiber, the magnitude of the birefringence effect varies throughout the fiber length, acting as a stochastic process – practically, this produces what is known as polarisation mode dispersion (PMD), where the polarisation modes of the signal drift during propagation [128, 129]. This effect complicates transmission and modelling, particularly as current transmission standards make use of two polarisation states, however there are a variety of modern compensation techniques, including RX-side DSP that are able to compensate for it [130, 131].

2.1.6 Stimulated Raman Scattering

One more major effect that contributes to QoT degradation and is not present in solutions which start from Eq. 2.2 is stimulated Raman scattering (SRS). This effect originates from an interaction between the signal photons and the fiber during propagation; some photons undergo inelastic scattering, whereby they are absorbed by the fiber and then re-emitted. As energy is lost during this process, the photons are re-emitted at a lower frequency, which on a macroscopic level manifests itself as a nonlinear shift in signal power from high to low frequencies. This power transfer causes a corresponding change in the amount of NLI that is generated, creating a complex and dynamic interaction between these two effects within a wideband transmission scenario. In fact, as the transmission bandwidth is extended, the SRS quickly becomes the dominant contributor to inter-band power loss even for a C+L-band scenario [11], meaning that this cannot be ignored when the transmission bandwidth is enlarged beyond the C-band.

The efficiency of the power transfer between two frequencies within a WDM grid is given by the Raman gain coefficient, g_R, which may be calculated using [132]:

$$g_R(\Delta f, f_p) = k_{\text{pol}} g_0(\Delta f, f_{\text{ref}}) \frac{f_p}{f_{\text{ref}}} \frac{A_{\text{eff}}(\Delta f, f_{\text{ref}})}{A_{\text{eff}}(\Delta f, f_p)} , \tag{2.13}$$

where f_p and f_s are the frequencies of the pump and Stokes wave, respectively, that correspond to the higher and lower frequencies, with a frequency shift, $\Delta f = f_p - f_s$. The variable k_{pol} quantifies the polarization state differences between the pump and the Stokes wave, and g_0 is the reference Raman gain measured at f_{ref}, given by:

$$g_0(\Delta f, f_{\text{ref}}) = \frac{\gamma_R(\Delta f, f_{\text{ref}})}{\Delta f, f_{\text{ref}}}\,, \tag{2.14}$$

where γ_R is the Raman gain coefficient in terms of mode intensity. The Raman efficiency for a typical SSFM fiber is given by a characteristic function shown in Fig. 2.6, with a peak efficiency of $\approx 0.38\,\text{W}^{-1}\,\text{km}^{-1}$ at ≈ 15 THz.

2.2 Recent Works in NLI Modelling

Since the widespread proliferation of the GN model, there have been many attempts to either improve, reformulate or enhance it to better suit the needs of more advanced use cases, such as for disaggregated or wideband network architectures, alternative amplification strategies, or to include the effects of SRS [133]. One of the first developments was the creation of the enhanced Gaussian noise (EGN) model, which made several corrections to the calculations of the original to help improve accuracy [125, 134], and paving the way for a variety of closed-form approximations,

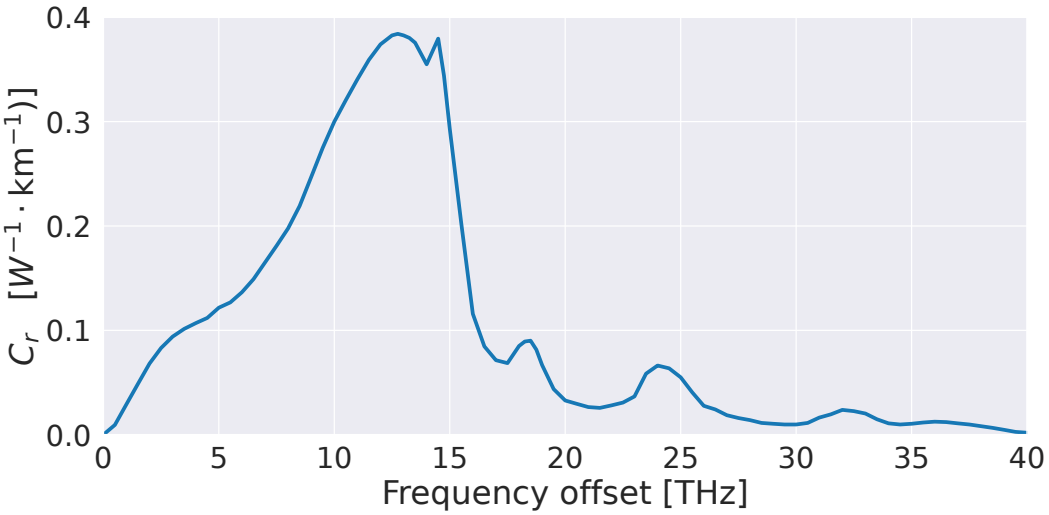

Fig. 2.6 The Raman gain profile for the ITU-T G.652D fiber type.

which feature greatly reduced computational complexity [135–137]. Shortly after came the development of the generalized Gaussian noise (GGN) model [138, 111], which permitted the GN model to be used in the case of varying loss parameters, distributed amplification, or the inclusion of Raman amplification, being verified experimentally for the latter in [139].

Besides the GN model approach, a variety of other, independent model implementations have been derived. In [120], the collisions between propagating signal pulses is considered, which is used to provide insights into the mechanism of NLI generation, with these results providing enhancements for the GN model, as suggested in [140]. In [141], a perturbative approach upon the fiber dispersion is performed, providing superior accuracy to GN model approaches in the low-dispersion regime. Numerical approaches to the nonlinear Schrödinger equation have also been considered, two examples being [142] and [143], with this technique often providing extremely accurate results. Unfortunately, as commented upon in [144] and explained in further detail in Chapter 3, detailed numerical solutions often cause computation time issues. In particular, when considering wideband networks even only spanning the C, L-, and S-bands, full-spectral load transmission scenarios may potentially take weeks to complete for just a single spectral configuration. Finding an approach which reduces this computational overhead while having a minimal impact on model accuracy is therefore highly desirable.

The first step on the path to wideband transmission and modelling is the shift from C-band to C+L-band networking. In [145] it is shown that for some C-band networks it is possible to more than double the available capacity by adding transmission through the L-band, showing that these upgrades offer attractive advantages over standard C-band transmission. As mentioned in Sec. 2.1.6, managing SRS is crucial in a wideband scenario, and this was notably approached through the development of the ISRS GN model, which includes the Raman effect within the NLSE, and makes assumptions such as a triangular approximation of the Raman profile, enabling a closed-form solution [47, 146–148], with further developments integrating a Raman amplifier model [149]. These closed form solutions achieve near-real-time accuracy, are simple to implement, and have been validated experimentally for bandwidths stretching from the L-band to parts of the S-band [150–152]. As a result, this method shows great promise for use as a generalised wideband NLI model, but there are two key problems that motivate an alternative approach.

Firstly, approximating the Raman profile as a triangle is an approach that is only valid as long as the transmission bandwidth does not exceed the peak of the SRS spectral efficiency, which was observed to be $\approx$ 13 THz in Sec. 2.1.6 for SSMF. For bandwidths larger than this, the "tail" of the Raman profile is mostly neglected, causing discrepancies between the model prediction and the observed power transfer. A 13 THz transmission bandwidth is equivalent to a C+L-band system that makes partial use of the S-band, which means that this approach is not guaranteed to provide accurate results for wideband systems with a larger spectral occupancy, such as L-, C-, S-, or L-, C-, S-, E-band transmission scenarios. Secondly, both the GN and ISRS GN model are aggregated models, which treat transmission between a source and destination within the network as a single unbroken route, therefore not being suitable for modelling disaggregated networks.

2.2.1 Current Limitations

Although aggregated models have been shown to be accurate for many contemporary optical network configurations [153, 154], the coherent contribution to the total NLI increases with the symbol rate, reducing their accuracy and hampering the efforts of network controllers in predicting the QoT degradation [8, 155]. Furthermore, an aggregated approach is not compatible with a disaggregated network architecture where OLSs must be considered separately, as LP history or certain physical layer parameters may be unknown.

To create a disaggregated network model, the NLI contribution for each CUT must be considered as being independently generated on a fiber-by-fiber and channel-by-channel basis, corresponding to full spatial and spectral separability, respectively. These separability requirements must then be extended to a wideband scenario that properly takes into account the effects of SRS. As an additional detail, to avoid risking out-of-service situations and network downtime, a functional wideband and disaggregated model must also be conservative, which means that its SNR predictions are lower than those actually encountered in-field.

As part of this project, investigations into the spectral and spatial separability of the SPM and XPM contributors to the NLI have been conducted for a variety of disaggregated and wideband optical network configurations [2, 5, 11, 13], presented in Chapters 4 and 5. This has included the inception of a wideband and disaggregated

model that was validated experimentally within an experimental transmission scenario spanning the L- to E-bands, with this model introduced and explained within the following section.

2.3 Disaggregated and Wideband NLI Modelling

In Sec. 2.1.5 the presence of birefringence and PMD in optical fiber was highlighted. Practically, the rapidly varying nature of the birefringence effect has a minimal contribution to the NLI generation [139], enabling the NLSE derivation to be simplified. By neglecting the effects of PMD upon the signal, propagation through a fiber may alternatively be described in terms of the dual polarisation model amplitude, $\vec{A}(z,t)$, which is given by the PMD-Manakov equation [78, 156]:

$$\vec{A}(z,t) = \left(-\hat{\alpha}(z) + \imath\hat{\beta}_2\right)\vec{A}(z,t) - \imath\frac{8}{9}\hat{\gamma}\left[\vec{A}(z,t)\cdot\vec{A}^*(z,t)\right]\vec{A}(z,t)\,, \tag{2.15}$$

where $\hat{\alpha}(z)$, $\hat{\beta}_2$, and $\hat{\gamma}$ are operators that correspond to α, β_2, and γ, respectively. The small differences between the solutions of the Manakov equation and the dual-polarisation coupled NLSE have been shown to not vary significantly for bandwidths spanning the entire C-band [139], and furthermore, these differences do not depend upon overall bandwidth, meaning that this approach is assumed to be valid also for a wideband transmission scenario.

Firstly, the system of differential equations which dictate the SRS effect can be solved for a given WDM spectra [5, 102, 157], giving the spatially and spectrally dependent power evolution that results from the SRS power transfer. The effects of SRS can therefore be thought of as another contributor to the gain/loss profile. We highlight in particular that an implementation of the solution to the coupled SRS equations is available within the GNPy repository [114]. Eq. 2.15 may also be solved with a perturbative approach, but with a key difference being that it is possible to start from a disaggregated standpoint, using the GGN model as a reference scenario. This is performed by assuming that all channels within the WDM grid are independent, Gaussian, and uncorrelated, and by including a parameter, C_∞, that quantifies the coherency of the SPM [2, 8]. C_∞ is calculated by finding the asymptotic level of the coherency, which corresponds to the maximum amount of SPM that may be

generated in a single span, for a given system configuration. As a result, this value provides a conservative upper bound to any coherent SPM effects.

The powers of the SPM and XPM effects are correspondingly given in terms of the NLI efficiency, η, the wavelength of the CUT, λ, and the wavelength of the interfering channel, κ:

$$P_{\mathrm{SPM},\lambda} = \eta_{\lambda\lambda} P_{\lambda}^{3} \,, \tag{2.16}$$

$$P_{\mathrm{XPM},\lambda,\kappa} = \eta_{\lambda\kappa} P_{\lambda} P_{\kappa}^{2} \,, \tag{2.17}$$

where P_{λ} and P_{κ} are the total channel powers over all polarization states, corresponding to the wavelengths λ, and κ, respectively. The quantities $\eta_{\lambda\lambda}$ and $\eta_{\lambda\kappa}$ are given by:

$$\eta_{\lambda\lambda} = (1 + C_{\infty}) \left(\frac{16}{27}\right) \frac{\gamma_{\lambda}^{2}}{R_{s_{\lambda}}^{3}} \mathscr{I}_{\lambda\lambda}(L_s) \tag{2.18}$$

$$\eta_{\lambda\kappa} = \left(\frac{32}{27}\right) \frac{\gamma_{\lambda}^{2}}{R_{s_{\lambda}} R_{s_{\kappa}}^{2}} \mathscr{I}_{\lambda\kappa}(L_s) \,, \tag{2.19}$$

where γ_{λ}, $R_{s_{\lambda}}$, and $R_{s_{\kappa}}$ are the nonlinear coefficient and symbol rates that correspond to the central frequencies of the channels located at λ and κ, respectively, and $\mathscr{I}_{\lambda\lambda}$ and $\mathscr{I}_{\lambda\kappa}$ are functions which emerge from the derivation of Eq. 2.15 that dictate the spectral and spatial evolution of the SPM and XPM noises, respectively, as a function of the fiber length, L_s. This model for the SPM and XPM impairments, combined to give the total NLI impairment, is referred to within the thesis as the disaggregated GN model. We direct readers seeking further detail about the derivation of $\eta_{\lambda\lambda}$ and $\eta_{\lambda\kappa}$, and the nature of the $\mathscr{I}_{\lambda\lambda}$ and $\mathscr{I}_{\lambda\kappa}$ functions to [5], as this is not explicitly covered in this thesis.

2.3.1 QoT Estimation

With the combined definitions of the linear and nonlinear impairments that arise from signal propagation, a common QoT estimator over a LP can be established. The overall QoT is often estimated using the generalised SNR (GSNR), given by [108, 154, 158]:

$$\mathrm{GSNR}_{\lambda} = \left(\mathrm{OSNR}_{\lambda}^{-1} + \mathrm{SNR}_{\mathrm{NL};\lambda}^{-1}\right)^{-1} = \frac{P_{\mathrm{ch}}}{P_{\mathrm{LIN}} + P_{\mathrm{NL}}} \,, \tag{2.20}$$

where the linear and nonlinear contributors to the QoT impairment are given by the optical SNR (OSNR), and nonlinear SNR, $\mathrm{SNR}_{\mathrm{NL}}$, respectively, with the corresponding total powers of these effects given by P_{LIN} and P_{NL}. Working from a disaggregated network standpoint, QoT estimation must be performed for each OLS independently, and so for an OLS composed of N_s fiber spans, indexed by s, the total GSNR at the end of the last fiber span is given as the sum of the GSNRs for all fiber spans:

$$\mathrm{GSNR} = \left(\sum_{s=1}^{N_s} \mathrm{GSNR}_s^{-1} \right)^{-1} . \tag{2.21}$$

Nonlinear SNR

The nonlinear contributors to the GSNR arise entirely from the Kerr effect term within the PMD-Manakov/NLSE equations, and as such are fully characterised by estimating the NLI impairment. Focusing upon a disaggregated framework, the SPM and XPM contributors to the NLI have been shown to be independent and separable for all realistic use cases [2, 123, 125, 159]. By including this correction, a conservative upper bound for the $\mathrm{SNR}_{\mathrm{NL}}$ is therefore given by the sum of the total SPM and XPM powers for a channel with a WDM grid index, n:

$$\mathrm{SNR}_{\mathrm{NL};\lambda,n} \leq \left(\sum_{s=1}^{N_s} \frac{P_{\mathrm{SPM},\lambda} + P_{\mathrm{XPM},\lambda}}{P_\lambda} \right)^{-1} , \tag{2.22}$$

where $P_{\mathrm{XPM},\lambda}$ is the total XPM impairment that arises from all interfering channels, for this particular CUT:

$$P_{\mathrm{XPM},\lambda} = \sum_{\kappa \neq n}^{N} P_{\mathrm{XPM},\lambda,\kappa} , \tag{2.23}$$

with $\kappa = n$ excluded, as this corresponds to the SPM contribution.

Optical SNR

Considering the fiber attenuation, dispersion and SRS as power transferring effects that may be considered during transmission, the primary linear contribution to the GSNR is therefore the amplified spontaneous emission (ASE) noise that occurs during the amplification process. Other smaller but noteworthy loss contributors,

such as impairments which arise from connector losses, imperfect splices, and from filtering and equalisation are not grouped within the OSNR, and are instead applied directly to the spectrum, meaning that they also affect the NLI. These contributors may be estimated through device characterisation; for example, a loss profile for a filter or equaliser for a given input power profile can be directly provided. An estimation of the total amount of these inherent system losses can be made using an optical time-domain reflectometer (OTDR), operated at low power [160].

Considering amplification in the C-band using an EDFA, for a given spectral load, the ASE noise for a single fiber span is given by:

$$P_{\mathrm{ASE},\lambda} = hf_c\zeta(f_c)(G(f_c)-1)R_{s_\lambda}\,, \tag{2.24}$$

where $\zeta(f_c)$ and $G(f_c)$ are the amplifier NF and gain values evaluated at the channel central frequency, respectively. When EDFA parameters are unknown or inaccurate, and/or the spectral load is not constant, additional information is required to calculate ASE noise power profile. In these scenarios, telemetry and monitoring data can be used to overcome the lack of information, e.g. with machine learning frameworks [1, 3], or with a model based characterization as in [102]. In general, this is not the case, as EDFAs have frequency dependent noise figures and gain profiles, with the fluctuations frequently present within the latter depending upon the input power spectrum [161, 162]. This effect may be included and compensated for as part of a more in-depth amplification model [3, 163, 164], however, as the primary focus of this thesis is upon NLI generation, these procedures lie outside of the scope, and as such is not included unless stated otherwise. Consequently, the OSNR may be written in terms of the power of a given CUT, $\mathrm{P_{CUT}}$, and the power of the ASE noise, $\mathrm{P_{ASE}}$:

$$\mathrm{OSNR}_{\lambda,n} = \left(\sum_{n=1}^{N_s}\frac{P_{\mathrm{ASE};\lambda}}{P_\lambda}\right)^{-1}. \tag{2.25}$$

2.3.2 Abstracting Optical Networks

With the GSNR and its contributors defined, the discussion now turns to how this value may practically be estimated for network monitoring and planning purposes. For a given optical network, QoT estimation may be performed by creating a so-called digital twin, where software models of the OLSs, amplifiers, and ROADM

nodes are created [165–167]. One good example of a software framework that makes use of this implementation is the GNPy library, where network configurations may be provided in JSON format, which is used to initialise an object-oriented architecture [168, 169]. This consequently permits estimation of the QoT impairments with the help of component and amplifier characterisation data, taken from both experimental or data-sheet measurements. A gain/loss profile that includes the effects of SRS power transfer may then be calculated using the built-in coupled SRS equation solver, known as the `RamanSolver` module, which is paired with an estimation of the NLI that comes from an implementation of the GGN model, for a given user-defined WDM spectra. Wideband and disaggregated implementations have also been possible with edits to the codebase, which have been performed within a variety of works related to this thesis [9, 11, 13].

The semi-analytical solution that may be used for NLI calculation that is presented in Eqs. 2.18 and 2.19 contains some assumptions, such as the AWGN hypothesis. To attain the highest possible NLI estimation accuracy, split-step Fourier method (SSFM) simulations may be used, where a numerical, step-wise evaluation of the signal propagation is performed, requiring far greater computational resources, but avoiding any uncertainties which may arise from assumptions in a semi-analytical approach. The SSFM framework that has been used to validate this model and perform accurate transmission experiments is outlined in the following chapter.

Chapter 3

Simulation Framework

The evolution of a WDM signal as it propagates through a fiber medium can be calculated numerically using the SSFM. Implementations of this technique have been essential for benchmarking semi-analytical and closed-form models, on account of its ability to accurately capture realistic nonlinear propagation impairments [77–79, 170–173]. Compared to semi-analytical or closed form methods, the SSFM provides an estimation of the NLI for propagation through an optical fiber with minimal assumptions or simplifications, and is frequently used a ground truth to validate other approaches. Within this chapter, the concept, workflow, and structure of the SSFM will be outlined, with separate details such as configurations and context-dependent settings explained in the following chapters and sections where they are of relevance.

The concept of the SSFM starts from the input of the fiber, where $z = 0$, and then splits the fiber length into z_m small, consecutive segments, each of a variable length $\mathrm{d}z_m$. For each $\mathrm{d}z_m$, two steps are performed: a nonlinear step, $\hat{N}$, followed by a linear step, $\hat{L}$. This approach produces an inaccuracy that is proportional to $\mathrm{d}z_m$, which vanishes as $\mathrm{d}z_m \to 0$; subsequently, $\mathrm{d}z_m$ can be reduced to a value that is sufficiently small to produce a negligible inaccuracy [79, 91]: A variable value of $\mathrm{d}z_m$ is used to increase the accuracy of the final result; as the power is higher at the start of the fiber span, larger amounts of impairments and signal distortions are produced, meaning that a greater step resolution is required [174, 175]. For the SSFM implementation used within this thesis, a FWM-CLE optimization algorithm is used to optimise $\mathrm{d}z_m$, ensuring that the simulation error remains constant as the

bandwidth is enlarged [79], with the size of $\mathrm{d}z_1$ determined by a variable, Φ_{FWM}, that corresponds to the maximum nonlinear phase shift.

The SSFM may be used to numerically solve the dual-polarisation coupled NLSE, but as with the semi-analytical solution shown in Sec. 2.3, the PMD-Manakov equation may be instead used as a starting point, providing a reduced computational complexity with minimal impact upon the simulation accuracy. The calculation performed at each $\mathrm{d}z_m$ is given by:

$$\vec{A}(z_m+\mathrm{d}z_m,t)=\mathscr{F}\left\{\hat{N}\left[\vec{A}(z_m,t)\right]\right\}+\hat{L}\left[\vec{A}(z_m,t)\right], \tag{3.1}$$

where $\mathscr{F}\{\cdot\}$ is the Fourier transform operator, which is performed in the MATLAB® environment using the fast Fourier transform (FFT) algorithm [176]. The nonlinear and linear steps are explicitly given by:

$$\hat{N}\left[\vec{A}(z_m+\mathrm{d}z_m,t)\right]=\mathscr{F}^{-1}\left\{\vec{A}(z_m,f)\right\}e^{-\imath\frac{8}{9}\hat{\gamma}\left|\vec{A}(z_m,t)\right|^2\mathrm{d}z_m}, \tag{3.2}$$

$$\hat{L}\left[\vec{A}(z_m+\mathrm{d}z_m,f)\right]=\mathscr{F}\left\{\vec{A}(z_m+\mathrm{d}z_m,t)\right\}e^{-\imath\beta(f)\mathrm{d}z_m}\frac{\rho\left(z_m+\mathrm{d}z_m,f\right)}{\rho\left(z_m,f\right)}, \tag{3.3}$$

where $\mathscr{F}\{\cdot\}^{-1}$ is the inverse Fourier transform operator. After the new signal has been calculated, the algorithm moves to the next segment, m, until the entire fiber length has been iterated over. This SSFM iterative process is shown diagrammatically in Fig. 3.1.

3.1 Computational Requirements

This project makes use of an internal library based upon a modified and restructured version of [78], which is built around a core function that numerically solves Eq. 3.1. This library permits a fully disaggregated and wideband approach, where DWDM grids with arbitrary values of channel power, bandwidth, and symbol rate are permitted, along with OLS abstractions that may be specified explicitly or given in terms of repeated fiber-amplifier pairs. Additionally, transmission through OLSs with in-line dispersion compensation, non-uniform fiber spans, and spectral configurations consisting of mixed IMDD and coherent signals is also permitted. The primary difference of this library from [78] is the conversion to an object-oriented

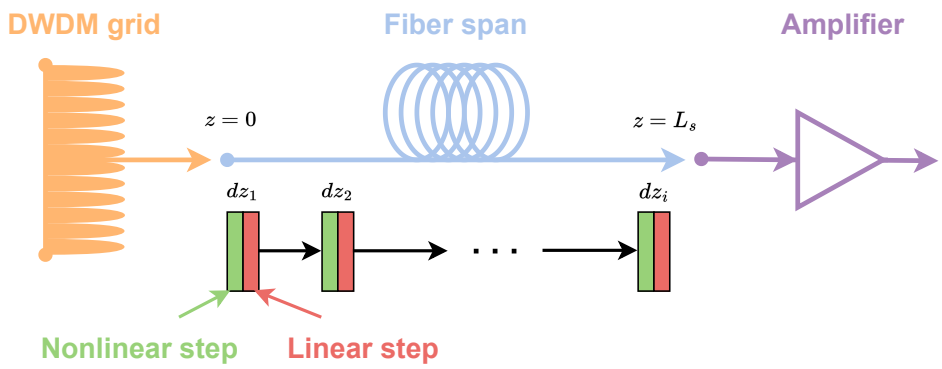

Fig. 3.1 A diagram showing the SSFM methodology. First, a DWDM signal is generated and passes into a portion of the fiber span of length dz_1, where nonlinear and linear operations are performed. The signal then passes into the next portion, with this process repeated until the entire length of the fiber has been traversed. Amplification is then performed and the entire process is repeated as necessary

format, where JSON files are used to create the required OLS/spectral information, in a similar manner to the GNPy library. In fact, the JSON structure of this project is fully compatible with the GNPy library JSON format, except for additional details required by the SSFM that can be ignored/discarded if the same configuration is used within GNPy. From this compatibility, a direct comparison between the SSFM and GNPy libraries is possible, which means that the NLI estimation from the disaggregated GN model may be verified by the SSFM.

An unfortunate detail is that the SSFM technique has unavoidably large computational requirements, for multiple reasons. Firstly, for each $\mathrm{d}z_m$ segment, the $\hat{L}$ and $\hat{N}$ operators must be applied upon the signal, which include two Fourier transform operations, an abs$|\cdot|^2$ operation, and two exponential. The limiting operations in this case are the Fourier transform operations, as the built-in MATLAB® FFT and IFFT algorithms have an order of $\mathcal{O}(N\log_2(N))$ [177], which produces a proportionality between the computational requirements and the size of the signal array. To realistically emulate transmission, a sufficiently long signal length must be used, producing arrays which already impart significant computational requirements. Moreover, to capture all nonlinear effects which take place during propagation it is necessary to consider a bandwidth which is, for most scenarios, at least twice the total DWDM grid bandwidth.

Even for C-band transmission scenarios, the total DWDM grid bandwidth can be as large as 4.8 THz; if a NLI estimation is required for a full spectral load transmission

scenario, the resultant computational requirements may cause this simulation to take weeks, even when making use of cutting-edge hardware to perform the required calculations. The result is that, despite the high level of accuracy, the SSFM technique may not be used directly for network monitoring scenarios, where near-real-time QoT estimations are required, which has been the primary motivation for the development of other, faster approaches, such as the GN model and its derivatives. Naturally, for wideband scenarios this computational requirement is even larger, which further motivates an approach that reduces computational requirements with a permissible loss of accuracy.

For benchmarking purposes, the SSFM simulations within this work were primarily performed on a dedicated server rack containing: two GPUs (a Tesla V100-PCIe 16 Gb and a Tesla V100S PCIe 32 Gb), 9 Tb of RAM, and two CPUs, both Intel® Xeon® Gold 6242 at 2.80 GHz, each with 16 cores and 32 threads. To most efficiently perform the aforementioned operations upon the signal [178], all signal calculations are performed using the graphics processing units (GPUs) of the server rack, by defining the signal array as a MATLAB® `GPUArray` object, and dividing simulation campaigns such that multiple GPUs are in use simultaneously.

3.2 Workflow and Physical Layer Abstraction

A diagram showing the workflow of the SSFM library used for this project is shown in Fig. 3.2, with the processes separated primarily by colour: information fed into the SSFM is given in blue, initialisation procedures and set-up is given in green, the propagation block enclosed by red, all receiver-side DSP and NLI recovery enclosed by purple, and any optional steps given in yellow.

3.2.1 OLS Abstraction and Initialisation

For a given simulation campaign the required OLS structure is defined in terms of four JSON files, which consist of: the spectral parameters, which describe the parameters of the WDM signal, the fiber parameters, which describe the characteristics of the fiber and any required amplification or in-line dispersion compensation, the DSP parameters, which provide the RX settings, and other global parameters, which contain details of all other specific conditions, such as where to save the output

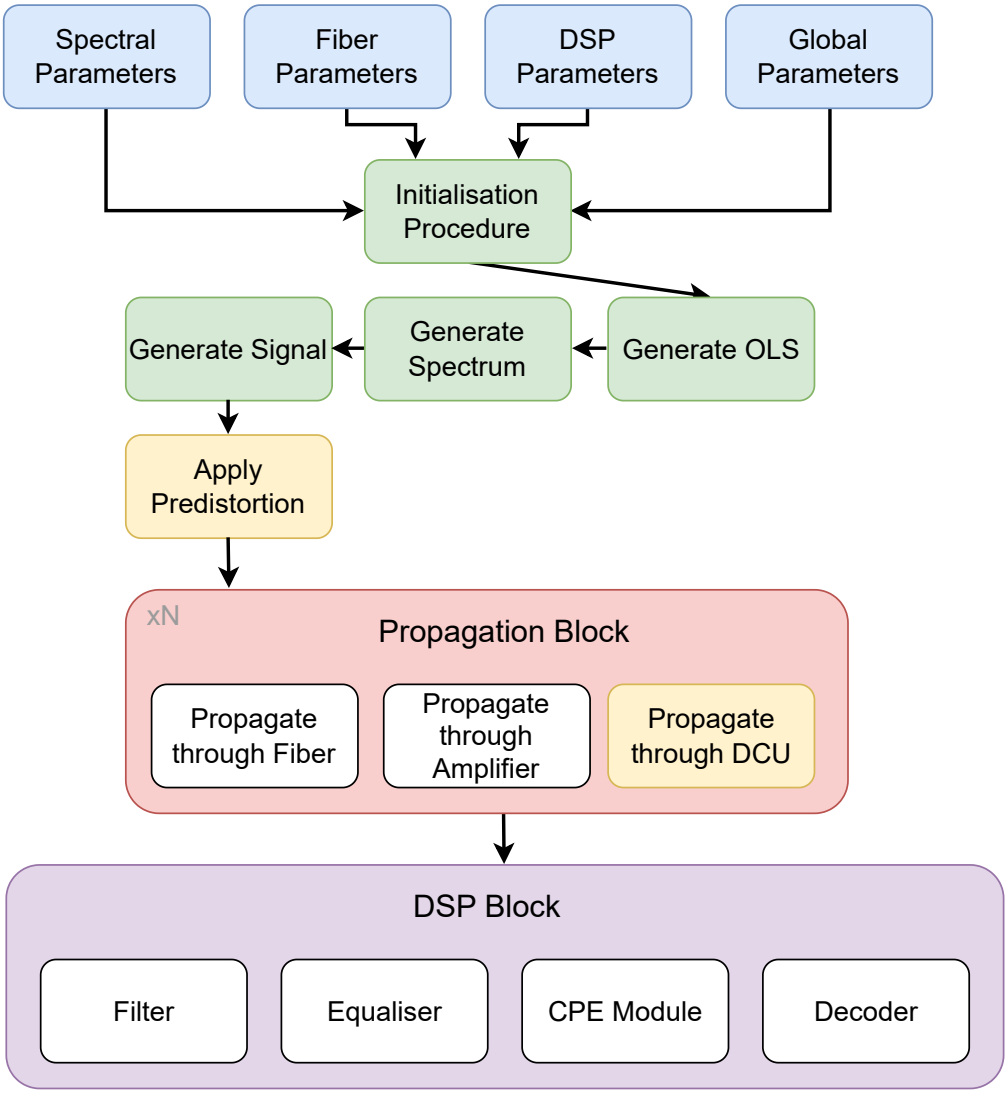

Fig. 3.2 The workflow of the SSFM library used in this project, with optional stages given in yellow. The four parameter files are provided to the SSFM in JSON format, which is then used to construct the corresponding MATLAB® objects. After initialisation is finished, the signal in DWDM format is propagated through the fiber and amplifier cascade, which at its termination is passed into the RX and DSP model, providing the SNR values of all CUTs.

files, and algorithmic accuracy settings. These JSON files are passed into a step summarised as the initialisation procedure, where the parameters and settings are abstracted into an object-oriented structure in the MATLAB® software environment.

After this, the OLS abstraction is created, where the fiber, amplifier, and optional dispersive elements are placed in succession, so that when propagation is initialised, the signal passes through all elements in the correct order. The DWDM spectrum is generated using a DSP-based TX, with each polarization component created using an independent pseudo-random binary sequence (PRBS) with a polynomial with a degree, n_p, that determines the data sequence length, as required. Before transmission, each channel within the WDM comb is up-sampled and shaped using a root-raised cosine filter that has a configurable channel roll-off value. For all scenarios within this work, unless stated otherwise, a roll-off value of 0.15 has been used. Varying this value did not cause any noticeable difference to the $\mathrm{SNR}_{\mathrm{NL}}$ estimation.

The parameters of each channel are specified within the spectral parameters, which permits unique or uniform values of P_{ch}, R_s, f_c, B_{ch}, and M, the latter corresponding to the parameter which encodes the modulation format for a given signal with b bits per symbol, where $M = 2^b$. An array corresponding to the total WDM grid is therefore created, where each channel has its own distinct values for each of these parameters. It is also possible to adjust the accuracy of the SSFM by changing the size of the first $\mathrm{d}z_m$ step, $\mathrm{d}z_1$.

Signal Predistortion

As mentioned within Sec. 2.1.4, dispersive effects shape the signal towards that of a Gaussian during propagation in a process known as Gaussianisation [106]. Practically this means that signals enter the OLS under consideration with some degree of Gaussianisation already applied, signal predistortion may be applied to investigate this effect. In disaggregated scenarios where the NLI accumulation requires investigation, signal predistortion can therefore be optionally applied, in order to progressively reduce or eliminate the effects that arise due to Gaussianisation within the first few fiber spans. The level of signal predistortion is specified by a parameter, Θ_{pd}, that quantifies the required amount of dispersion to add to or subtract from the signal directly before transmission is performed.

3.2.2 Propagation Block

After the signal(s) have been generated and the spectrum has been prepared, transmission begins by passing the spectrum into the propagation block. For each element defined within the fiber parameters, a corresponding custom MATLAB® object is generated. Starting with the `Fiber` object, two dispersion and loss configurations are possible: the single-band and wideband configurations. In the single-band configuration, the user provides a fiber dispersion value in terms of D, for a given λ_{ref}, and a total linear loss coefficient. In this scenario, these parameters are considered to be flat across the entire spectrum, meaning that they are suitable only for C-band simulations where the variation in these parameters provides tolerable losses in accuracy. For the wideband configuration, the user provides β_2, β_3, (and optionally β_4) for a given λ_{ref}, along with a gain/loss profile, $\rho(z, f)$, from a linked JSON file, calculated a priori by solving the coupled SRS equations. This calculation takes into account all linear losses and power transferring effects, including any power transfer due to Raman amplifiers, if present. This configuration considers the frequency variation of the fiber parameters for the entire wideband spectrum, and is the approach used for simulations which have bandwidths larger than the C-band. The other crucial fiber parameters are L_s, given in km, the value of γ for the λ of the CUT, the fiber PMD coefficient, which is always set to 1.265×10^{-15}, and any attenuation due to input and output connector losses, which are always set to 0, as connector losses are handled through postprocessing in the GNPy library, if required.

The amplifiers are abstracted as `EDFA` objects, which have gain, tilt, output variable optical attenuator (VOA), and NF values. These EDFA settings can be explicitly provided from experimental measurements to give an accurate EDFA model, or otherwise set to operate in transparency, whereby the signal power is perfectly recovered. In all projects within this thesis, the SSFM is used purely for evaluation of the NLI, and EDFA amplification is done separately within the GNPy framework. This decision is made due to the GNPy library enabling a greater level flexibility; as the NLI and OSNR are separable, evaluating the OSNR separately from the NLI significantly reduces computational and troubleshooting time. Subsequently, all EDFAs operate in transparency, meaning that the only impairment present after propagation arises due to NLI. The gain parameter is therefore set to fully recover the signal power, and the other parameters are not considered within the SSFM in this project.

Considering the optional dispersive elements, these are represented by `DCU` objects, which are a child of the `Fiber` class, but do not impart any losses during propagation, serving only to induce a dispersive effect onto the signal. This effect is specified by the user with a parameter, D_{DCU}, providing the amount of dispersion to be applied (either positive or negative), at a given reference wavelength.

All propagation block objects may be described explicitly within the fiber parameters JSON, otherwise a sequence of objects may be given along with a `repetitions` variable, which flags the SSFM to loop over the given configuration a number of times equal to this variable, constructing a periodic line. The propagation itself is performed by calling a `propagate` method for each object, which calculates the NLI impairment for the fiber, amplifies the signal, and adds a specified amount of dispersion, for the `Fiber`, `EDFA`, and `DCU` objects, respectively. For each object, flags are included to specify whether dispersion compensation will be performed, along with whether to recover the signal at this point. Experimentally, recovery of the signal is only feasible at the receiver, but within a simulation framework such as this it is possible to recover the signal at any point, permitting an estimation of the NLI to be given after each fiber span. Additionally, is it possible to specify a `kerr_on` variable, which can be used to switch off all nonlinear effects within any given fiber spans. This permits the NLI impairment to be investigated on a per-span basis, which proves essential for evaluating NLI accumulation within Chapter 4.

3.2.3 Digital Signal Processing Block

As a first step after propagation, dispersion compensation is performed using an ideal dispersion compensation module that fully recovers the dispersion that is accumulated during propagation, for all line objects that have dispersion compensation enabled. The signal then passes into the DSP block, which has multiple stages. Firstly, for each CUT, the signal passes through a re-sampling filter, which isolates only the frequencies within the CUT bandwidth. An ideal, noiseless ADC is then applied, digitising and fully recovering the signal for the four polarisation states of each CUT by re-sampling the WDM signal at 2 samples per symbol. Following this there is an adaptive equaliser stage, which, for all simulation campaigns, utilizes a least mean squares (LMS) algorithm with 42 taps and an adaptation coefficient, μ, of 1×10^{-4}. This amount of taps is larger than may be expected experimentally, which

helps to ensure that the back-to-back (B2B) performance is high with respect to the transmitted signal, and to ensure that the NLI is recovered accurately.

After the equaliser, a carrier phase estimation (CPE) block recovers the nonlinear phase noise, which is visible as a circular shift of the constellation points towards the axes, which may practically be compensated for by the CPE [179]. The CPE block implements a blind-phase search using the Viterbi-Viterbi algorithm [180], fully recovering all nonlinear phase noise induced upon the signal. An example constellation after propagation of a 16-QAM signal through 10 fiber spans of SSMF is shown in Fig. 3.3. Comparing the observed constellation to Fig. 2.2b, which shows an ideal 16-QAM signal before transmission, it is visible that the CPE algorithm has completely recovered all nonlinear phase noise, leaving only circular noise present around each point of the constellation. The CPE algorithm uses a memory that may be fixed or dynamic, with the optimal value maximising the circularity of the noise clouds around the transmitted symbol scattering diagram. The dynamic memory mode uses knowledge of the transmitted symbols to find the optimal CPE memory value, which is useful for scenarios where fiber parameters such as length or dispersion change throughout the course of an OLS.

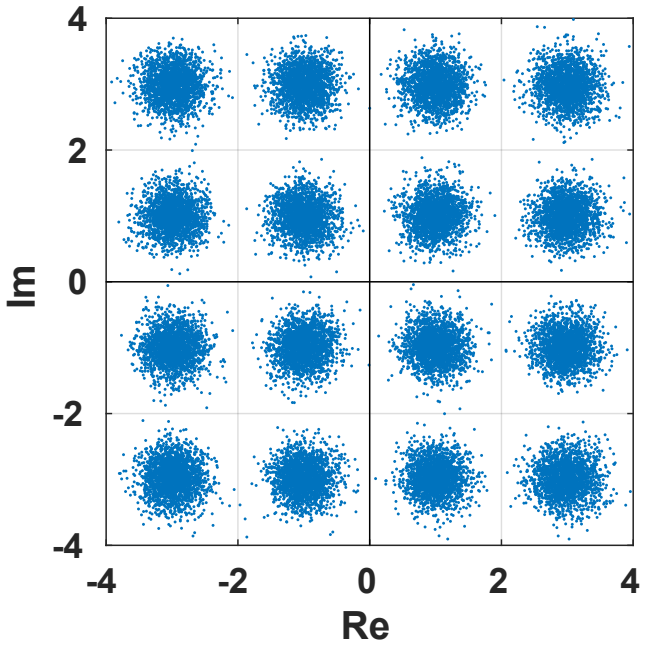

Fig. 3.3 The constellation of a 16-QAM signal after propagation through 10 spans of SSMF fiber, each followed by a transparent amplifier.

By assuming that the receiver is ideal and lossless, the transmitted symbol series can be subtracted from the received signal, and $P_{\mathrm{NLI};\lambda}$ can be evaluated as the variance of the difference between the two signals. Subsequently, $\mathrm{SNR}_{\mathrm{NL};\lambda}$ is extracted by taking the error vector magnitude (EVM) upon the received constellation at 1 sample per symbol, at the termination of each fiber span.

3.3 Configurations

As mentioned in Sec. 3.1, perfectly emulating transmission of a DWDM grid undergoing full spectrum transmission is a task which has a prohibitively high computational resource requirement. These requirements increase proportionally to the spectral occupation, which makes modelling wideband transmission for a system under full spectral load difficult. It is therefore desirable to explore configurations of the SSFM that can reduce this requirement without significantly sacrificing accuracy.

When operating within a disaggregated scenario, channels are considered to be spectrally disaggregated, where the NLI generated at a given channel is independent from the NLI generated at all other channels. This therefore implies that the SPM and XPM can be separated on a per-channel basis, and then combined to reconstruct the total NLI, in a so-called superposition of effects. Furthermore, as the spectral separation between two given channels increases, the interference generated between them decreases, and, correspondingly, so too does the XPM contribution from an interfering channel upon a CUT. From these motivations a variety of spectral configurations for the SSFM are formulated to help reduce computational complexity: full-spectrum, single-channel, pump-and-probe, and limited-bandwidth.

3.3.1 Full-Spectrum

The most straightforward configuration is the full-spectrum scenario, which consists of a densely packed WDM grid, where every available frequency slot contains a channel undergoing propagation. An arbitrary number of CUTs may be specified, replacing any of the interfering channels, and when the signal is received, these CUTs are iterated over by the receiver block. An example full spectral load configuration for 11 channels and a single CUT is shown in Fig. 3.4.

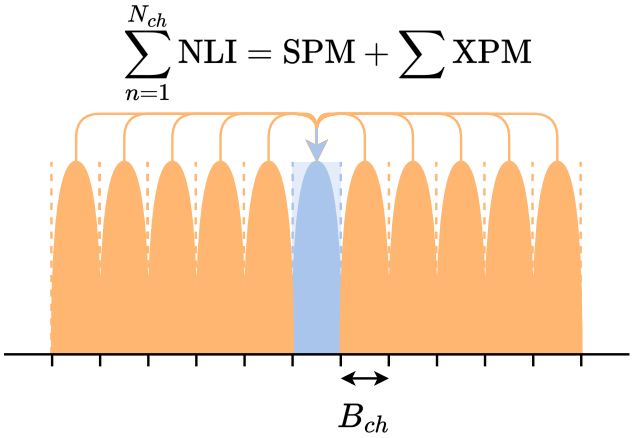

Fig. 3.4 A diagram showing a full spectrum SSFM configuration for one CUT and 10 interfering channels. In this scenario, all channels transmit with an equal power, providing the total SPM and XPM impairments.

The full-spectrum configuration is the most computationally expensive way to perform simulations, and is typically limited to bandwidths spanning no more than a single band (or less for larger bands such as the S-band). However, the full-spectrum configuration represents the most accurate way of operating the SSFM, and may be compared to other configurations to verify whether a loss of accuracy has occurred. Full-spectrum simulations are launched with parameter settings of $n_p = 15$, and $\Phi_{\text{FWM}} = 1$.

3.3.2 Single-Channel

The single-channel configuration propagates a single CUT, without any interfering channels, corresponding to a case where the CUT and interfering channel occupy the same bandwidth. As no XPM impairments are generated, this configuration is used to evaluate solely the SPM contribution to the total NLI impairment. An example single-channel configuration is shown in Fig. 3.5. Single-channel simulations require a greater level of accuracy than the other configurations, due to a low total spectral bandwidth inducing a larger nonlinear phase shift. Subsequently, all full-spectrum simulations within this work are launched with parameter settings of $n_p = 17$, and $\Phi_{\text{FWM}} = 0.01$, providing a trade-off between accuracy and computational complexity.

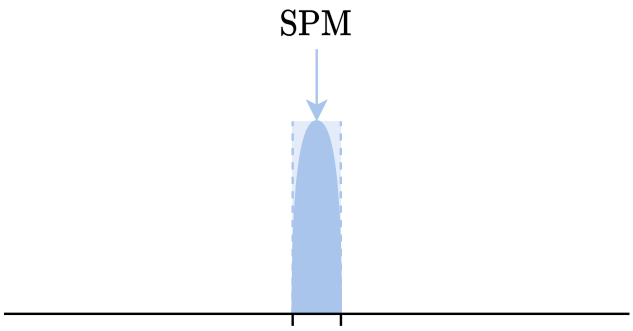

Fig. 3.5 A diagram showing how the SSFM operates when in single channel mode, where only the CUT is propagated through the system abstraction, in order to quantify solely the SPM impairment.

3.3.3 Pump-and-Probe

The XPM impairment of every given interfering channel upon a given CUT may be evaluated through a series of simulations run in pump-and-probe configuration, consisting of a single CUT, and a single interfering channel, spectrally separated by Δf. These simulations may be performed in isolation, or for every pump that constitutes a full-spectrum configuration, for a given CUT, with an example shown in Fig. 3.6. To fully isolate the XPM contribution, it is necessary to ensure that the probe power is sufficiently low so that no SPM impairments are generated.

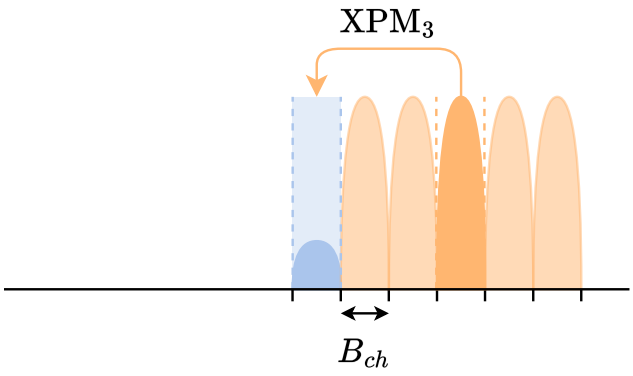

Fig. 3.6 A diagram showing the configuration for pump-and-probe simulations, which are used to investigate the XPM contribution. Here, five separate simulations are performed, with one channel turned on at a time, with the third channel currently transmitting. The power of the CUT is lowered with respect to the interfering channels in order to limit SPM contributions.

Within all pump-and-probe simulations (besides the scenario when the pump neighbours the probe, which must be set on a case-by-case basis to ensure NLI recovery and minimise pump-probe crosstalk), the probe power is set to -20 dBm, which was high enough to enable recovery of the XPM impairment, with negligible SPM contributions. For pump-and-probe configurations settings of $n_p = 16$, and $\Phi_{\text{FWM}} = 1$ were used.

3.3.4 Limited-Bandwidth

The final configuration, only used for wideband transmission, is the limited-bandwidth configuration. This simulation operates similarly to the full spectrum scenario, however, for each CUT, all channels only within a given bandwidth on either side of the CUT are considered. An example limited bandwidth configuration, where only three interfering channels on either side of the CUT are considered is given in Fig. 3.7, with the first channel to be considered on the left of the CUT assigned an index, n_0. This approach is considered to enable completion of wideband simulations within reasonable timeframes, and is justified by the nature of the NLI generation; as mentioned within Sec. 2.1.4, the XPM contribution falls off with an approximately $1/x^2$ relation, meaning that interfering channels sufficiently far from the CUT have a negligible contribution to the total NLI. The result is that the total

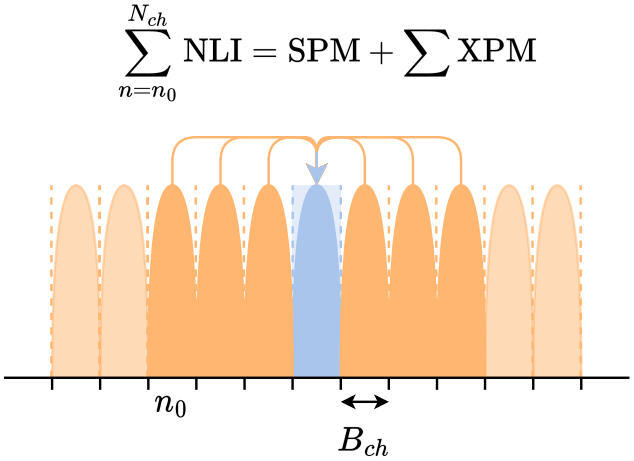

Fig. 3.7 A diagram showing a limited bandwidth SSFM configuration for one CUT and 10 interfering channels, but with only 3 channels on either side of the CUT considered for estimating the NLI impairment.

spectrum for each CUT may be limited with only small losses in NLI estimation, provided that frequency-dependent parameter scaling and effects due to SRS being properly taken into account. In practice, this NLI effective bandwidth is observed to be approximately 2 THz for each CUT in a C-, L-, S-band scenario [5]. For the limited-bandwidth simulations performed as a part of this thesis, bandwidths of 1.5 THz on either side of the CUT were considered, in order to ensure that there was no significant underestimation of the NLI, providing a good trade-off between accuracy and computational complexity.

Chapter 4

Modelling Disaggregated Network Segments

To enable a signal propagation model that is suitable for a disaggregated network transmission scenario, it is essential to create a model framework which permits spectral and spatial separation. In this regime, every channel (and, correspondingly, every NLI contribution) is considered to be independent, and each fiber span is completely separated from each other fiber span, respectively. The verification of spectral separability has previously been described in Sec. 3.3 with the implementation of a full-spectrum superposition, which is enabled by the full separability of the SPM and XPM contributors to the NLI impairment. This approach has been investigated in [2] (an article produced as part of this thesis), in combination with an implementation of the coherent accumulation factor, C_∞, as described in Eq. 2.18. By including this factor, the maximal SPM impairment is quantified, which enables the realisation of spatial separability, therefore creating a modelling framework that enables full spectral and spatial separability.

The simulation campaign performed within [2] was for a variety of OLSs that consist of 20 fiber spans, each with identical physical layer parameters. In a realistic disaggregated network deployment scenario this is not an entirely adequate validation, as fiber spans lengths are seldom equal through an OLS due to installation capabilities and requirements, compounded further by multiple vendors being responsible for fiber deployment. Additionally, when network upgrades are performed. the likelihood that new OLSs make use of identical or even similar fibers to those cur-

rently deployed within the network is not guaranteed. The result is that, as networks grow, it is anticipated that the variety of the installed fibers will increase, unless certain steps are taken to enforce standardisation. The ability to model fibers with non-uniform parameters through a given OLS is therefore a requirement for any NLI model which supports disaggregation. There is consequently a desire to investigate how this separability is affected when the fiber parameters change throughout the OLS, in order to create scenarios that more accurately correspond to realistic OLS architectures, and extend the validity of the wideband and disaggregation model. Within this chapter, these concepts will be explored through a variety of simulation campaigns using the common framework described within Chapter 3.

First, the idea of a disaggregated network segment is defined, which corresponds to a region within a disaggregated network that is composed of multiple OLSs, each potentially managed by different vendors, and each potentially having different underlying characteristics, including fiber dispersions, lengths, and amplification or dispersion management techniques. An example segment within a disaggregated network is shown in Fig. 4.1. The starting point of the signal within this framework cannot be assumed to lie within the disaggregated optical segment, meaning that channels may begin transmission with arbitrary amounts of distortion as a result of signal Gaussinisation, which must be taken into account.

The most important fiber parameters that concern NLI generation through a non-uniform OLS are L_s, β, and γ. Starting with L_s, this parameter directly affects the amount of NLI which is generated during propagation, as it corresponds to z in 2.15. The majority of the NLI is generated within the fiber effective length, L_{eff}, given by [91]:

$$L_{\text{eff}} = \frac{1 - e^{-\alpha L_s}}{\alpha}, \tag{4.1}$$

evidently, a reduction in L_s produces a corresponding reduction in L_{eff}. Concerning β, this parameter affects the NLI generation due to changes in signal power that arise during accumulation of the linear impairment in 2.15. Additionally, in dispersion-managed OLSs, small amounts of residual dispersion may be present, which has been shown to change the accumulation of the NLI contributors [13]. Regarding γ, this parameter causes a flat shift in the amount of NLI which is generated in a given fiber span, however this does not cause a significant issue if the γ values for each fiber within the system are known.

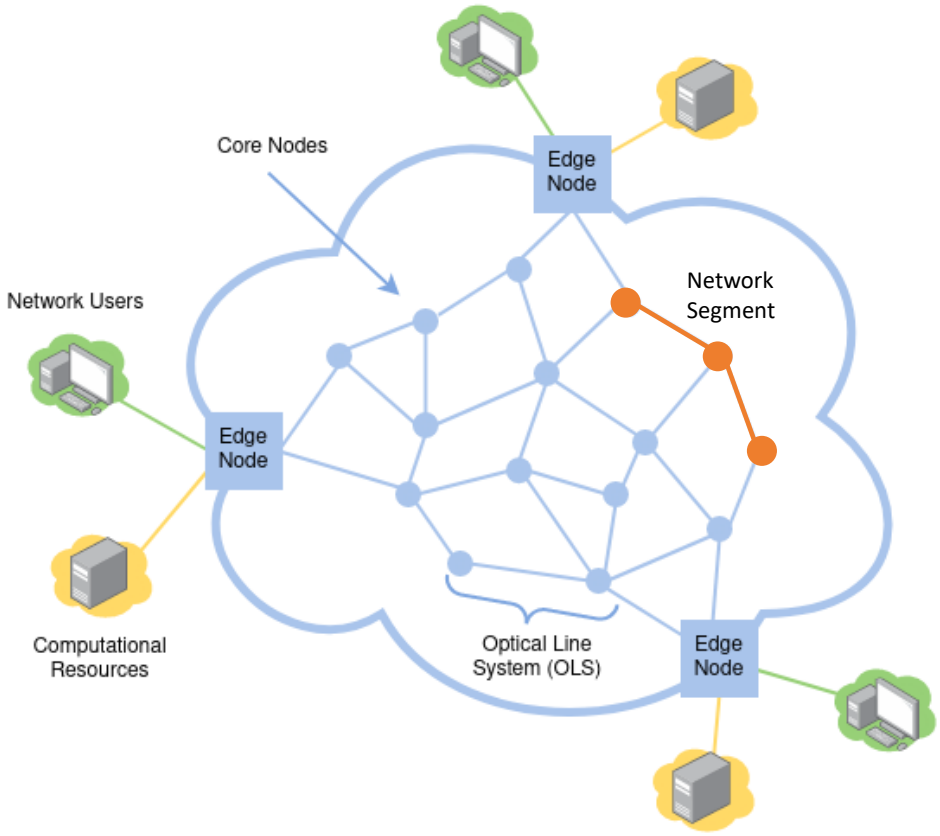

Fig. 4.1 An example disaggregated optical network infrastructure. Data is transmitted along LPs that pass through successive OLSs from a source to a destination. A disaggregated network segment is highlighted in orange.

4.1 Chapter Overview

This chapter focuses upon how changing fiber parameters within a disaggregated network segment affects the accumulation of the SPM and XPM contributors to the NLI. A variety of simulation campaigns have been launched to investigate the accumulation of the NLI through disaggregated network architectures that occupy a portion of the C-band, with extensions to wideband architectures that make use of the findings presented here outlined in Chapter 5.

The first investigation concerns how changes in L_s (and, correspondingly, L_{eff}) impact the accumulation of the NLI, and how a maximal amount of NLI may be quantified in cases where L_s or the distance from the signal origin point are not accurately known. Next, simulations are performed to reaffirm the spectral and spatial separability hypothesis and provide validation of the wideband and disaggregated

model outlined in Sec. 2.3, along with an investigation of the NLI generation for a coherent signal passing through a system that consists of three OLSs with distinct fiber dispersion configurations. After this, the effect of residual dispersion within dispersion-managed links is investigated for coherent transmission, along with a summary of how NLI modelling may be approached within disaggregated network infrastructures as a whole following the observations made within this chapter.

4.2 Impact of Fiber Span Length

To investigate the impact of changing fiber lengths within a disaggregated network segment, a simulation campaign is launched consisting of a variety of pump-and-probe simulations. First, regarding the spectral information, the pump is placed 150 GHz away from the probe, located at 194.05 THz and 193.9 THz, respectively, each with $B_{\text{ch}} = 75$ GHz. For both the pump and the probe, the symbol rate, R_s, is set to 64 GBd. As described in Sec. 3.3.3, P_{CUT} is set to -20 dBm to ensure that there is negligible SPM contribution, whereas $P_{\text{ch}} = 6$ dBm to ensure that the simulation falls solidly within the nonlinear regime, guaranteeing that a sufficient amount of NLI is generated. Concerning the modulation format, two scenarios are investigated: one where both the pump and probe are set to transmit signals with QPSK modulation, and the other where the probe is set to transmit a QPSK modulated signal, and the pump is launched with 16-QAM modulation. These scenarios have been chosen in order to inspect the modulation format dependence of the XPM accumulation. The choice was made to only change the modulation format of the pump, as changing the modulation format of the probe was found to not significantly affect the results, but gives a less accurate final result proportional to the increase in Δf. This lack of difference in the results when changing the modulation format of the probe can be explained by the probe power being significantly lower than the pump, and as such, only small changes to the overall NLI generation are observed.

Moving onto the line configuration, a periodic OLS consisting of 40 fiber-amplifier pairs is considered, with the amplifiers corresponding to transparent and noiseless EDFAs. For this specific simulation campaign, the fibers all have identical parameters, and any parameter changes are applied to every fiber span within the system equally. Four L_s values have been investigated: 50, 80, 100, and 200 km, with the former three values lying within the range of realistic deployed

fiber lengths, and the fourth value chosen to see how the NLI accumulation behaves as L_s is increased beyond current realistic levels. These fibers are assigned values of $\alpha_{\mathrm{dB}} = 0.2\,\mathrm{dB/km}$, $\gamma = 1.27\,\mathrm{W^{-1}km^{-1}}$, and, for this investigation, uniform dispersion values of $16\,\mathrm{ps\,/\,(nm{\cdot}km)}$.

To present the results of this simulation campaign in terms of a common metric, the NLI power is normalised with respect to $P_{\mathrm{CUT}}^2 P_{\mathrm{ch}}$, which corresponds exactly to the NLI efficiency for the XPM, $\eta_{\lambda\kappa}$, from Eq. 2.19. For ease of reference this value is referred to as η within this section. The gradient of η, denoted $\Delta\eta$, is then presented on a logarithmic scale to visualise the difference in η on a per-span basis, with this quantity defined as:

$$\Delta\eta = \eta_n - \eta_{n-1}\ , \tag{4.2}$$

where n corresponds to the index of the fiber span, ranging from $n = 1$ to $n = N_s$, with $n = 0$ corresponding to the value of η given by the TX B2B.

4.2.1 Periodic Scenario

The results of this simulation campaign are presented in Figs. 4.2 and 4.3 with all four L_s values, for the scenarios where the pump is transmitted with QPSK and 16-QAM modulation, respectively. Additionally, the value given by the disaggregated GN model for a single propagated span has been calculated, and shown as a reference level (given by the red line) by extrapolating this result, for all values of n. As this investigation concerns only the XPM contributor, in this scenario the disaggregated GN model is fully incoherent. The first observation to be made is that all L_s scenarios feature a similar behaviour: $\Delta\eta$ begins at the same level and experiences a logarithmic increase towards an asymptote as the signal passes through the OLS, with increasing L_s values providing a faster trend towards this level. The asymptotic value is well approximated by the disaggregated GN model result, which serves as an upper bound to $\Delta\eta$ for any given fiber span. The disaggregated GN model result corresponds to transmission of a fully Gaussianised signal, on account of the assumptions made during the derivation of this model.

The behaviour of the NLI accumulation in this scenario therefore corresponds to the progressive Gaussianisation of the pump as more predistortion is applied. Figs. 4.2 and 4.3 present the same behaviour in this regard, with the main difference

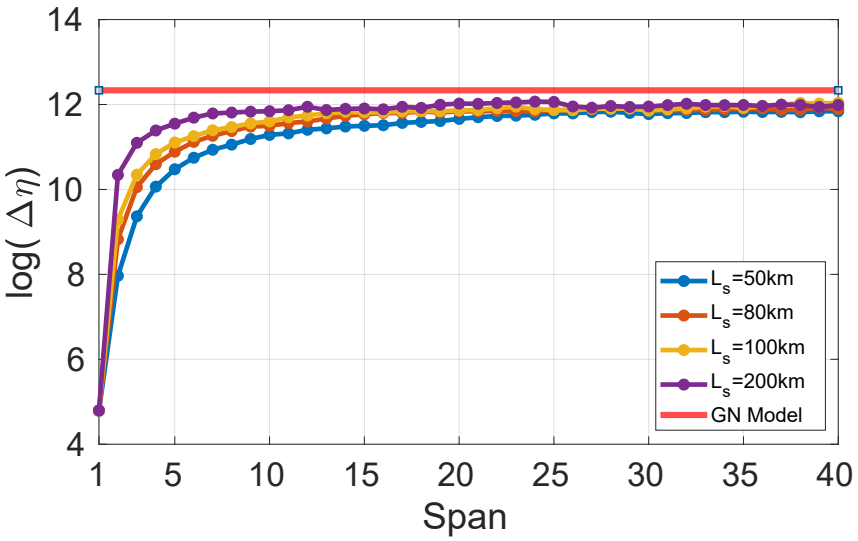

Fig. 4.2 The results of a pump-and-probe simulation campaign along a 40-span periodic OLS, for both pump and probe transmitted with QPSK modulation. Four span length scenarios are presented: L_s =50, 80, 100 and 200 km, all with $D = 16$ ps / (nm·km). The level given by the GN model is shown as a red line.

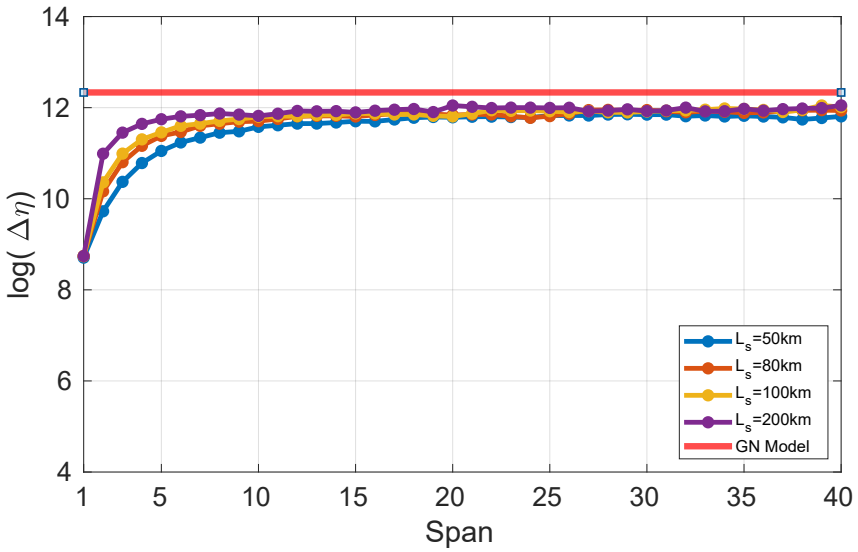

Fig. 4.3 The results of a pump-and-probe simulation campaign along a 40-span periodic OLS, for transmission of a pump with 16-QAM modulation, and a probe with QPSK modulation. Four span length scenarios are presented: L_s =50, 80, 100 and 200 km, all with $D = 16$ ps / (nm·km). The level given by the GN model is shown as a red line.

being that the modulation format determines the starting point of the $\Delta\eta$ value. It can be inferred that the different starting points produced by the two modulation formats may be explained by less dense constellations requiring a greater amount of predistortion to reach the worst-case Gaussian scenario – a behaviour which has previously been observed in [123, 125].

4.2.2 Single-Span Scenario

Following this result, the simulation campaign is extended to include a pump with predistortion applied such that its signal may be considered as Gaussian. A second subset of simulations have been launched, denoted the single-span simulations, in order to investigate how an unknown LP history affects the $\Delta\eta$ evolution. For these single-span simulations, a single fiber-amplifier pair is considered, with the signal propagated through this configuration 40 separate times, each with a different amount of predistortion applied to the pump. First, no predistortion is applied, corresponding to a LP that originates from the TX at the input of the disaggregated network segment, providing the same result as the first $\Delta\eta$ value in Figs. 4.2 and 4.3. Next, the signal is transmitted with an amount of predistortion equal to one previously crossed fiber span, then two previously crossed fiber spans, etc., upon until a value corresponding to 40 previously crossed fiber spans is reached, giving a total of 40 separate single-span simulations. These single-span simulations therefore represent every possible case for an LP with an unknown history for this scenario under investigation. For these simulations, the predistortion is applied to both the pump and the probe, and changing solely the value of predistortion for the probe was found to have no effect upon the NLI generation of the pump. A diagram illustrating the difference between the periodic and single-span scenarios is shown in Fig. 4.4.

The results of the single-span simulations for the same spectral and line configuration details as the first campaign are given in Figs. 4.5 and 4.6, with the pump transmitted with Gaussian modulation denoted the $L_s = \infty$ case, for brevity. For all investigated span lengths, the $L_s = \infty$ result was found to be near-identical, and so only the 200 km result is presented, for all cases, for readability purposes. Commenting first upon the $L_s = \infty$ scenario, the value is near-constant, besides small fluctuations due to simulation noise, and is well-approximated by the GN model, which serves as a slightly conservative upper bound.

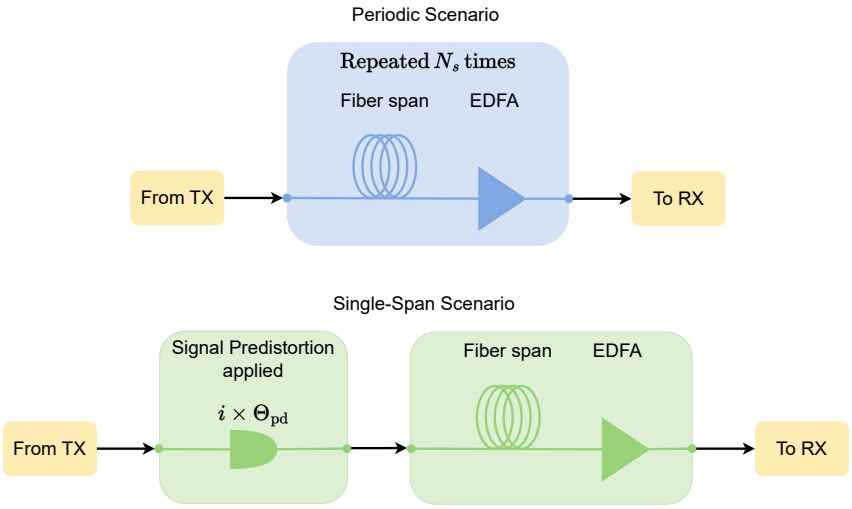

Fig. 4.4 Two diagrams which show the methodology between the periodic and single-span simulations, respectively. For the former, the signal is propagated through the entire optical system, whereas for the latter, a single span is considered at a time. Before transmission, the signal in the single-span scenario is predistorted by a value equal to transmission through a single span, Θ_{pd}, multiplied by the current considered span index, i.

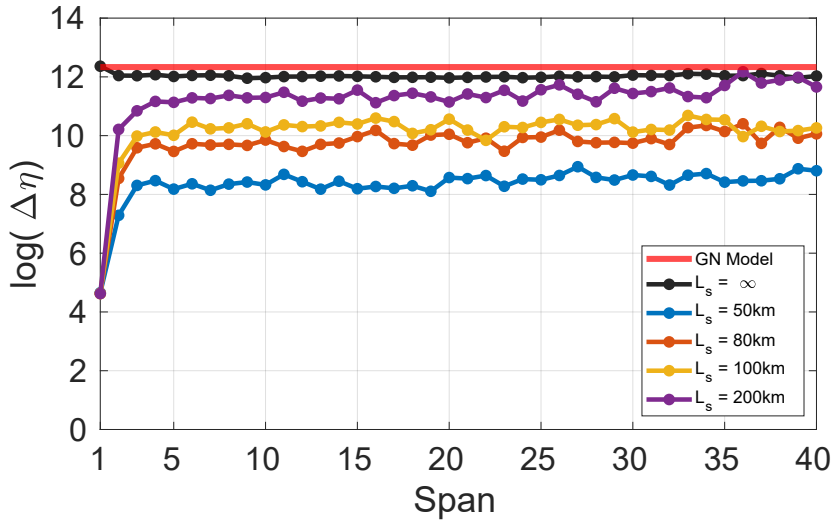

Fig. 4.5 The results of a pump-and-probe simulation campaign corresponding to 40 fiber-amplifier pairs, with a progressively increasing amount of digital predistortion applied, up to a quantity corresponding to 40 spans. Both pump and probe are transmitted with QPSK modulation. Four span length scenarios are presented: L_s =50, 80, 100 and 200 km, all with $D = 16\,\mathrm{ps}/(\mathrm{nm{\cdot}km})$. The level given by the GN model is shown as a red line, and the result for a pump transmitted with Gaussian modulation shown in black.

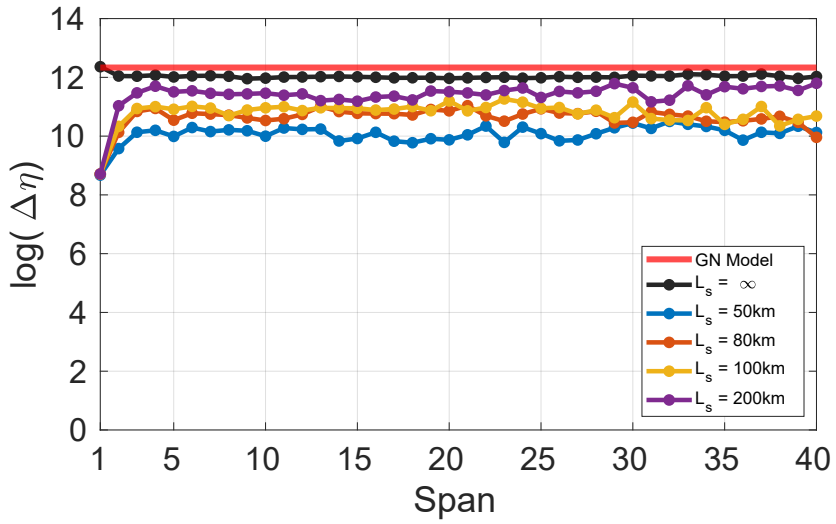

Fig. 4.6 The results of a pump-and-probe simulation campaign corresponding to 40 fiber-amplifier pairs, with a progressively increasing amount of digital predistortion applied, up to a quantity corresponding to 40 spans. The pump and probe are transmitted with 16-QAM and QPSK modulation formats, respectively. Four span length scenarios are presented: L_s =50, 80, 100 and 200 km, all with $D = 16$ ps / (nm·km). The level given by the GN model is shown as a red line, and the result for a pump transmitted with Gaussian modulation shown in black.

Concerning the single-span simulations, it is visible that $\Delta\eta$ is a quantity that depends upon L_s, with a different, constant level being attained for each L_s scenario, for both modulation formats. This difference can be primarily explained due to the differences between the effective lengths of the two fibers. For example, the difference between the $L_s = 50$ km and $L_s = 100$ km scenario is proportional to the difference between L_{eff} of these two cases. It is also visible that the difference between the asymptotic level and $L_s = \infty$ is greatest for the $L_s = 50$ km scenario, and this difference reduces as L_s is increased. This suggests that the $L_s = \infty$ scenario serves as an upper bound to the amount of NLI that can be generated between two successive fiber spans, no matter the fiber length, with this value decreasing proportional to L_{eff}. Subsequently, this implies that if the history of an LP is unknown when it enters a disaggregated network segment, it is always possible to use either the GN model or a Gaussian modulated pump simulation result as a worst case upper-bound.

4.2.3 Full Results for Other Investigated Cases

To expand the validity of the previous statement, further simulations were performed, additionally for an OLS configuration where the values of D are set to 4 and 8 ps / (nm·km), and for a pump-and-probe configuration where the pump is placed 300 GHz away from the probe. These results are presented for a spectral separation of 150 GHz and $D = 4$ and 8 ps / (nm·km) in Figs. 4.7 and 4.8, respectively, followed by a spectral separation of 300 GHz and $D = 4$ and 8 ps / (nm·km) in Figs. 4.9 and 4.10. Aside from reaffirming the observations made within the previous subsections, it also becomes evident that, outside of small amounts of variation induced by simulation noise, the single-span simulations tend to evolve equally to the periodic simulations within the first few fiber spans. This suggests that the Gaussianisation process happens uniformly independently of fiber length, spectral separation, or pump modulation format. Furthermore, observing the trends of the periodic and single-span simulations along the first few fiber spans on a macroscopic level, the single-span simulations appear to closely follow the periodic simulations, before levelling off as the maximum $\Delta\eta$ is reached. This shows that the single-span

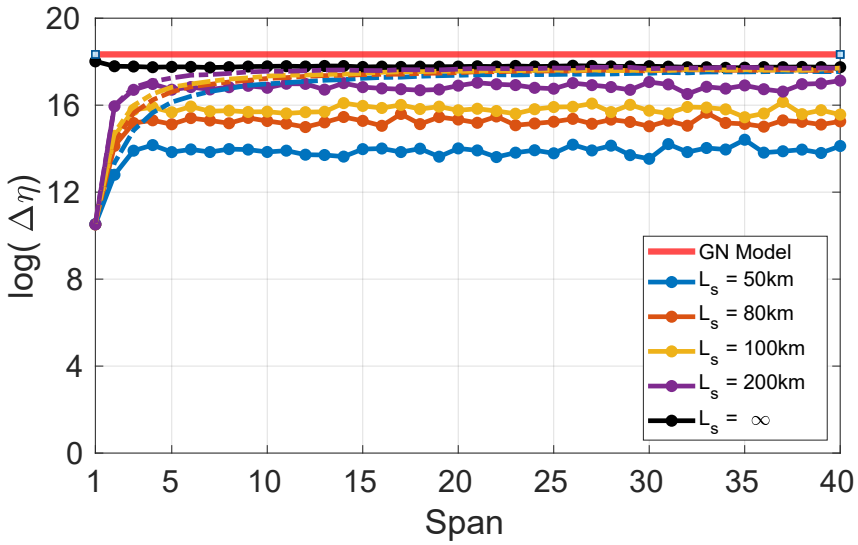

Fig. 4.7 The results of a pump-and-probe simulation campaign corresponding to 40 fiber-amplifier pairs, with a progressively increasing amount of digital predistortion applied, up to a quantity corresponding to 40 spans. Both pump and probe are transmitted with QPSK modulation, separated by 150 GHz. Four span length scenarios are presented: L_s =50, 80, 100 and 200 km, all with $D = 4$ ps / (nm·km). The level given by the GN model is shown as a red line, and the result for a pump transmitted with Gaussian modulation shown in black.

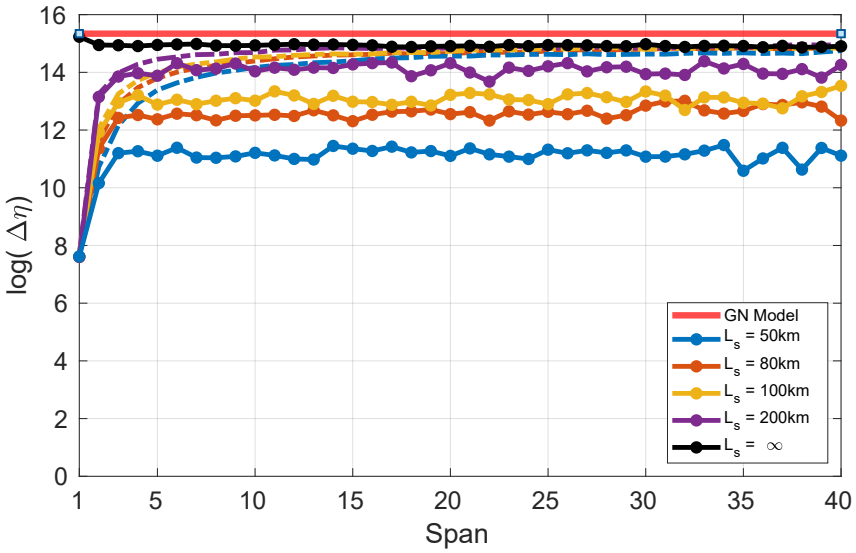

Fig. 4.8 The results of a pump-and-probe simulation campaign corresponding to 40 fiber-amplifier pairs, with a progressively increasing amount of digital predistortion applied, up to a quantity corresponding to 40 spans. Both pump and probe are transmitted with QPSK modulation, separated by 150 GHz. Four span length scenarios are presented: L_s =50, 80, 100 and 200 km, all with $D = 8$ ps / (nm·km). The level given by the GN model is shown as a red line, and the result for a pump transmitted with Gaussian modulation shown in black.

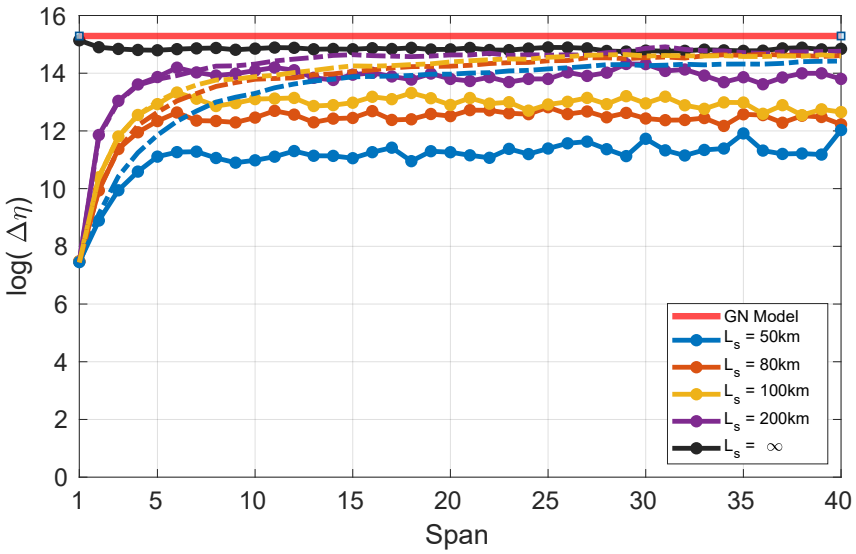

Fig. 4.9 The results of a pump-and-probe simulation campaign including the periodic (solid line) and single-span (dashed line) scenarios. Both pump and probe are transmitted with QPSK modulation, separated by 300 GHz. Four span length scenarios are presented: L_s =50, 80, 100 and 200 km, all with $D = 4$ ps / (nm·km) The level given by the GN model is shown as a red line, and the result for a pump transmitted with Gaussian modulation shown in black.

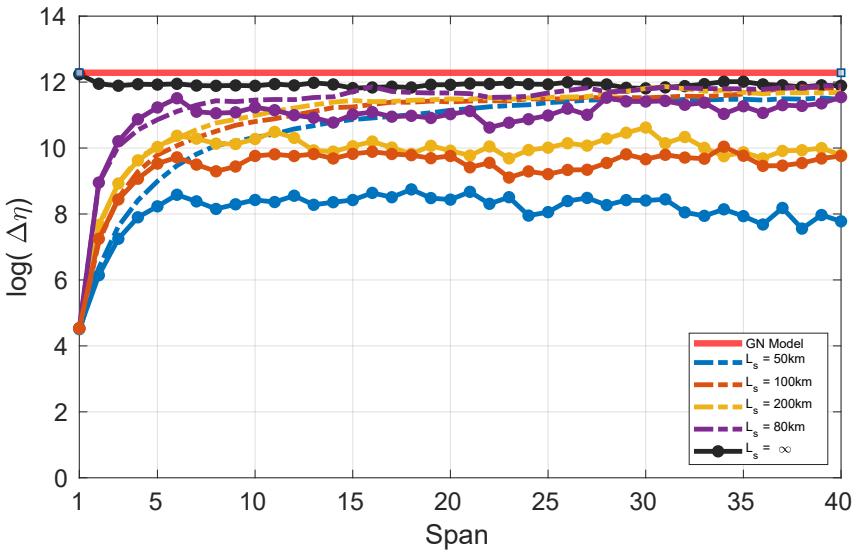

Fig. 4.10 The results of a pump-and-probe simulation campaign including the periodic (solid line) and single-span (dashed line) scenarios. Both pump and probe are transmitted with QPSK modulation, separated by 300 GHz. Four span length scenarios are presented: L_s =50, 80, 100 and 200 km, all with $D = 8$ ps / (nm·km) The level given by the GN model is shown as a red line, and the result for a pump transmitted with Gaussian modulation shown in black.

simulations experience the same form of Gaussianisation as the periodic simulations within the first few fiber spans, but after this, the behaviour is dictated solely by the fiber parameters.

4.3 Impact of Fiber Dispersion

In the previous section it has been observed that the maximum amount of NLI that can be generated for a signal propagating through a fiber span depends upon the parameters of the fiber span and the distortion of the signal, both specifically arising from the accumulated dispersion, DL_s. This has been visible for a uniform disaggregated network segment consisting of 40 fiber-amplifier pairs; the next step is now to perform an investigation upon segments which are no longer uniform, by changing the fiber dispersion, D, throughout the segment.

For this purpose, two disaggregated network segments have been modelled, each consisting of three OLSs, denoted OLS1, OLS2, and OLS3. Each of these OLSs consists of 5 fibers with uniform D values of 4, 8 or 16 ps / (nm·km), providing a total of 15 fiber spans. These OLSs are arranged to produce a disaggregated network

segment, for two distinct simulation scenarios, referred to as Scenario 1 and Scenario 2, which are described in Tab. 4.1. The order of the OLSs has been chosen such that both low-to-high and high-to-low changes in D are simulated, corresponding to: 4 to 16 ps / (nm·km) for Scenario 1, and from 16 to 4 ps / (nm·km) for Scenario 2, respectively. All fiber spans are set to a fixed length of 80 km, in order to purely observe the effect of changing D, and all other fiber parameters are set to uniform values, equal to those listed in Sec. 4.2.

For both scenarios, an identical simulation campaign has been performed that consists of three configurations: a single-channel configuration to analyze the SPM generated within the CUT bandwidth, a full-spectrum configuration to quantify the total NLI, and a series of pump-and-probe simulations, for all pumps within the full-spectrum scenario, to quantify the XPM generated by each interfering channel. By performing all constituent pump-and-probe simulations that correspond to the full-spectrum case, a superposition of the total SPM and XPM impairments is enabled, allowing these two configurations to be directly compared.

Concerning differences to the spectral parameters, the channel power, P_{ch} is set to 3 dBm for the single-channel case and for all channels within the full-spectrum case. For the pump-and-probe simulations, for the case where the probe and pump neighbour each other, the probe power is set to -5.5 dBm, which is chosen to prevent crosstalk between the pump and the probe, but still enable the probe to be properly received. For all other pumps the probe power is set to -20 dBm, and the power of the ith pump, $P_{\mathrm{ch;i}}$, is found using the following relation, in linear units:

$$P_{\mathrm{ch;i}} = \sqrt{i \cdot P_{\mathrm{ch;1}}}\,, \tag{4.3}$$

where $P_{\mathrm{ch;1}}$ is 3 dBm. This conversion ensures that an equal amount of NLI is generated for each interfering pump, producing NLI values that are significantly larger than the simulation noise floor, and permitting each pump-and-probe result to be compared directly.

Table 4.1 A summary of the two disaggregated network scenarios. Each OLS consists of 5x80 km fiber spans, each followed by a transparent amplifier.

Scenario	OLS 1	OLS 2	OLS 3
1	16 ps / (nm·km)	4 ps / (nm·km)	8 ps / (nm·km)
2	4 ps / (nm·km)	16 ps / (nm·km)	8 ps / (nm·km)

All simulation results are then scaled to the local-optimization global-optimization (LOGO) power value [181], which is calculated by considering that the optimal working point of a system from a GSNR perspective is when the NLI generation is half (3 dB lower than) the OSNR. The amplifiers are then set at this optimal working point, and information about the amplifier NF is used to provide an optimal input power value, for a scenario where all channel input powers are identical. As mentioned within Chapters 1 and 2, within wideband scenarios power optimisation is a more complex problem, but for this investigation the LOGO power corresponds closely to the optimal working point of the system, as only approximately 2 THz of the C-band spectrum is occupied. Moving beyond use of the LOGO power for wideband transmission scenarios is covered in Chapter 5.

Firstly, the single-channel results for Scenario 1 are presented in terms of $\Delta\,\mathrm{SNR_{NL}}$ in Fig. 4.11. Much like the definition given for η in Eq. 4.2, $\Delta\,\mathrm{SNR_{NL}}$ is the gradient of $\mathrm{SNR_{NL}}$, calculated by:

$$\Delta\mathrm{SNR_{NL}} = \mathrm{SNR_{NL},}_{n} - \mathrm{SNR_{NL},}_{n-1}\,. \tag{4.4}$$

The SNR is chosen as a metric rather than η within this section in order to compare each simulation result to the GSNR, which is given as a final metric. Within Fig. 4.11,

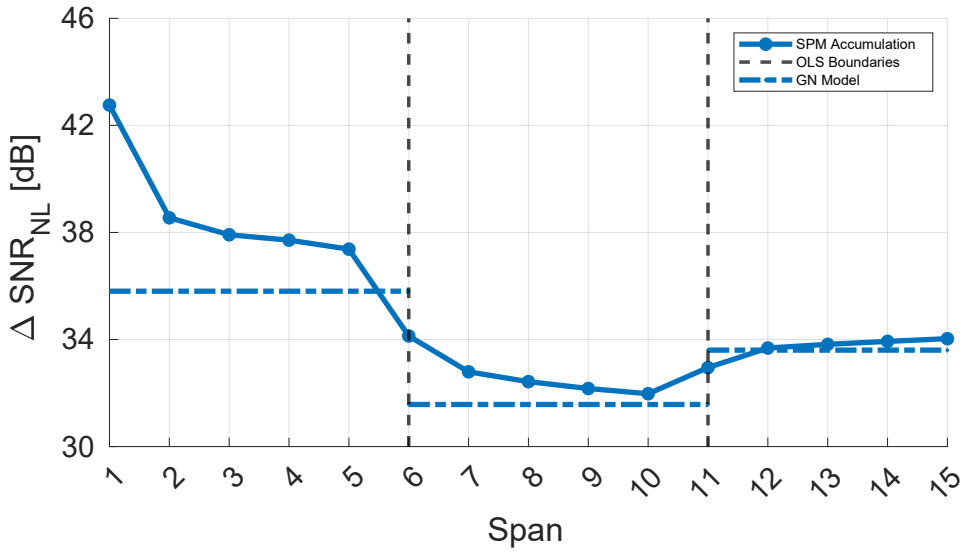

Fig. 4.11 The gradient of the $\mathrm{SNR_{NL}}$ accumulation, $\Delta\,\mathrm{SNR_{NL}}$, in Scenario 1, for a single propagating channel. The boundaries of the three OLSs are highlighted with dashed lines, and an implementation of the disaggregated GN model is shown with the blue dashed-dotted lines.

the limits of each OLS are bounded by a vertical dashed line, which corresponds to the first spans of the 2nd and 3rd OLSs. The blue dashed-dotted line corresponds to three values that are given by the disaggregated GN model presented in Chapter 2, with the coherency of the SPM taken into account by calculation of C_∞ in Eq. 2.18, and adjusting the weighting of the SPM effect accordingly. This value is found by performing three separate simulations, each corresponding to periodic transmission through 100 fiber spans, with D values of 4, 8 and 16 ps / (nm·km). The asymptotic value of the SPM is then calculated by averaging over the last 10 spans (to reduce the impact of simulation noise), with C_∞ found by taking the ratio of this value to the initial SPM. These simulations to calculate C_∞ are not presented, as the entire behaviour which they demonstrate is visible, along with other information, within Fig. 4.11: within the first two OLSs, the SPM accumulates coherently, with $\Delta\,\mathrm{SNR_{NL}}$ progressively decreasing as the signal passes through the fiber spans, rather than being at a constant level.

For all spans except the first span of OLS3, the model is conservative, giving a prediction with a level of accuracy that starts at an adequate level, and improves as the number of previously crossed fiber spans grows. It is visible that jumps in $\Delta\,\mathrm{SNR_{NL}}$ are present when the signal passes into an OLS with a different D value, with the size of this jump corresponding to the change in the maximum possible amount of NLI that may be generated in a single fiber span, similarly to what occurs when L_s is changed, as explained in Sec. 4.2. This behaviour also corresponds to the direction of the $\Delta\,\mathrm{SNR_{NL}}$ jump when D is changed: when D decreases, $\Delta\,\mathrm{SNR_{NL}}$ reduces, due to the maximum $\Delta\,\mathrm{SNR_{NL}}$ being limited, and vice versa. Furthermore, the apparent lack of coherent SPM generation within OLS3 is explained by this behaviour: within this OLS, an equilibrium is being reached that balances the effects of the SPM coherency and the jump in $\Delta\mathrm{SNR_{NL}}$ that occurs due to changing the value of D between OLSs.

Next, the pump-and-probe results for Scenario 1 are presented in Fig. 4.12. For ease of presentation, 5 pumps are selected, which correspond to the first 3 pumps nearest to the probe, along with pumps 5 and 7, showing the behaviour of the XPM as Δf is progressively increased. For each pump and D value the level given by the disaggregated GN model is calculated from Eq. 2.19, and presented in terms of $\Delta\mathrm{SNR_{NL}}$, with colours that correspond to the pump-and-probe results. Compared to the single-channel results, the $\Delta\mathrm{SNR_{NL}}$ values for the pump-and-probe results are at an approximately constant level for each pump, which is due to the incoherent

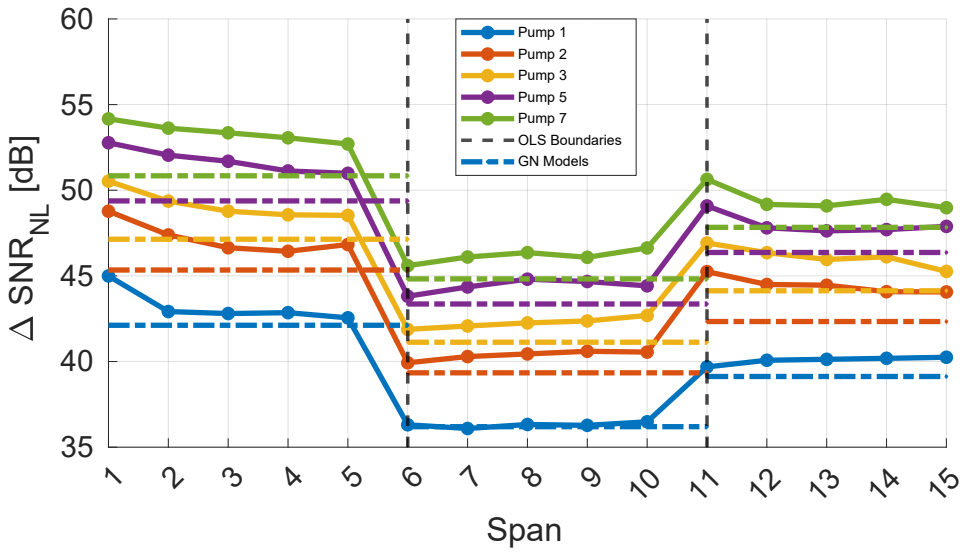

Fig. 4.12 The gradient of the $\mathrm{SNR_{NL}}$ accumulation, $\Delta\,\mathrm{SNR_{NL}}$, in Scenario 1, for 5 selected pump-and-probe simulations. The boundaries of the three OLSs are highlighted with dashed lines, and an implementation of the disaggregated GN model is shown for each pump, with dashed-dotted lines with colours that correspond to the pumps that they are modelling.

nature of the XPM. For all pumps, the disaggregated GN model provides an accurate and conservative prediction, including for when fiber dispersion is changed between OLSs, with this conservativity increasing as the spectral distance between the pump and the probe, Δf, is increased. It is also visible that increasing Δf causes small fluctuations in $\Delta\mathrm{SNR_{NL}}$, which is simply due to a proportional decrease in simulation accuracy.

Fig. 4.13 gives a side-by-side comparison of the full-spectrum results and the superposition of the SPM and XPM impairments, found by summing each constituent pump-and-probe simulation and the single-channel result. The superposition is found to correspond very well to the full-spectrum result, which gives additional verification to the spectral disaggregation hypothesis confirmed in [2, 5], and validating the disaggregated GN model, at least for bandwidths within the C-band. Furthermore, the averaging effect of the superposition helps to bypass fluctuations due to simulation inaccuracy, while still accurately presenting the general behaviour of the signal as it passes through the OLSs.

As mentioned previously, calculating power using the LOGO method assumes amplification at the optimal working points of all EDFAs, where the NLI is half the linear noise. A more broad estimation of system performance can therefore be

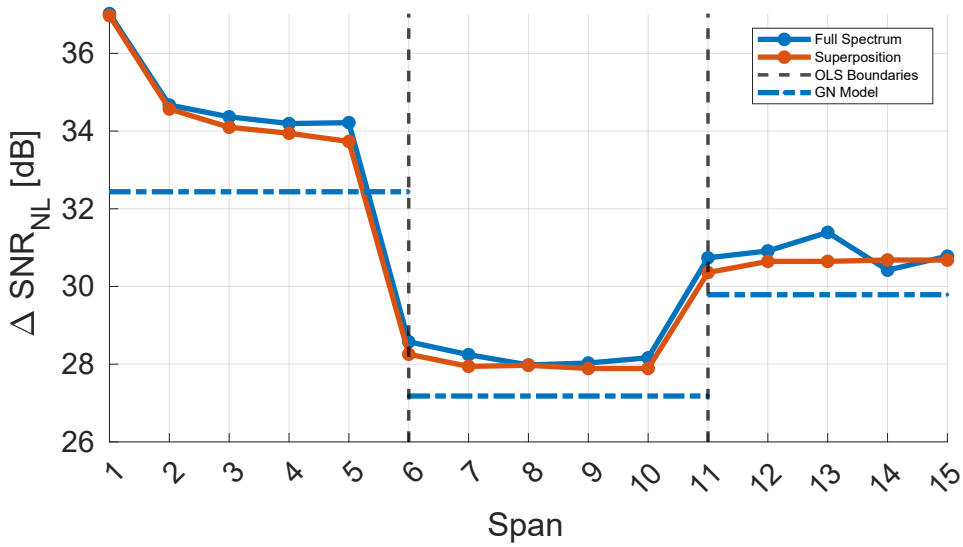

Fig. 4.13 The gradient of the $\mathrm{SNR_{NL}}$ accumulation, $\Delta\,\mathrm{SNR_{NL}}$, in Scenario 1 for the full-spectrum results, compared to a superposition of all pump-and-probe results. The boundaries of the three OLSs are highlighted with dashed lines, and an implementation of the disaggregated GN model is shown with the blue dashed-dotted lines.

calculated by inclusion of the GSNR, first by estimating the OSNR as 3 dB lower than the NLI. All of these quantities are presented in terms of $\mathrm{SNR_{NL}}$ in Fig. 4.14, along with a corresponding GSNR given by the disaggregated GN model. This figure shows that, after the addition of the OSNR, the difference between the full-spectrum scenario and the superposition is negligible, and the difference between the GN model and these results after 15 spans of propagation is approximately 0.4 dB, which provides a good level of accuracy. Similarly to the full-spectrum and superposition results in Fig. 4.13, the GN model remains conservative for all fiber spans, both in terms of $\mathrm{SNR_{NL}}$ and GSNR. Moreover, the accumulation given by the GSNR for the full-spectrum and superposition results is near-equivalent, with the green line of the former obscured by the latter. This demonstrates that any inaccuracies which arise between the full-spectrum and superposition scenarios are greatly reduced when considering the GSNR rather than the $\mathrm{SNR_{NL}}$ evolution.

For completeness, the results of Scenario 2 are presented in Figs. 4.15, 4.16, 4.17 and 4.18. Identical conclusions are reached with this fiber span configuration: a similar level of accuracy is attained, with an approximately 0.6 dB difference present between the final GSNR of the disaggregated GN model and the full-spectrum scenario, after 15 spans of propagation. The disaggregated GN model therefore

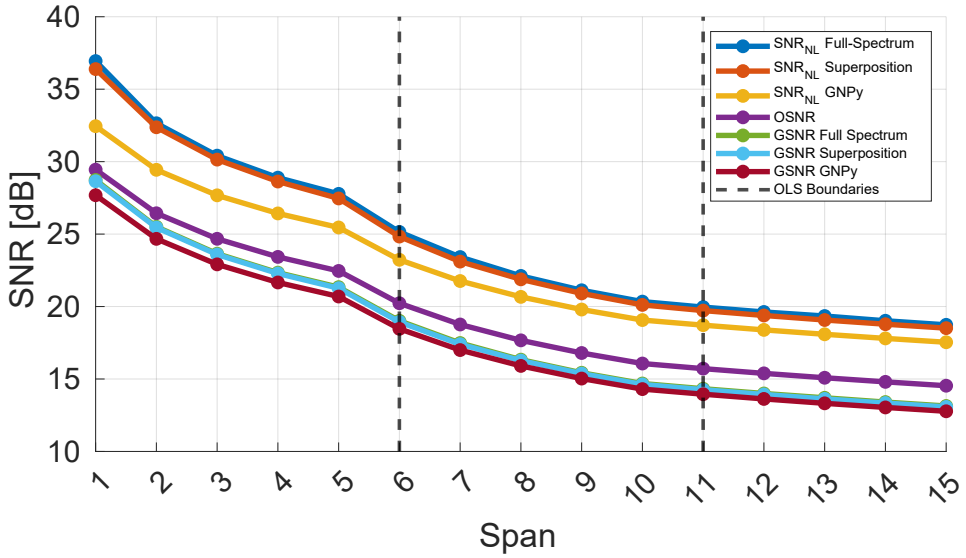

Fig. 4.14 The SNR_{NL} accumulation in Scenario 1 for the full-spectrum results, compared to a superposition of all pump-and-probe results. OSNR values are calculated by considering ideal amplification, enabling GSNR estimates for the full spectrum, superposition and GNPy simulations. The boundaries of the three OLSs are highlighted with dashed lines.

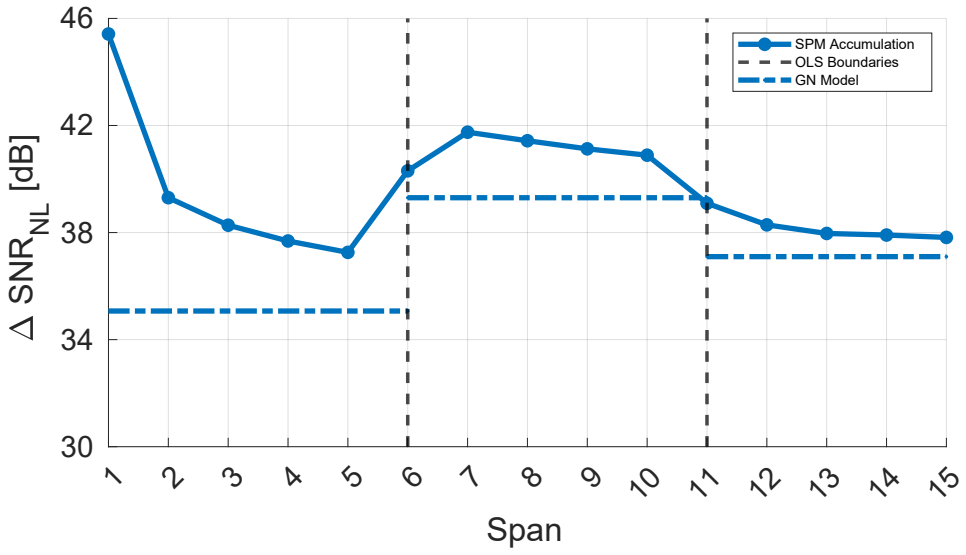

Fig. 4.15 The gradient of the SNR_{NL} accumulation, $\Delta\,SNR_{NL}$, in Scenario 2, for a single propagating channel. The boundaries of the three OLSs are highlighted with dashed lines, and an implementation of the disaggregated GN model is shown with the blue dashed-dotted lines.

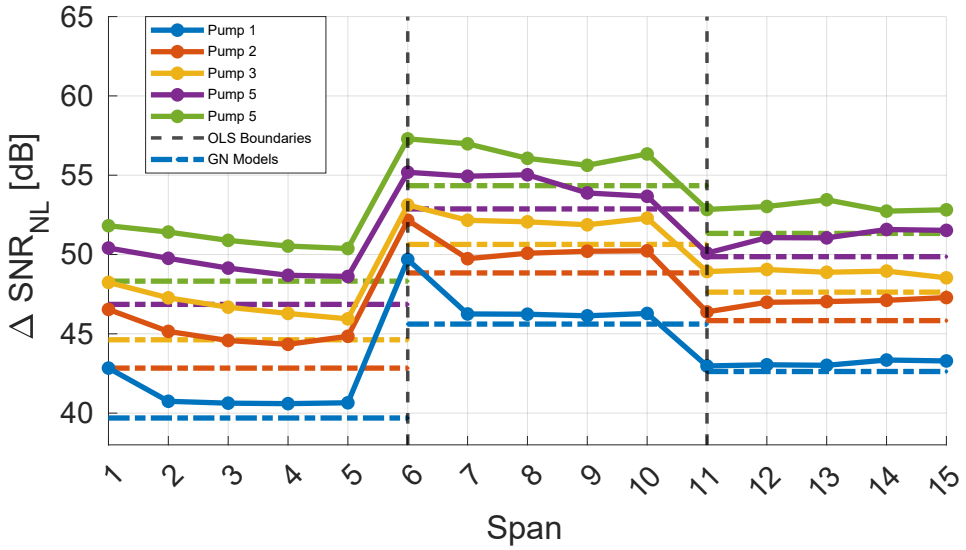

Fig. 4.16 The gradient of the SNR_{NL} accumulation, ΔSNR_{NL}, in Scenario 2, for 5 selected pump-and-probes simulations. The boundaries of the three OLSs are highlighted with dashed lines, and an implementation of the disaggregated GN model is shown for each pump, with dashed-dotted lines with colours that correspond to the pumps that they are modelling.

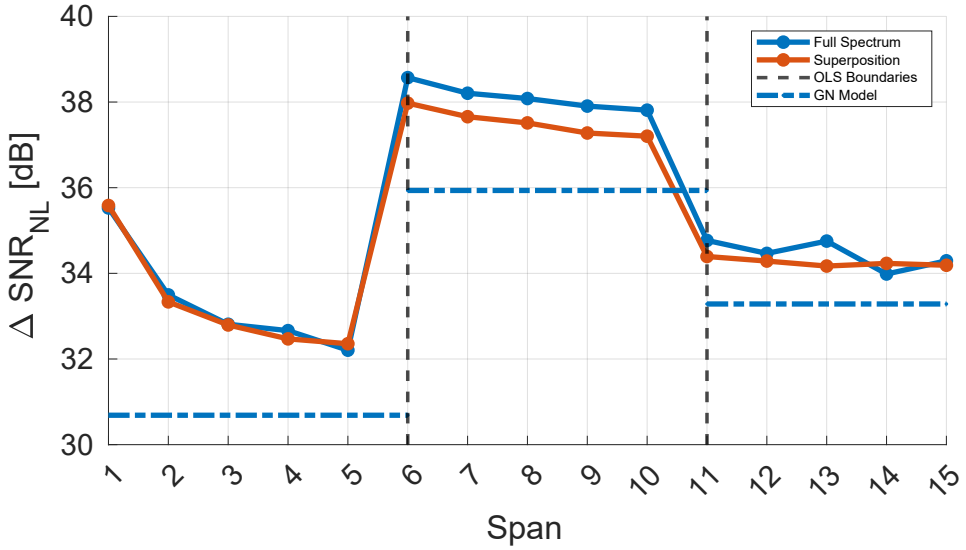

Fig. 4.17 The gradient of the SNR_{NL} accumulation, ΔSNR_{NL}, in Scenario 2 for (a): the full spectrum results, compared to a superposition of all pump-and-probe results. The boundaries of the three OLSs are highlighted with dashed lines, and an implementation of the disaggregated GN model is shown with the blue dashed-dotted lines.

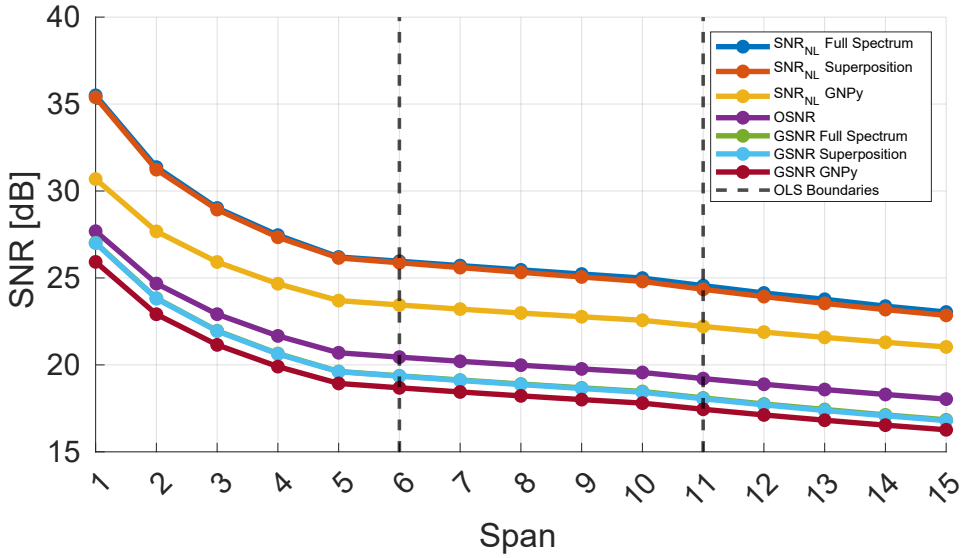

Fig. 4.18 The SNR_{NL} accumulation in Scenario 2 for the full spectrum results, compared to a superposition of all pump-and-probe results. OSNR values are calculated by considering ideal amplification, enabling GSNR estimates for the full spectrum, superposition and GNPy simulations.The boundaries of the three OLSs are highlighted with dashed lines.

provides an accurate and conservative upper bound to the NLI generation for all interfering channels, within both disaggregated network segment configurations.

4.4 Impact of Residual Dispersion

Following the investigations of how L_s and D affect the NLI accumulation within a disaggregated network, attention now turns to how the relation between these parameters and the NLI generation is altered in cases where in-line dispersion compensation is performed. In these scenarios, rather than compensating for dispersion with end-of-line DSP, DCUs are placed directly within the line after each fiber span, aiming to fully compensate the dispersion that is induced during transmission. Despite less spectral efficiency than coherent transmission, many metro and access networks still make use of in-line dispersion compensation and IMDD signals. These networks may be progressively upgraded towards coherent and dual polarisation transmission, but in some cases it may be too costly or not yet worth the effort, creating scenarios where IMDD and coherent signals propagate alongside each other [103]. The result is that QoT estimation of coherent signals passing through links with in-line

dispersion compensation is something which should not be overlooked, particularly in the case of disaggregated networking, where this may occur within disaggregated network segments.

The amount of dispersion compensated for by the DCUs may be slightly different to that of the preceding fiber span, which produces small amounts of residual dispersion. As shown in in Sec. 4.3, differences in dispersion have an effect upon the maximum amount of NLI which may be generated for a given system, meaning that this residual dispersion will affect the NLI generation. Concerning the SPM contribution to the NLI, the effects of residual dispersion have been investigated in [182], demonstrating that it changes the SPM accumulation. Regarding the XPM contribution, this has been investigated as part of this thesis in [6], which is presented in this section.

A SSFM simulation campaign has been created that consists of a variety of pump-and-probe simulations, for multiple spectral and line configurations, in order to investigate the impact of residual dispersion upon the accumulation of the XPM. These simulations are performed over a disaggregated network segment that consists of two distinct OLSs, denoted OLS1 and OLS2, which both feature in-line dispersion compensation in the form of DCUs. The scenario of an unknown LP history has been covered in Sec. 4.2, and consequently the signal is set to originate at the input of OLS1 to isolate the impact of residual dispersion.

4.4.1 Simulation Settings

An example line configuration for the two OLSs is shown in Fig, 4.19: each OLS has all variable parameters listed beneath the corresponding optical component that features them, with a corresponding index of 1 for OLS1, and 2 for OLS2. The fiber dispersion, D, is varied on a per-simulation basis, with an equal value for every fiber span, for a given configuration. Each fiber is followed by an EDFA that operates within transparency, with G set such that the fiber loss is fully recovered. After the amplifier a DCU module is placed, compensating for D and producing a small amount of residual dispersion, D_{RES}, given by:

$$D_{\mathrm{RES}} = DL_s + D_{\mathrm{DCU}} \,, \tag{4.5}$$

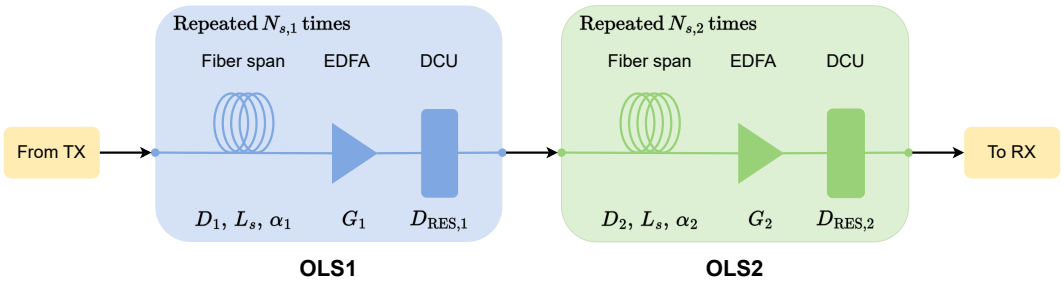

Fig. 4.19 A SSFM line configuration that corresponds to a disaggregated optical network segment. This segment is composed of two OLSs that feature in-line dispersion compensation in the form of DCUs.

where D is the dispersion of the preceding fiber span, in ps / (nm·km). D_{RES} values of 40, 80, and 160 ps / (nm·km) have been investigated, representing realistic residual dispersion values that may be present within uncompensated links.

After the signal has passed through the first fiber-amplifier-DCU section, it then passes successively into $N_{s,1} = 10$ other sections with the same format and line elements. The signal then passes into OLS2, which consists of $N_{s,2} = 20$ successive sections, all characterized by values of D_2, G_2, and D_{RES}. After this, the signal is then considered to have reached the destination node, passing into the RX side of the SSFM for processing and analysis. The choice of 10 spans for OLS1 and 20 spans for OLS2 is motivated solely to best observe the behavior of the XPM accumulation, such that any macroscopic trends are fully visible. With regards to the fiber attenuation, α_1 and α_2 are always set to be equal, and two values have been investigated: $\alpha = 0.2$ and $\alpha = 0.15$ dB / km, with the former presented first within the investigation. For L_s, values were set to be either 80 or 50 km, with the former representing the standard investigated case. For all scenarios, γ was set to a value of 0.00127 W^{-1} km^{-1}, for all fiber spans. Two distinct chromatic dispersion configurations are considered: $D = 4$ and 16 ps / (nm·km), for the first and second OLSs, respectively, and vice versa.

In terms of spectral parameters, the R_s of both the probe and pump are set equally to be either 32 or 64 GBaud, both with 16-QAM modulation formats, and powers set to $P_{\mathrm{CUT}} = -20$ and $P_{\mathrm{ch}} = 1$ dBm, respectively. The spectral separation of the probe and pump is chosen to be either 75 and 150 GHz for the $R_s = 32$ GBaud case, and either 150 and 300 GHz for the $R_s = 64$ GBaud case, which correspond to pumps with indices of 2 and 4 for spectral separations of 37.5 and 75 GHz, respectively. For

all scenarios, the probe is located at 193.9 THz, and the pump is placed at a higher frequency with respect to the probe. Equally to Sec. 4.3, $\Delta\text{SNR}_{\text{NL}}$ is used as an overall metric, and as only the XPM is investigated within this section, this quantity corresponds to the normalised XPM power (see Eq. 2.22).

4.4.2 Investigating XPM Accumulation

Similar to the methodology of Sec. 4.2, two distinct simulation subsets have been performed which correspond to the periodic and single-span, both having a similar implementation and purpose as with this earlier section. In the periodic scenario, the signal is propagated through the entire network segment, starting at the input of OLS1 and terminating at the output of OLS2, in order to observe the effect which the residual dispersion has upon the XPM generation. The single-span scenarios correspond to signal propagation through a single fiber-DCU-amplifier section at a time, with the 1st result corresponding to propagation solely through the 1st fiber-DCU-amplifier section. This process is repeated for every constituent fiber-DCU-amplifier section until a result has been attained for every section within both OLSs. These simulations are performed in order to provide a reference scenario where the residual dispersion has no effect upon the propagating signal, by switching on the Kerr effect one span at a time and considering that all other spans undergo lossless propagation. Additionally, the level given by the disaggregated GN model has been calculated for each OLS, representing the predicted accumulation of the XPM for a completely incoherent signal.

Starting with the $R_s = 32\,\text{GBaud}$, $\Delta f = 75\,\text{GHz}$ scenario, the first results of this simulation campaign are presented in Figs. 4.20 and 4.21, showing the two scenarios where $\text{D}_{\text{RES}} = 40\,\text{ps}/\text{nm}$. Within these plots, four different methods of calculating the XPM are presented. The blue and red lines represent two periodic cases, where the propagating signal starts from the inputs of OLS1 and OLS2, respectively. These scenarios show the aggregated effect of the XPM, evolving span-by-span, along with any additional impairments that arise due to the presence of residual dispersion. In green, the results of the single-span simulations are shown, whereas in black the results of the disaggregated GN model for a single fiber span are given, calculated using GNPy and extrapolated along each OLS. For these two latter cases, the XPM is fully incoherent, and no relation between the XPM of spans i and $i-1$ is observed.

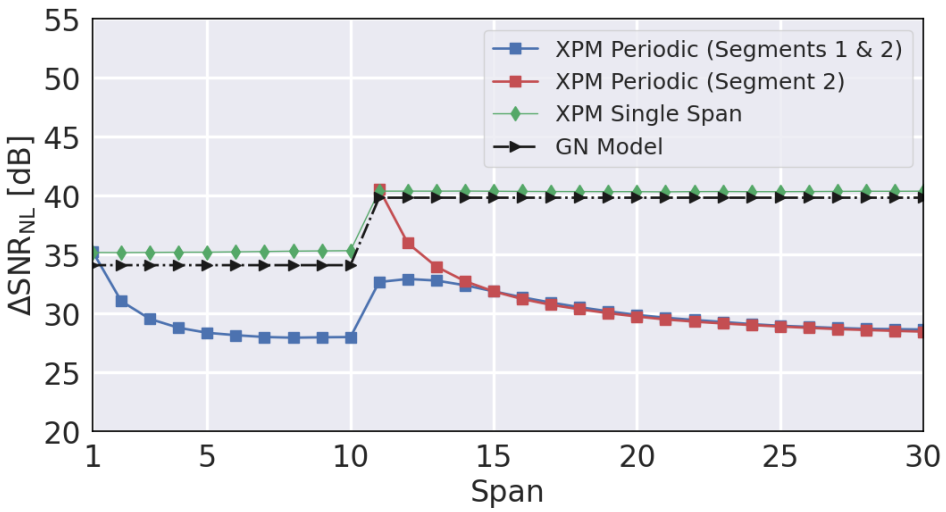

Fig. 4.20 The $\Delta\text{SNR}_{\text{NL}}$ versus span index for a single interfering pump, with $\Delta f = 150\,\text{GHz}$ and $R_s = 32\,\text{GBaud}$, through a dispersion-managed segment. Results are presented for the entire segment (blue lines), for the final 20 spans (red lines), each span evaluated independently (green lines) and a GN model implementation (black dashed lines), for $\alpha = 0.2\,\text{dB}/\text{km}$, $L_s = 80\,\text{km}$, $D_1 = 4\,\text{ps}/(\text{nm}\cdot\text{km})$, $D_2 = 16\,\text{ps}/(\text{nm}\cdot\text{km})$, and $D_{\text{RES}} = 40\,\text{ps}/\text{nm}$.

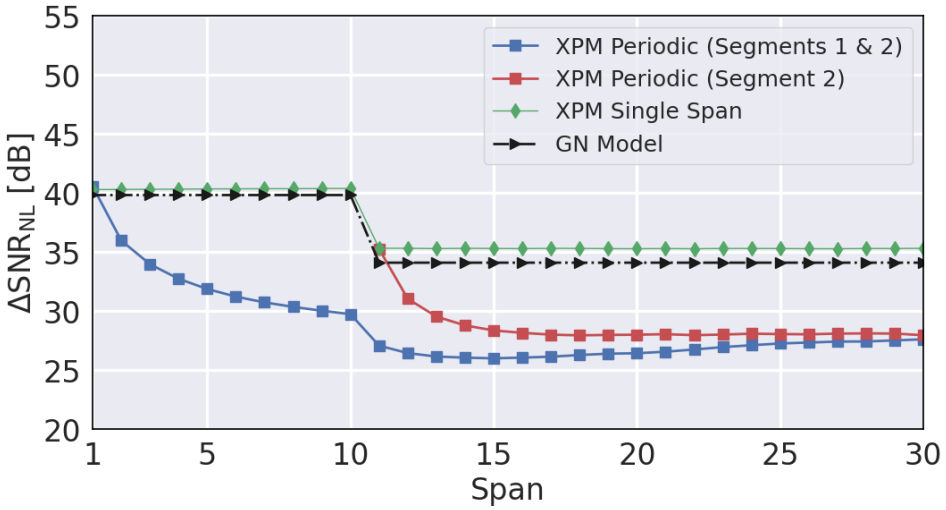

Fig. 4.21 The $\Delta\text{SNR}_{\text{NL}}$ versus span index for a single interfering pump, with $\Delta f = 150\,\text{GHz}$ and $R_s = 32\,\text{GBaud}$, through a dispersion-managed segment. Results are presented for the entire segment (blue lines), for the final 20 spans (red lines), each span evaluated independently (green lines) and a GN model implementation (black dashed lines), for $\alpha = 0.2\,\text{dB}/\text{km}$, $L_s = 80\,\text{km}$, $D_1 = 16\,\text{ps}/(\text{nm}\cdot\text{km})$, $D_2 = 4\,\text{ps}/(\text{nm}\cdot\text{km})$, and $D_{\text{RES}} = 40\,\text{ps}/\text{nm}$.

These two results are in good agreement, as would be expected for a scenario without residual dispersion present within the link.

Moving onto the results of the periodic scenarios, in Fig. 4.20, where $D_1 = 4\,\mathrm{ps/(nm{\cdot}km)}$ and $D_2 = 16\,\mathrm{ps/(nm{\cdot}km)}$, it is visible that within the first 10 spans of OLS1, the $\Delta\mathrm{SNR}_{\mathrm{NL}}$ value starts at the same point as the single-span simulations, before quickly reducing, and eventually reaching a stable equilibrium, or asymptote. The implication of this is that, for a scenario featuring residual dispersion introduced by DCUs, the total XPM introduced by each span cannot be accurately estimated by the disaggregated GN model, which overestimates it by several dB, and is no longer conservative. Considering the final 20 spans in Fig. 4.20, the value of $\Delta\mathrm{SNR}_{\mathrm{NL}}$ for the periodic scenario that starts from OLS1 (blue curve) jumps up as the signal passes into OLS2, before slowly decreasing once more towards the same asymptote encountered within OLS1. For the periodic scenario starting from OLS2 (red curve) a similar behavior is seen, except for a different accumulation within the first few fiber spans. This reveals two important points: firstly, the residual dispersion causes the XPM accumulation to experience a memory effect, where the result of a given span depends upon those preceding it, preventing the XPM from being described as purely incoherent. This also implies that there may be a significant underestimation of the XPM if the GN model is used to model a dispersion-managed segment with a sufficiently low residual dispersion. Secondly, the asymptote of the XPM accumulation depends only upon the parameters of the fiber spans located within the first OLS.

Considering next Fig. 4.21, where $D_1 = 16\,\mathrm{ps/(nm{\cdot}km)}$ and $D_2 = 4\,\mathrm{ps/(nm{\cdot}km)}$, a similar but opposite behavior is observed; initially, the XPM accumulates towards an asymptotic value, and $\Delta\mathrm{SNR}_{\mathrm{NL}}$ jumps downwards when the signal passes into OLS2, followed by an increase towards the OLS1 asymptote. Much like the $D_1 = 4\,\mathrm{ps/(nm{\cdot}km)}$ case, increasing the residual dispersion within the system reduces the discrepancy between the observed XPM accumulation and the disaggregated GN model. This demonstrates a similar behaviour to the one observed within Sec. 4.2, which showed that the maximum amount of NLI that can be generated for a given fiber span configuration depends upon the fiber dispersion value. It is visible that this change in value has a somewhat delayed effect for a system with in-line dispersion compensation, with the jumps producing a shift in the NLI generation that slowly reaches the equilibrium due to the presence of residual dispersion within the system.

The results for the same configuration, but with $D_{\mathrm{RES}} = 80\,\mathrm{ps/nm}$ are presented in Figs. 4.22 and 4.23. The behaviour is observed to be very similar to the $D_{\mathrm{RES}} = 40\,\mathrm{ps/nm}$, except that the accumulation in the periodic case reaches that of the asymptotic level faster. This effect is visible to an even greater extent when $D_{\mathrm{RES}} = 160\,\mathrm{ps/nm}$ is considered, shown in Figs. 4.24 and 4.25, where the accumulation almost immediately tends towards the asymptotic level. These results suggest that, as D_{RES} is increased, eventually a level is reached that corresponds to a fully compensated transmission scenario, and the most significant impacts upon NLI generation occur when D_{RES} is small.

Further minor investigations were performed to investigate what happens when D_{RES} values are set to be larger than 160 ps/nm and smaller than 40 ps/nm. For the former, the XPM accumulation very quickly falls/rises to the level given by the GN model as a result of the residual dispersion being large enough that no correlation is observed between successive fiber spans. Practically, these results present identical behaviour to those observed within Figs. 4.24 and 4.25. For D_{RES} values smaller than 40 ps/nm, the number of spans required to reach the asymptotic level progressively rose to a level which could not be observed within 20 spans, with the amount of XPM generated for each span being significantly different up to and presumably

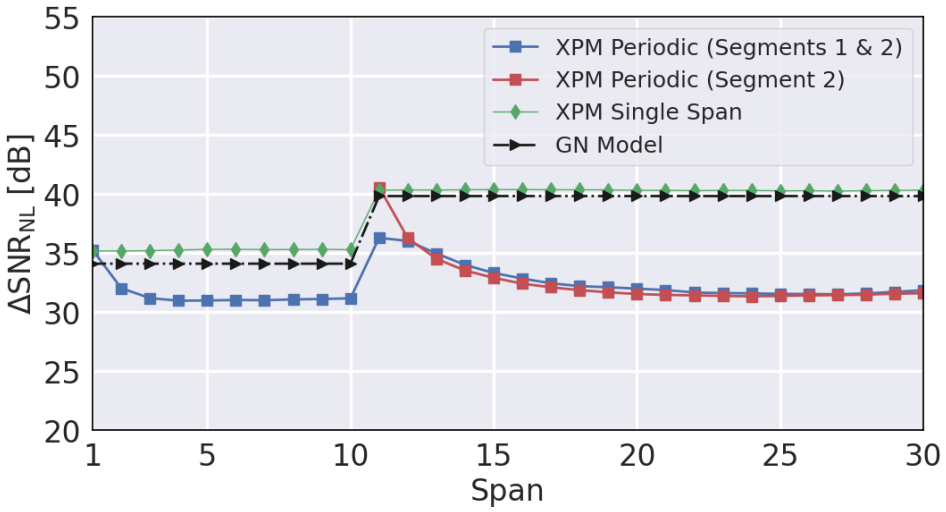

Fig. 4.22 The $\Delta\mathrm{SNR}_{\mathrm{NL}}$ versus span index for a single interfering pump, with $\Delta f = 150\,\mathrm{GHz}$ and $R_s = 32\,\mathrm{GBaud}$, through a dispersion-managed segment. Results are presented for the entire segment (blue lines), for the final 20 spans (red lines), each span evaluated independently (green lines) and a GN model implementation (black dashed lines), for $\alpha = 0.2\,\mathrm{dB/km}$, $L_s = 80\,\mathrm{km}$, $D_1 = 4\,\mathrm{ps/(nm{\cdot}km)}$, $D_2 = 16\,\mathrm{ps/(nm{\cdot}km)}$, and $D_{\mathrm{RES}} = 80\,\mathrm{ps/nm}$.

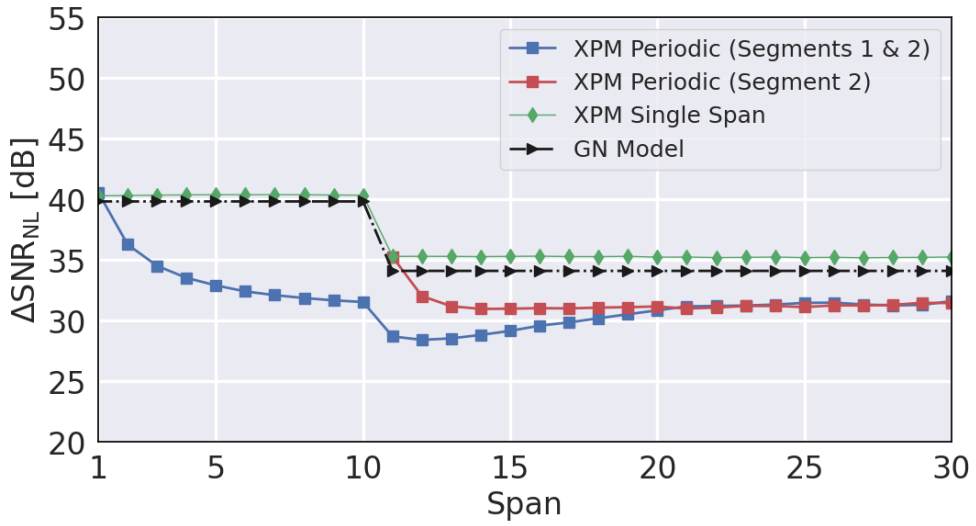

Fig. 4.23 The $\Delta\text{SNR}_{\text{NL}}$ versus span index for a single interfering pump, with $\Delta f = 150\,\text{GHz}$ and $R_s = 32\,\text{GBaud}$, through a dispersion-managed segment. Results are presented for the entire segment (blue lines), for the final 20 spans (red lines), each span evaluated independently (green lines) and a GN model implementation (black dashed lines), for $\alpha = 0.2\,\text{dB}/\text{km}$, $L_s = 80\,\text{km}$, $D_1 = 16\,\text{ps}/(\text{nm}\cdot\text{km})$, $D_2 = 4\,\text{ps}/(\text{nm}\cdot\text{km})$, and $D_{\text{RES}} = 80\,\text{ps}/\text{nm}$.

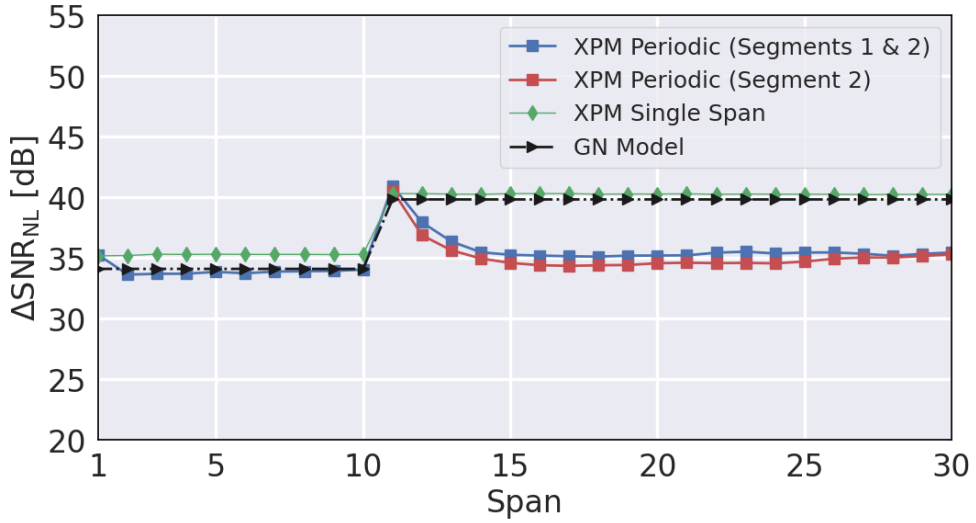

Fig. 4.24 The $\Delta\text{SNR}_{\text{NL}}$ versus span index for a single interfering pump, with $\Delta f = 150\,\text{GHz}$ and $R_s = 32\,\text{GBaud}$, through a dispersion-managed segment. Results are presented for the entire segment (blue lines), for the final 20 spans (red lines), each span evaluated independently (green lines) and a GN model implementation (black dashed lines), for $\alpha = 0.2\,\text{dB}/\text{km}$, $L_s = 80\,\text{km}$, $D_1 = 4\,\text{ps}/(\text{nm}\cdot\text{km})$, $D_2 = 16\,\text{ps}/(\text{nm}\cdot\text{km})$, and $D_{\text{RES}} = 160\,\text{ps}/\text{nm}$.

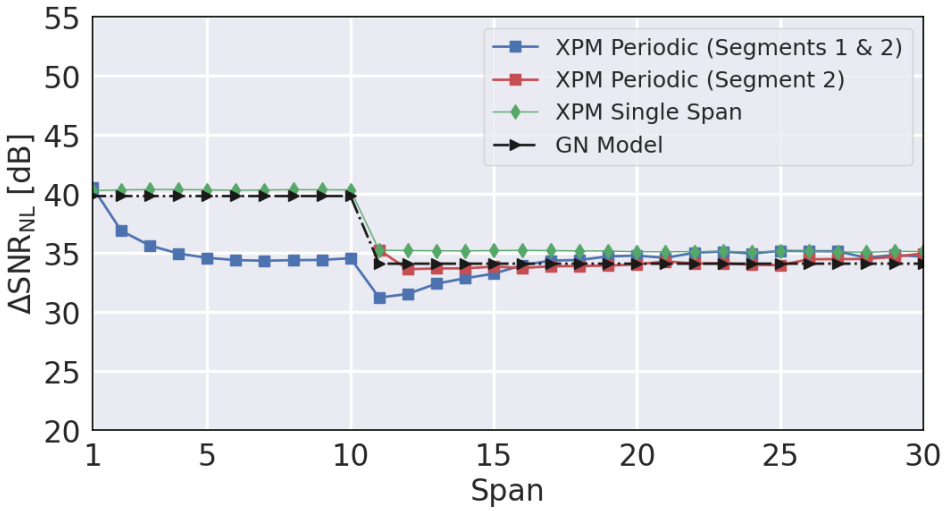

Fig. 4.25 The $\Delta\text{SNR}_{\text{NL}}$ versus span index for a single interfering pump, with $\Delta f = 150\,\text{GHz}$ and $R_s = 32\,\text{GBaud}$, through a dispersion-managed segment. Results are presented for the entire segment (blue lines), for the final 20 spans (red lines), each span evaluated independently (green lines) and a GN model implementation (black dashed lines), for $\alpha = 0.2\,\text{dB}\,/\,\text{km}$, $L_s = 80\,\text{km}$, $D_1 = 16\,\text{ps}\,/\,(\text{nm}{\cdot}\text{km})$, $D_2 = 4\,\text{ps}\,/\,(\text{nm}{\cdot}\text{km})$, and $D_{\text{RES}} = 160\,\text{ps}\,/\,\text{nm}$.

beyond this point. This scenario is therefore deemed to present behaviour that is wholly unphysical, or representative of unrealistic operating scenarios, and these results are not presented. For completeness, a selection of results corresponding to scenarios where $\Delta f = 300\,\text{GHz}$, $\alpha = 0.15\,\text{dB}\,/\,\text{km}$, $L_s = 50\,\text{km}$, and when the pump and probe are transmitted with $R_s = 64\,\text{GBaud}$ are presented in Figs. 4.26 – 4.33.

All of these configurations present identical behaviour to that which has been observed within the previous figures, aside from small fluctuations in the accumulation after the dispersion value changes, which may be attributed to simulation noise, and in some cases, the rate at which the accumulation reaches the asymptote. Furthermore, shifts in $\Delta\text{SNR}_{\text{NL}}$ are visible in some scenarios that correspond exactly to the changes in L_{eff} or α within the fiber parameters. These small differences in behaviour may be wholly attributed to the changes in simulation settings, and demonstrate that the behaviour observed and explained within Figs. 4.20 and 4.21 applies to all other simulation configurations investigated within this section.

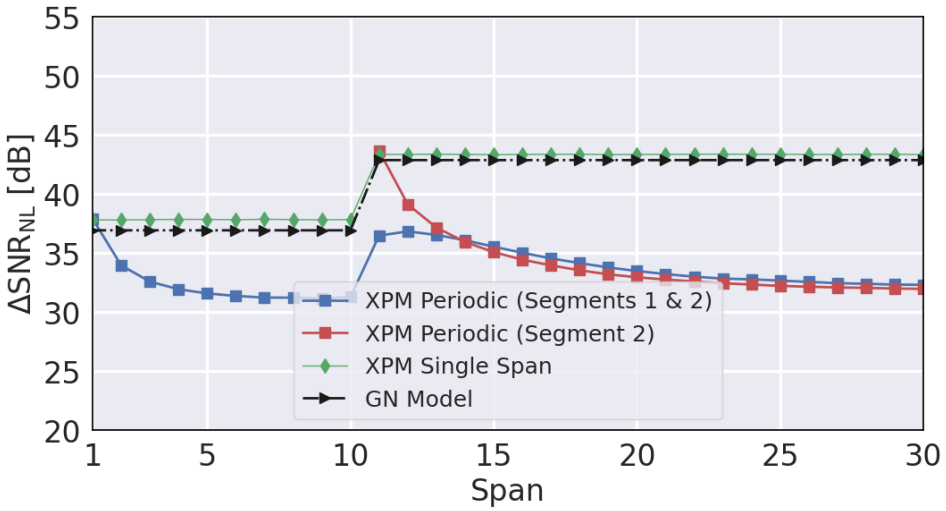

Fig. 4.26 The $\Delta\text{SNR}_{\text{NL}}$ versus span index for a single interfering pump, with $\Delta f = 300\,\text{GHz}$ and $R_s = 32\,\text{GBaud}$, through a dispersion-managed segment. Results are presented for the entire segment (blue lines), for the final 20 spans (red lines), each span evaluated independently (green lines) and a GN model implementation (black dashed lines), for $\alpha = 0.2\,\text{dB}/\text{km}$, $L_s = 80\,\text{km}$, $D_1 = 4\,\text{ps}/(\text{nm}\cdot\text{km})$, $D_2 = 16\,\text{ps}/(\text{nm}\cdot\text{km})$, and $D_{\text{RES}} = 160\,\text{ps}/\text{nm}$.

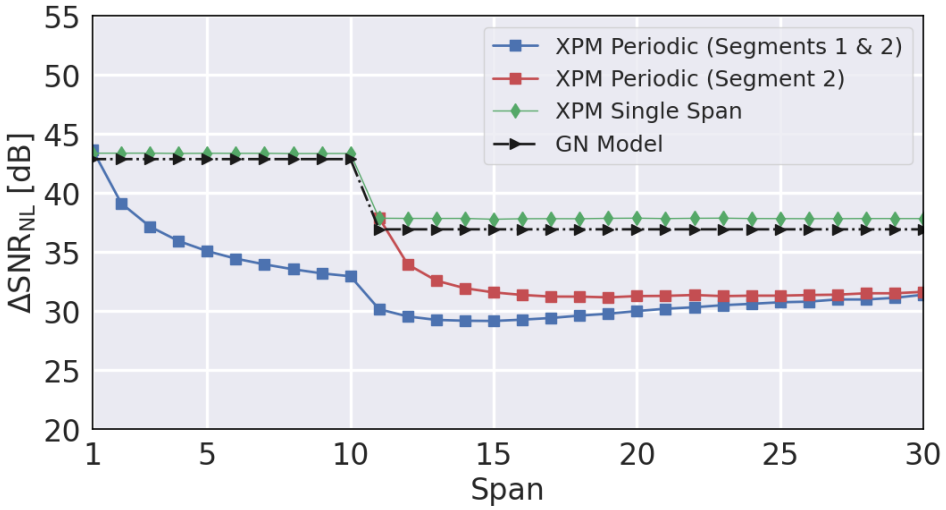

Fig. 4.27 The $\Delta\text{SNR}_{\text{NL}}$ versus span index for a single interfering pump, with $\Delta f = 300\,\text{GHz}$ and $R_s = 32\,\text{GBaud}$, through a dispersion-managed segment. Results are presented for the entire segment (blue lines), for the final 20 spans (red lines), each span evaluated independently (green lines) and a GN model implementation (black dashed lines), for $\alpha = 0.2\,\text{dB}/\text{km}$, $L_s = 80\,\text{km}$, $D_1 = 16\,\text{ps}/(\text{nm}\cdot\text{km})$, $D_2 = 4\,\text{ps}/(\text{nm}\cdot\text{km})$, and $D_{\text{RES}} = 160\,\text{ps}/\text{nm}$.

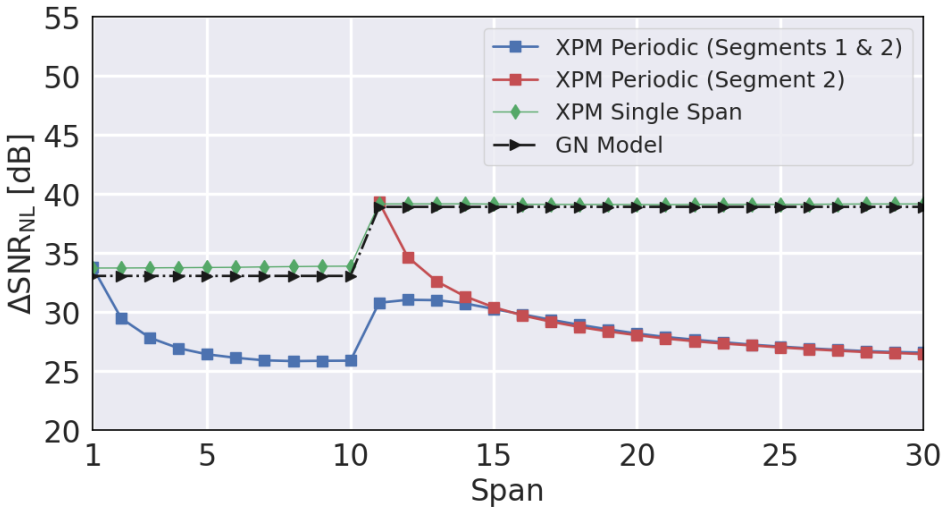

Fig. 4.28 The $\Delta\text{SNR}_{\text{NL}}$ versus span index for a single interfering pump, with $\Delta f = 150\,\text{GHz}$ and $R_s = 32\,\text{GBaud}$, through a dispersion-managed segment. Results are presented for the entire segment (blue lines), for the final 20 spans (red lines), each span evaluated independently (green lines) and a GN model implementation (black dashed lines), for $\alpha = 0.15\,\text{dB}/\text{km}$, $L_s = 80\,\text{km}$, $D_1 = 4\,\text{ps}/(\text{nm}\cdot\text{km})$, $D_2 = 16\,\text{ps}/(\text{nm}\cdot\text{km})$, and $D_{\text{RES}} = 160\,\text{ps}/\text{nm}$.

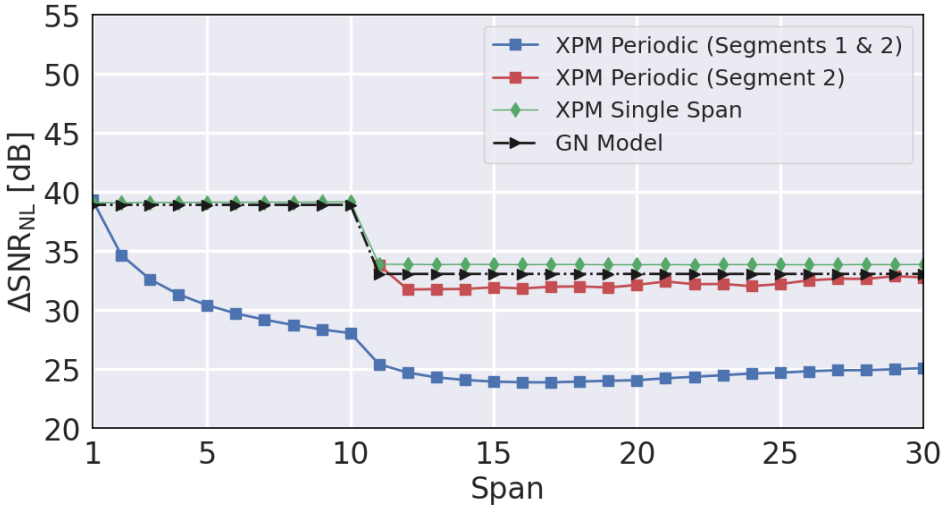

Fig. 4.29 The $\Delta\text{SNR}_{\text{NL}}$ versus span index for a single interfering pump, with $\Delta f = 150\,\text{GHz}$ and $R_s = 32\,\text{GBaud}$, through a dispersion-managed segment. Results are presented for the entire segment (blue lines), for the final 20 spans (red lines), each span evaluated independently (green lines) and a GN model implementation (black dashed lines), for $\alpha = 0.15\,\text{dB}/\text{km}$, $L_s = 80\,\text{km}$, $D_1 = 16\,\text{ps}/(\text{nm}\cdot\text{km})$, $D_2 = 4\,\text{ps}/(\text{nm}\cdot\text{km})$, and $D_{\text{RES}} = 160\,\text{ps}/\text{nm}$.

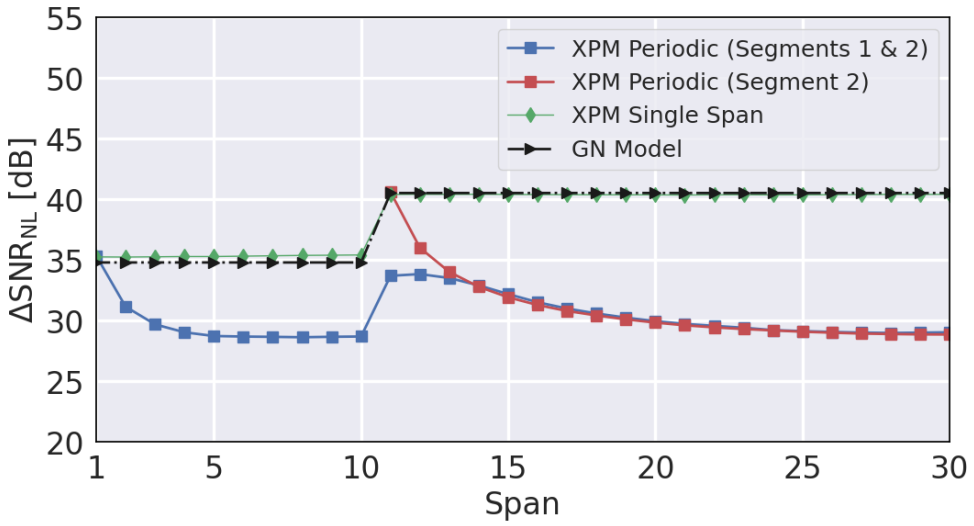

Fig. 4.30 The $\Delta\text{SNR}_{\text{NL}}$ versus span index for a single interfering pump, with $\Delta f = 150\,\text{GHz}$ and $R_s = 32\,\text{GBaud}$, through a dispersion-managed segment. Results are presented for the entire segment (blue lines), for the final 20 spans (red lines), each span evaluated independently (green lines) and a GN model implementation (black dashed lines), for $\alpha = 0.2\,\text{dB}/\text{km}$, $L_s = 50\,\text{km}$, $D_1 = 4\,\text{ps}/(\text{nm}\cdot\text{km})$, $D_2 = 16\,\text{ps}/(\text{nm}\cdot\text{km})$, and $D_{\text{RES}} = 160\,\text{ps}/\text{nm}$.

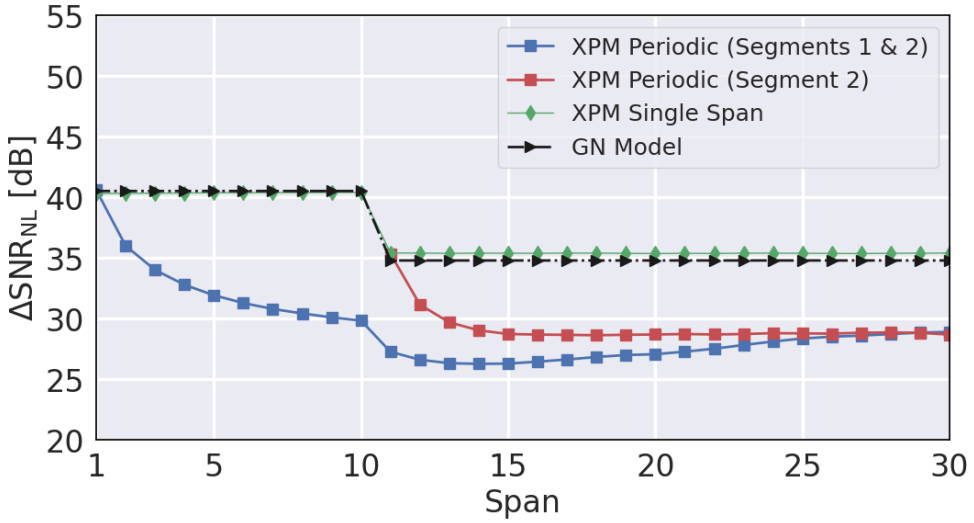

Fig. 4.31 The $\Delta\text{SNR}_{\text{NL}}$ versus span index for a single interfering pump, with $\Delta f = 150\,\text{GHz}$ and $R_s = 32\,\text{GBaud}$, through a dispersion-managed segment. Results are presented for the entire segment (blue lines), for the final 20 spans (red lines), each span evaluated independently (green lines) and a GN model implementation (black dashed lines), for $\alpha = 0.2\,\text{dB}/\text{km}$, $L_s = 50\,\text{km}$, $D_1 = 16\,\text{ps}/(\text{nm}\cdot\text{km})$, $D_2 = 4\,\text{ps}/(\text{nm}\cdot\text{km})$, and $D_{\text{RES}} = 160\,\text{ps}/\text{nm}$.

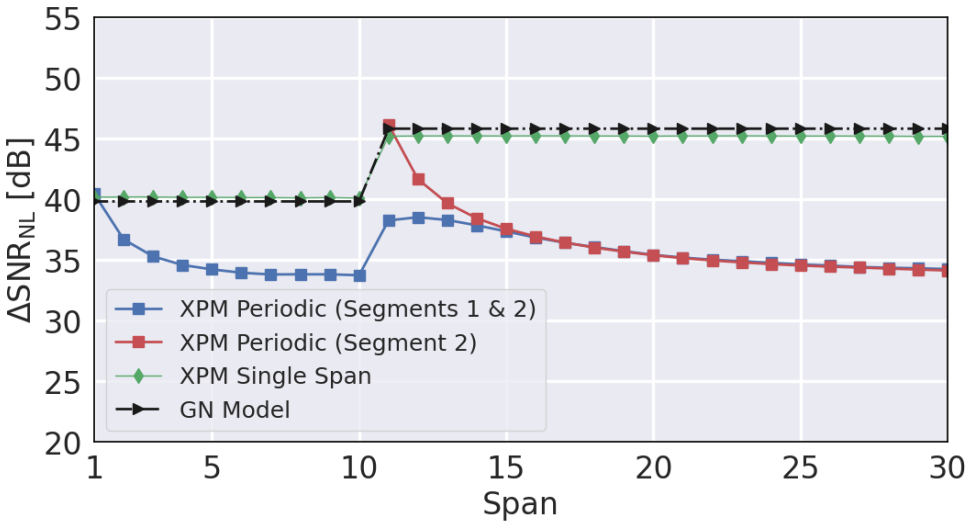

Fig. 4.32 The $\Delta\text{SNR}_{\text{NL}}$ versus span index for a single interfering pump, with $\Delta f = 300\,\text{GHz}$ and $R_s = 64\,\text{GBaud}$, through a dispersion-managed segment. Results are presented for the entire segment (blue lines), for the final 20 spans (red lines), each span evaluated independently (green lines) and a GN model implementation (black dashed lines), for $\alpha = 0.2\,\text{dB}/\text{km}$, $L_s = 80\,\text{km}$, $D_1 = 4\,\text{ps}/(\text{nm}\cdot\text{km})$, $D_2 = 16\,\text{ps}/(\text{nm}\cdot\text{km})$, and $D_{\text{RES}} = 160\,\text{ps}/\text{nm}$.

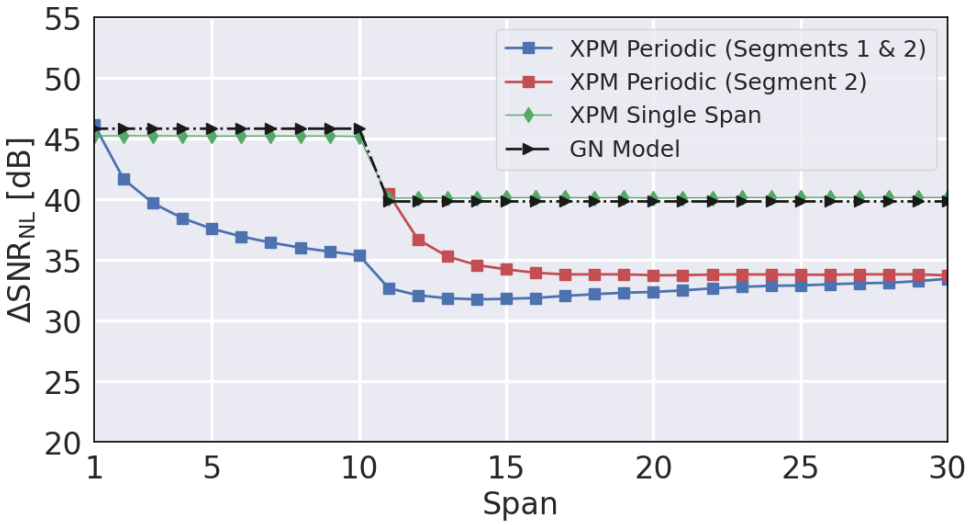

Fig. 4.33 The $\Delta\text{SNR}_{\text{NL}}$ versus span index for a single interfering pump, with $\Delta f = 300\,\text{GHz}$ and $R_s = 64\,\text{GBaud}$, through a dispersion-managed segment. Results are presented for the entire segment (blue lines), for the final 20 spans (red lines), each span evaluated independently (green lines) and a GN model implementation (black dashed lines), for $\alpha = 0.2\,\text{dB}/\text{km}$, $L_s = 80\,\text{km}$, $D_1 = 16\,\text{ps}/(\text{nm}\cdot\text{km})$, $D_2 = 4\,\text{ps}/(\text{nm}\cdot\text{km})$, and $D_{\text{RES}} = 160\,\text{ps}/\text{nm}$.

4.4.3 Dispersive Coherency Factor

Combining all information that has been observed within Figs. 4.20 – 4.33, it is visible that the asymptotic level attained by the XPM accumulation depends upon the parameters of OLS1, rather than both OLS1 and OLS2. Although jumps due to changes in OLS configuration are still present, this suggests that the residual dispersion introduced within the first couple of fiber spans is what dictates the evolution of the XPM impairment throughout an entire dispersion-managed segment. Additionally, the slow trend of the accumulation towards this asymptotic level is suggestive of a memory effect, whereby the NLI generated in previously crossed fiber spans affects the NLI generation in future fiber spans. Normally, the XPM accumulates completely incoherently, which means that any incoherent model applied to a scenario where a coherent signal is transmitted through a dispersion-managed link will likely provide inaccurate estimations. Being able to quantify and correct for this behaviour is therefore of interest for the scenario where this may occur within a disaggregated network segment.

It is possible to characterise this behaviour using a parameter, C_{ij}, denoted the coherent coupling factor. This parameter quantifies the correlation between two spans, i and j, providing the amount of additional XPM that is generated between them. This approach has previously been used in [182], following a similar but more expansive methodology as [8], where a parameter is used to quantify the incremental differences in accumulation in terms of intrinsic fiber span parameters. In this section a similar methodology is applied, in order to characterise the macroscopic behaviour of the XPM accumulation memory effect that occurs due to residual dispersion. The XPM power gradient for a given fiber span, $\Delta P_{\mathrm{XPM,i}}$, may be written in terms of C_{ij} as:

$$\Delta P_{\mathrm{XPM,i}} = \sigma_i^2 + 2\sum_{j=1}^{i-1} C_{ij}\sigma_i\sigma_j \,, \tag{4.6}$$

where the variable σ_i corresponds to the XPM power that is generated at the ith fiber span, not counting any additional coherent impairments induced by residual dispersion, meaning that this quantity corresponds to the green lines in Figs. 4.20 – 4.33. The additional coherent impairments are therefore accounted for by the sum on the right hand side of this equation, providing a contribution when a low level of accumulated dispersion is present between two neighboring spans. The presence of this dispersion causes the XPM contributions between these two spans to sum coherently

at the RX after chromatic dispersion compensation is performed, preventing them from being considered as completely uncorrelated.

Similar to the result concerning the SPM in [182], it has been observed in Figs. 4.20 – 4.33 that the memory effect decreases as more chromatic dispersion is accumulated between the correlated spans. To provide a more explicit example of this effect, one may consider the XPM generated at the 3rd fiber span. The XPM has an inherent contribution, given by σ_3^2, but also has contributors due to the correlation that arises from the 1st and 2nd fiber spans:

$$\Delta P_{\mathrm{XPM},1} = \sigma_1^2 \,, \tag{4.7}$$

$$\Delta P_{\mathrm{XPM},2} = \sigma_2^2 + C_{21}\sigma_2\sigma_1 \,, \tag{4.8}$$

$$\Delta P_{\mathrm{XPM},3} = \sigma_3^2 + C_{31}\sigma_3\sigma_1 + C_{32}\sigma_3\sigma_2 \,, \tag{4.9}$$

which consequently means that the coupling between all previously crossed fiber spans must be calculated in order to obtain the total memory effect of a given span.

To validate this approach, the total cumulative C_{ij} value was calculated for every simulation case described within Sec. 4.4.2. In order to only observe the fundamental behaviour of the memory-inducing effect, the XPM values of the periodic case were considered with OLS2 as the origin point of the signal, corresponding to the blue curve in Figs. 4.20 – 4.33. This starting point was chosen to exclude any changes in gradient that occur when passing from OLS1 to OLS2, which, as outlined in Sec. 4.2, arises due to the change in maximum NLI generation for a given fiber span configuration. In any case, the first 10 spans of OLS1 correspond exactly to the first 10 spans of OLS2, except with swapped D_1 and D_2 values. This means that evaluating C_{ij} values for OLS2 quantifies the behavior of the XPM accumulation for all investigated cases.

To better account for the fiber and spectral parameters of the network segment, a variable is defined, denoted θ_{span}, which quantifies the amount of residual dispersion introduced at each fiber span. This parameter, when considering a fiber span of index k, is given by [182]:

$$\theta_{\mathrm{span}}(i,j) = R_s^2\pi \left| \sum_{k=j}^{i-1} \left(\beta_{2,k}L_s + \beta_{\mathrm{RES},k}\right) \right| \,, \tag{4.10}$$

where $\beta_{2,k}$ is the dispersion coefficient of the kth fiber span, and β_{DCU} is the dispersion introduced by the DCU, expressed in terms of frequency. This parameter may then be normalized with respect to another variable, θ_{eff}, or effective theta, that quantifies all system parameters which the incoherent XPM accumulation scales with:

$$\theta_{\mathrm{eff}} = \pi R_s^2 \beta_2 L_{\mathrm{eff}} \,. \tag{4.11}$$

To find the total C_{ij} values, Eq. 4.6 was used to calculate the correlation between each span and the preceding one, for each scenario under investigation. Focusing upon the core scenarios where $R_s = 32\,\mathrm{GBaud}$, $\alpha = 0.2\,\mathrm{dB/km}$, and $L_s = 80\,\mathrm{km}$, the C_{ij} values for every investigated configuration are plotted (in linear units) against $\theta^2_{\mathrm{span}}(i,j)\,/\,\theta_{\mathrm{eff}}$, for all three considered D values in Figs. 4.34 and 4.35, showing the results for $\Delta f = 150$ and 300 GHz, respectively. To more closely inspect the behaviour of the densely populated region about the origin, a zoomed-in look at these regions within Figs. 4.34 and 4.35 are shown in 4.36 and 4.37, respectively.

Firstly, it is visible in these figures that the behaviour for all three D_{RES} cases follows the same curve, albeit with a small difference in gradient. This implies that the correlation between two given spans i and j decreases with an inverse proportionality to D_{RES}, identically to the observed behaviors within Figs. 4.20 –

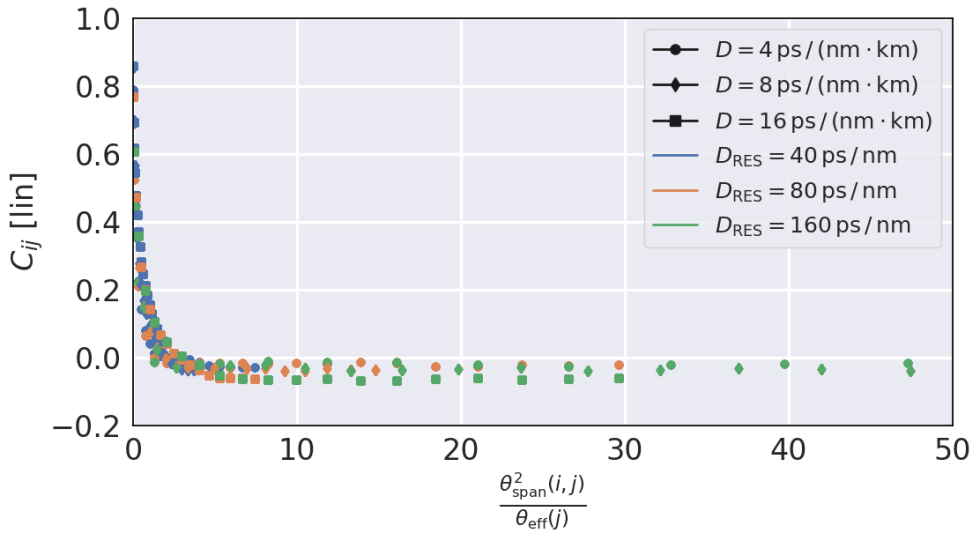

Fig. 4.34 The plot of the correlation factor, C_{ij}, against $\theta^2_{\mathrm{span}}\theta_{\mathrm{eff}}$, which quantifies the behavior of the XPM accumulation depending upon the scaled fiber parameters, for $\Delta f = 150\,\mathrm{GHz}$. Three different residual dispersion values are shown; $D_{\mathrm{RES}} = 40$, 80 and 160 ps / nm are given by the blue, orange and green dots, respectively.

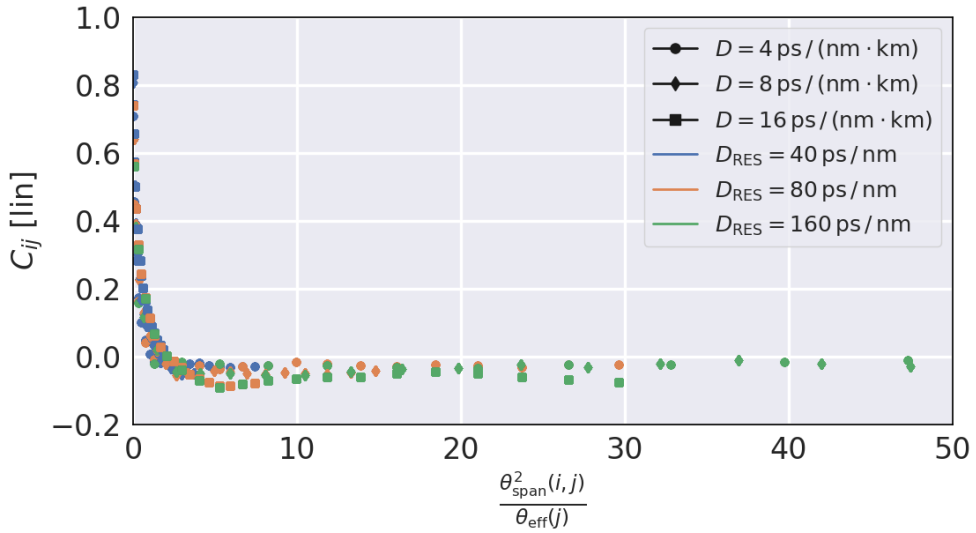

Fig. 4.35 The plot of the correlation factor, C_{ij}, against $\theta^2_{\text{span}}\theta_{\text{eff}}$, which quantifies the behavior of the XPM accumulation depending upon the scaled fiber parameters, for $\Delta f = 300\,\text{GHz}$. Three different residual dispersion values are shown; $D_{\text{RES}} = 40$, 80 and $160\,\text{ps}/\text{nm}$ are given by the blue, orange and green dots, respectively.

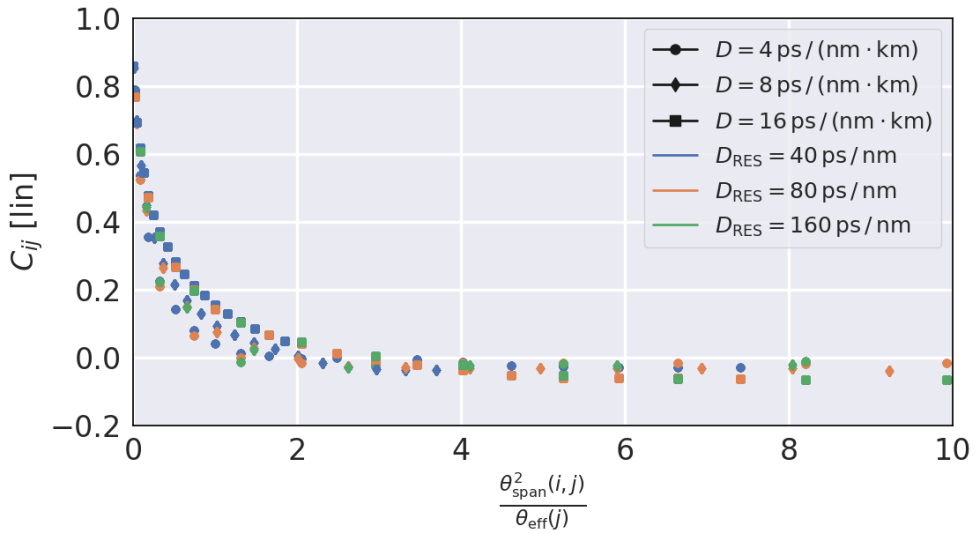

Fig. 4.36 A closer view of the dense region of interest centered about the origin within Fig. 4.34.

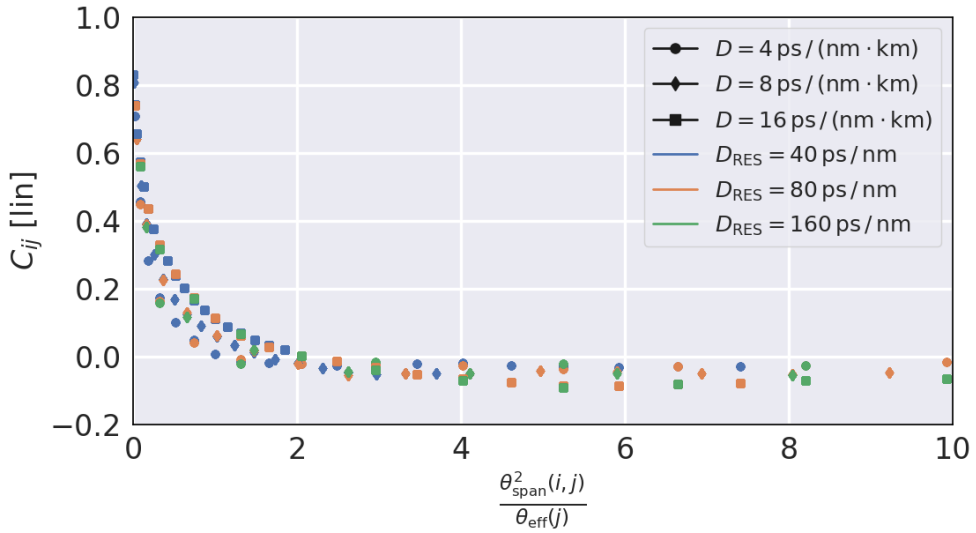

Fig. 4.37 A closer view of the dense region of interest centered about the origin within Fig. 4.35.

4.33. It can also be seen that that C_{ij} decreases proportionally to $\theta^2_{\text{span}}(i,j)\,/\,\theta_{\text{eff}}$. Importantly, all C_{ij} values are below zero after a given $\theta^2_{\text{span}}(i,j)\,/\,\theta_{\text{eff}}$ value, which means that the coherency induced by the residual dispersion will always decay to zero, no matter the D_{RES} present within the system. Subsequently, given a long enough distance, the XPM will accumulate towards the asymptotic value defined by the parameters of the fibers within OLS1, with this happening faster for higher D_{RES} values. Changing Δf is also observed to provide only small differences to the distributions of the data, without any major alterations to the overall behavior. This implies that, for each pump-and-probe pair, there exists a function which characterizes the relationship between the coherent effect induced by the residual dispersion and the system parameters, enabling this approach to be applied to any CUT and interfering channel pair within a disaggregated network framework. Furthermore, the behavior of the XPM accumulation in this scenario bears significant similarity to the behavior of the SPM accumulation [8, 182], suggesting that these parameters provide an intrinsic characterization of coherent NLI contributions, for both SPM and XPM, in both uncompensated and dispersion-managed scenarios.

4.5 Chapter Summary

Within this chapter an overview of NLI generation within disaggregated network segments has been presented, with findings observed that may be used to compensate for effects which are not present within typical aggregated network architectures. A major difference when working within a disaggregated architecture is that signals passing through disaggregated network segments have origin points which may be outside of the network segment, meaning that their history may be partially or fully unknown. Additionally, disaggregated network segments are not guaranteed to have uniform OLS configurations, meaning that the effects of changing fiber configuration throughout a given OLS must be considered. Both of these details were investigated by first applying varying amounts of Gaussian predistortion to a signal before propagation through a uniform, 40-span long OLS. Next, a single span in isolation was investigated, varying the length of the fiber span.

Two key observations were made: firstly, the maximum amount of NLI which may be generated between two fiber spans is completely bounded by the result of the GN model. Secondly, when considering the difference in NLI generation between two fiber spans, increasing length of these spans correspondingly increases the maximum amount of NLI which may be generated, with this level progressively increasing up to a maximum, which also corresponds to the GN model. This means that if a signal originates from outside of the network segment and has a known history, is it possible to apply Gaussian predistortion to distort the signal such that it begins propagation with the appropriate level of Gaussianisation. Otherwise, if the signal history is unknown, the level given by the GN model may be used as a conservative upper bound, and adjusted appropriately to provide further accuracy according to known information about the fiber effective lengths within the network segment.

Following this, the impact of changing fiber dispersion within a network segment was investigated, comparing the generation of the SPM and XPM impairments with the total NLI, each from corresponding simulation configurations. Jumps in ΔSNR_{NL} were observed when D was changed, which caused no issues when modelling the XPM, but required that the asymptotic coherent accumulation coefficient, C_∞, is included within the SPM model to ensure accurate and conservative predictions. With this correction, a superposition of the SPM and XPM effects was performed, providing a result which closely matched the total NLI, demonstrating that spectral

and spatial separability is possible within a disaggregated network segment, even for non-uniform links.

Attention then turned to the behaviour of the XPM within dispersion-managed links, where DCUs produce small amounts of residual dispersion. A consistent and uniform behaviour has been observed, where the difference between the disaggregated GN model and the periodic accumulation is proportional to the residual dispersion induced by the DCUs, with significant variations being present for D_{RES} values at or below 160 ps / nm. The macroscopic behaviour of this discrepancy has then been characterised by calculating a coupling factor, C_{ij}, that was found to scale proportional to $\theta^2_{\mathrm{span}}(i,j) \,/\, \theta_{\mathrm{eff}}$, a relation which takes into account the residual dispersion and the signal and fiber parameters. Subsequently, in a dispersion-managed system, it is possible to calculate the discrepancy between the disaggregated GN model and the periodic transmission value by combining information about the history of the signal and the residual dispersion present within the system, which may then be integrated into the disaggregated model. Due to C_{ij} following a well-defined curve, this methodology is possible for a wide range of realistic system parameter settings, and may be performed separately for each interfering pump, as required, further integrating the effects due to signal Gaussianisation mentioned previously.

To summarise, modelling NLI within disaggregated network segments from a fully spectrally and spatially disaggregated perspective is therefore possible, with the GN model always serving as an upper bound for the XPM generation, and the maximum amount of SPM able to be estimated by calculating the asymptotic level of its accumulation. Adjustments on a per-channel basis may then be performed, to account for unknown signal histories or in-line dispersion compensation, in order to increase accuracy, if required.

Chapter 5

Modelling LSCE-Band Experimental Transmission

Following the investigation of NLI impairments within disaggregated networks, and the validation of the disaggregated part of the disaggregated and wideband model, attention now turns to the wideband part of this model. As mentioned within Chapters 1 and 2, enlarging transmission bandwidths beyond the C-band presents issues for NLI modelling which must be taken into account to retain model accuracy. Within this chapter, the wideband and disaggregated model is validated against an experimental campaign that has been performed at Aston University, where propagation of a fully loaded L-, C-, S-, E-band spectrum was performed over a single 70 km long fiber span, and then amplified with a mixed BDFA and Raman amplifier regime. To find the optimal QoT for a wideband transmission scenario, the intricacies of power optimisation, management of impairments which arise from novel amplification techniques, and the interaction between the linear, nonlinear and power-transferring propagation effects must all be considered carefully, with the behaviour of the physical layer impairments first outlined within the following section.

5.1 Wideband Transmission Parameters

Considering the linear contributors to the QoT degradation, in a standard C-band transmission scenario the fiber attenuation α, is typically presented as a constant

value that has been measured for a given λ, which usually corresponds to the center of the WDM comb under investigation. The variation of α across the C-band is typically small, assuming this value to be constant produces a loss of accuracy that is tolerable for most operating scenarios. When moving to even the simplest wideband propagation scenario (a C+L-band implementation), the variation of α between the C- and L-bands is large enough that taking this value as a constant is no longer feasible. As a result, use of a frequency- and length-dependent gain/loss profile, $\rho(z, f)$, is required to avoid large model inaccuracies.

Concerning the chromatic dispersion of the fiber spans, within C-band transmission scenarios it is sufficient to use a single value of β_2 for each fiber span, and much like α, taking this variable to be constant across the entire band provides a loss in accuracy which is relatively small with respect to the size of the linear and nonlinear impairments. For wideband transmission, it is no longer sufficient to use solely β_2; this value is provided for a given reference frequency, meaning that as the spectral separation between the interfering channel and the reference frequency increases, so too does the discrepancy between the β_2 values at the local and reference frequencies. A solution is to make use of β_3, as given within Eq. 2.9, which corresponds to the gradient of β_2. This provides a smooth function that is then used for calculation of the chromatic dispersion for a given frequency, with β_4 potentially also being included, if the accuracy of this estimation is not sufficient. Alternatively, a spectral sweep may be performed to measure β_2 for a range of frequencies, with an interpolation based upon Eq. 2.10 used to provide a smooth function for any unmeasured frequencies, as performed within [5].

Moving attention to the nonlinear impairments, γ is also frequency-dependent, but as seen in Fig. 2.5, it has a small variation with respect to α and β, changing from 1.15 to 1.45 $\mathrm{W^{-1}km^{-1}}$ between the L- and E-bands, and scales approximately linearly. As the XPM contributions of the interfering pumps decrease proportionally to their spectral distance from the probe, the difference in γ does not cause a significant issue, as pumps with a significantly different γ value from the probe will not generate significant amounts of XPM. The practical result is that changes in γ are only relevant within an ≈ 3 THz region surrounding any given CUT, to be maximally conservative. Subsequently, for a given CUT, γ may be kept the same for all interfering channels, without any significant loss of accuracy.

In terms of the nonlinear effects themselves, the situation becomes far more complex than that of a standard C-band scenario. As seen from Fig. 2.6, the Raman gain profile starts to become relevant at spectral separations of approximately 5 THz, and peaks between 10 and 15 THz, for a typical SMF fiber. For an example wideband transmission scenario that is transmitting a DWDM spectra with full spectral load over the L-, C-, and S-bands, the total spectral occupation is 18 THz, or more, meaning that significant power transfer arising from the SRS effect will take place most efficiently from channels in the S-band to the C- and L- bands. The main problem which arises from this power transfer is that, for a given CUT, the leading contributor (the XPM) scales proportionally to $P_{CUT}P_{\text{ch}}^2$, as shown in Eq. 2.17. As a result, power transfer from the SRS effect significantly affects the NLI generation, with channels at higher frequencies generating less NLI due to power depletion, and channels at lower frequencies generating a larger amount of NLI due to power accretion. Furthermore, this power transfer continues if additional channels are present at lower frequencies, meaning that broad spectra will experience a cascade effect; in the same L-, C-, S-band example, channels within the C-band will both receive power from the S-band and transfer power to the L-band. Combining the effect of SRS power transfer and the subsequently altered NLI noise magnitude with the frequency-dependent α, β, and γ creates in a scenario where the total QoT impairment after transmission is not simple to predict, and may vary greatly in unpredictable ways even for small changes in input power.

5.2 Power Optimization

The result of the interplay between these frequency-dependent interactions is that channel input power optimisation is a complex problem within wideband transmission. Network controllers typically seek GSNR values which are both flat and maximal, with the aim to reduce complexity when choosing modulation formats and assigning new LPs, and to maximise capacity [159, 183, 184]. When seeking an optimal input power, minimising GSNR standard deviation and maximising absolute value at the RX side are therefore commonly chosen figures of merit [185–187].

The problem of whether the output GSNR for an arbitrary wideband spectral configuration may be maximised while retaining some degree of flatness has not yet been formally solved, as this also depends greatly upon the amplifier configuration

of the system in question. As mentioned in Sec. 1.4, EDFAs are only able to cover the C- and L-bands with reasonably low NFs, meaning that alternative amplification strategies are therefore required for other wideband regions. The use of new amplification strategies, such as TDFAs in the S-band, BDFAs in the E-band, and hybrid Raman-EDFA/BDFA amplification methods all come with distinct losses, which further must be taken into account when finding the optimal power profile. For example, considering a L-, C-, S- transmission scenario, with amplification performed with EDFAs in the L- and C-bands, and a prototype TDFA within the S-band. This TDFA may not guarantee a flat gain profile, on account of device immaturity, which may prevent a flat GSNR from being recoverable at the RX for a given capacity requirement.

Evidently, there are many variables which come into play regarding input power optimisation within a wideband transmission scenario, and a variety of techniques for finding the optimal input power have been proposed. Evolutionary algorithms may be used to intelligently search the problem space – these algorithms perform well for problems with a large number of variables, and tend to converge to a near-optimal value within acceptable timeframes. Some notable examples include genetic algorithms [188, 185, 189], simulated annealing [190] and particle swarm algorithms [191], all of which providing a solution which significantly improves GSNR flatness and maximal value at the transmission output, compared to a flat input power profile. Machine learning implementations are also increasing in popularity, as they typically provide a greater level of adaptability than evolutionary algorithms, at the expense of computational and implementation complexity [192, 188].

5.3 Abstraction of Experimental Set-up

Now that the groundwork has been laid out for modelling transmission impairments within a wideband transmission scenario, attention now moves to modelling the aforementioned experimental transmission. This experiment, performed at Aston University, was done separately and prior to the modelling work explained within this thesis. Within this experiment, a total of 26 CUTs were transmitted as part of a DWDM spectra that spans a total of 25.8 THz, covering the entirety of the L-, C-, S-bands, and a portion of the E-band. A total of 147 channels are located within the L-, C-, and S-bands, with interfering channels created by shaping ASE noise in

emulation of a transmitting channel. For the E-band, rather than a DWDM region, only a maximum of three channels are transmitted at one time, emulated by laser diodes, which is due to a lack of mature components within the E-band.

A diagram abstracting the experimental set-up is shown in Fig. 5.1: the L-, C-, S-, E-band spectrum is transmitted simultaneously through the line system, with each band in the experiment having a constant, flat power, P_{L}, P_{C}, P_{S}, and P_{E}, respectively. Although not shown to scale, Fig. 5.1 shows the approximate spectral occupation of each band and the guard bands between them, with 41, 46, and 60 channels present within L-, C-, and S-bands, respectively, and the E-band shown as if it were fully occupied. This spectrum passes through a single 70 km long fiber span of SMF, then entering the hybrid amplifier system, where the E-band is separated from the rest of the spectrum and amplified with a BDFA, and the L-, C-, S-bands are amplified with a two-stage Raman amplifier.

Concerning the BDFA, this device was developed by the collaborators at Aston University, providing a high level of gain at a low NF, and has been extensively tested and characterised in previous dedicated works [75, 193]. As for the Raman amplifier, each stage consists of 7.5 km of inverse dispersion fiber (IDF), serving to first amplify the S-band, followed by the L- and C-bands. The first stage has three Raman pumps within the E-band, whereas the second stage has five Raman pumps that are located within the S-band. All Raman pumps used within this experimental set-up are counter-propagating, and the IDF type is used on account of the large Raman gain that it experiences, rather than its dispersive qualities. The exact spectral location and powers for each of the pumps used within the Raman amplifier are listed in Tab. 5.1.

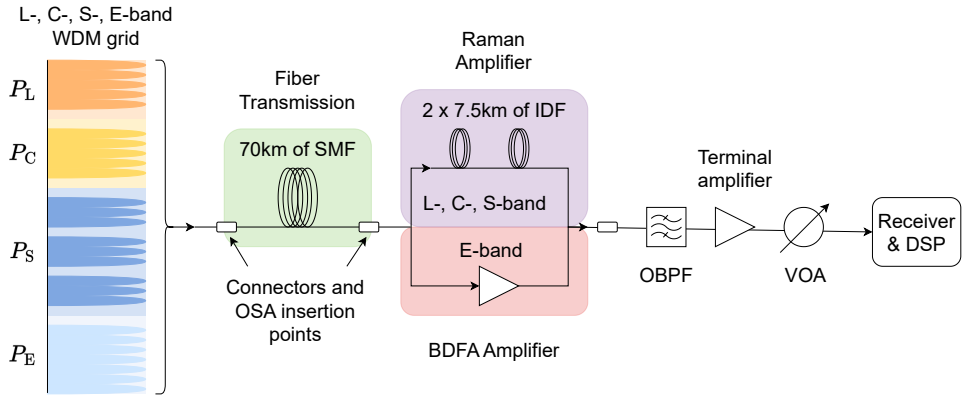

Fig. 5.1 An abstraction of the experimental set-up used for L-, C-, S-, E-band transmission.

Table 5.1 The wavelengths and powers for each of the pumps used within the experimental Raman amplifier.

Amplified Band	Wavelength (nm)	Frequency (THz)	Pump power (mW)
S-band	1365	219.53	485
S-band	1385	216.49	333
S-band	1405	213.52	116
C+L-band	1425	210.63	205
C+L-band	1445	207.80	215
C+L-band	1465	205.04	190
C+L-band	1485	202.34	47
C+L-band	1508	199.68	122

To help prevent QoT impairments that arise due to interactions between the Raman pumps and propagating channels within the S-band, this band has been split into three sub-bands, denoted S_1, S_2, and S_3, ordered from lower to higher frequency, respectively. Each of these sub-bands are separated by a guard band region where no channels are present, which may also be seen in the abstraction given in Fig. 5.1.

After amplification, the signal is recombined, then passing through a sequence of devices: an optical bandpass filter (OBPF), a terminal amplifier, a VOA, and then finishing transmission by passing into a RX that makes use of a coherent DSP module. As highlighted within Fig. 5.1, there exist three connection points within the line where an optical spectrum analyzer (OSA) may be used to measure the spectrum. It should be noted that these connectors induce linear losses that apply to the entire spectrum outside of the OSNR, which originate from imperfect splices. The connectors that are present on the RX-side are not shown, but data concerning their characterisation was available for use within the model.

5.4 Experimental Parameter Characterisation

The QoT impairment of this experiment is calculated by comparing the experimental GSNR at the end of the coherent DSP block to a simulated GSNR, comprised of properly modelled OSNR and SNR_{NL} contributors. For the L-, C-, and S-bands, the physical processes in the Raman amplifier must be considered carefully, as this method introduces additional nonlinear impairments [194, 195].

As a first step, the SMF and IDF parameters must be described to calculate the SNR_{NL}, followed by creation of the hybrid amplification model to calculate the OSNR. These parameters are obtained through a combination of data measured during the experimental campaign, and data sheets provided by the fiber suppliers. As described in Sec. 5.1, the main parameters that must be taken into account are α, β_2, and γ, along with the Raman gain coefficient, g_0, which includes the effect of the Raman amplifiers. By combining all of these effects, a power profile, $\rho(z,f)$, is created, giving the power evolution of the entire spectrum as it propagates through the system. Starting with α, values for the spectrum under consideration were measured experimentally using a cut-back technique, presented in Fig. 5.2, with the blue and red lines corresponding to the SMF and IDF fiber types, respectively. Similarly for β_2, values for the SMF and IDF fibers are measured for the required L-, C-, S-, E-band spectral range, presented in Fig. 5.3. For γ, the parameters A_{eff} and n_2 in Eq. 2.11 must be found for each fiber type, with the former calculated using the theory of weakly guiding fibers with standard SMF parameters [104], and the latter taken from the fiber data sheets. The calculated γ values for each fiber type is given in Fig. 5.4. Similarly, g_0 has also been measured experimentally, for both fiber types, with this value at a reference frequency of $f_{\text{ref}} = 203.9$ THz presented in Fig. 5.5.

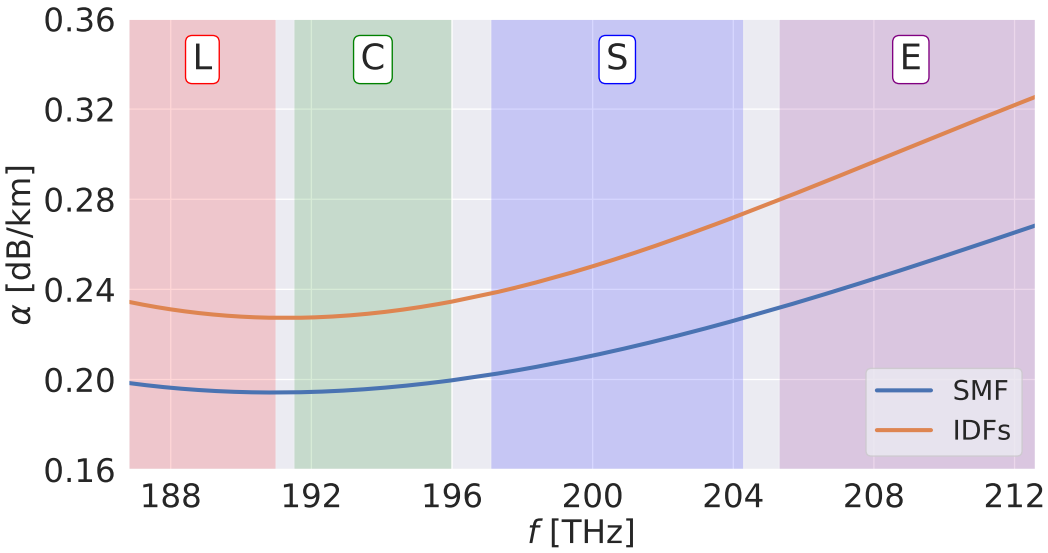

Fig. 5.2 The loss coefficients, α, of the SMF and IDF types for the wideband spectral region under consideration.

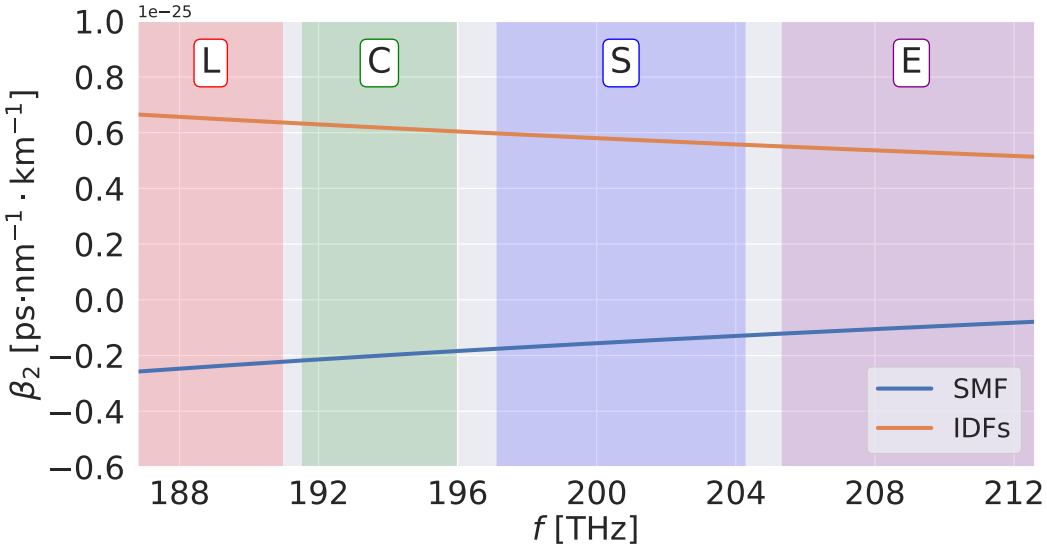

Fig. 5.3 The group velocity dispersion, β_2, of the SMF and IDF types for the wideband spectral region under consideration.

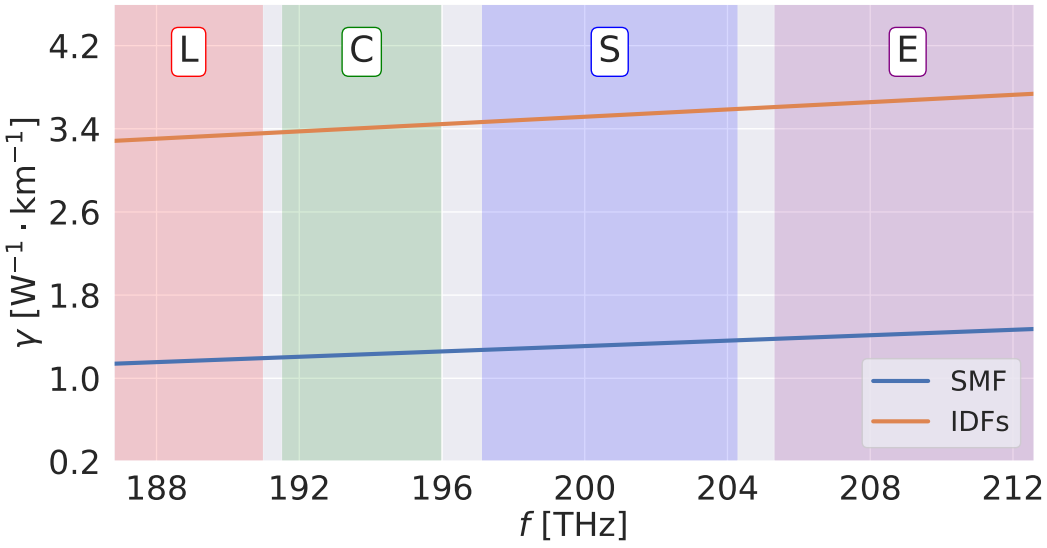

Fig. 5.4 The nonlinear coefficient, γ of the SMF and IDF types for the wideband spectral region under consideration.

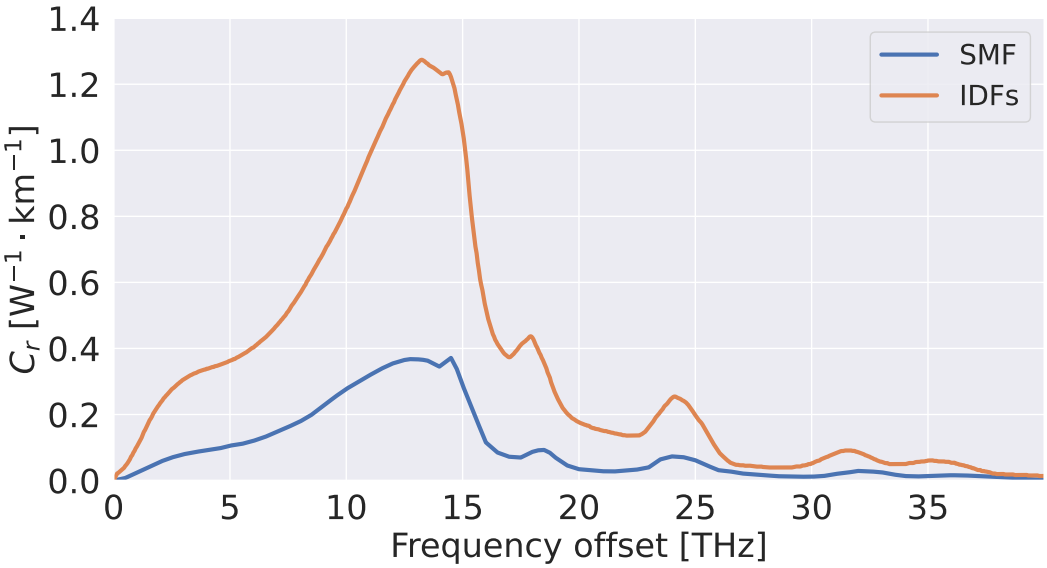

Fig. 5.5 The reference Raman gain coefficient, g_0, corresponding to the Raman gain at a reference frequency, $f_{\text{ref}} = 203.9$ THz, for the SMF and IDF types for the wideband spectral region under consideration.

Moving onto the amplifier model, the effects of the Raman pumps are included by solving the Raman equations [132], which is performed using the `RamanSolver` module within the GNPy library [114]. Solving these equations provides the power profile through both IDF fibers, along with the ASE noise contributions, with the latter providing the OSNR of the L-, C-, S-band regions. For the E-band, the BDFA is modelled using a simpler approach resembling that of a standard EDFA, where the signal is amplified using the experimentally-derived gain and NF profiles, and the ASE is calculated using Eq. 2.24. All parameters required for the Raman equations and Eq. 2.24 have been obtained from experimental characterization of the amplifier system: f_c has been obtained by analysing the spectrum, ζ and G have been measured for all wavelengths under investigation, for a variety of input powers, and R_s is a constant 30 GBaud for all channels. The gain and NF for the entire spectrum is presented is Fig. 5.6; it is visible that the E-band presents the highest and most uniform gain on account of the good performance of the BDFA, whereas ripples are present within the gain of the L-, C-, and S-bands due to the two-stage Raman amplification process.

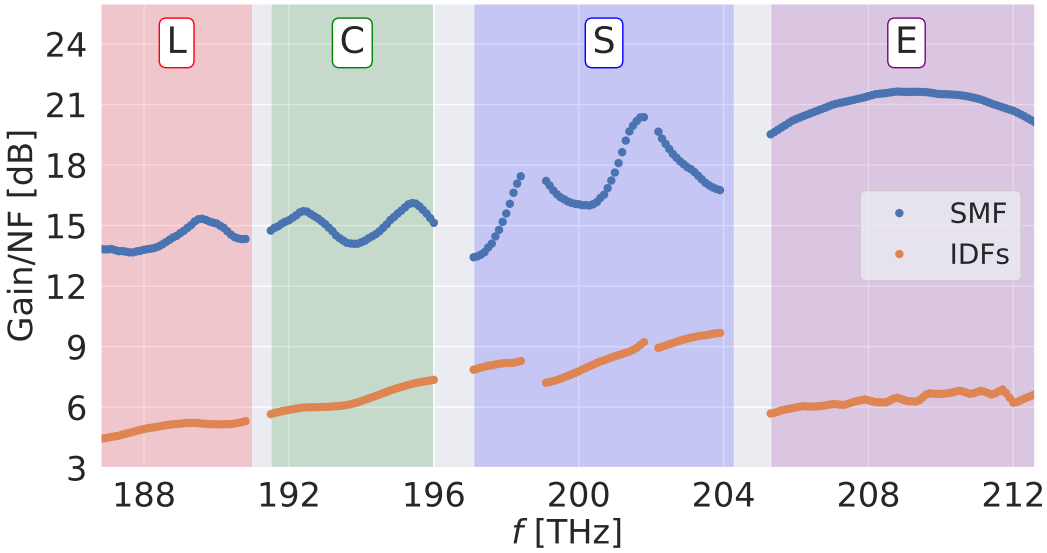

Fig. 5.6 The gain and NF profiles calculated with the hybrid amplifier model, across the wideband spectral region under consideration.

5.5 Simulation Set-up

The S- and E-band spectral regions are not well characterised from a NLI modelling perspective, particularly for full-spectrum transmission that also includes the L- and C-bands with a hybrid amplification strategy. To therefore ensure the highest possible accuracy of this model in unexplored territory, the decision was made to use the SSFM library outlined in Chapter 3 to estimate the $\mathrm{SNR}_{\mathrm{NL}}$ of this experiment. This decision was made in order to minimise any doubts about whether resultant differences between the experimental and simulated results are from assumptions made as part of the model.

In the experimental campaign the L-, C-, S-bands were fully populated with channels, whereas only three channels were present in the E-band at a time, causing this latter band to produce a comparatively small impairment. To provide a meaningful characterization of the E-band, a fully loaded E-band spectra was considered for the wideband model, producing a spectrum with 41, 46, 60, and 74 channels in the L-, C-, S-, E-bands, respectively, giving a total of 221 channels ranging from 186.8 to 212.6 THz over a total bandwidth of 25.8 THz, including guard bands at the same positions as those used within the experimental setup. As a result, the aim of

this model is to provide an estimate of anticipated losses over the entire L-, C-, S-, E-band spectrum for an envisaged full spectral load implementation.

If an idealised transmission scenario is to be considered, the question then turns to how the channel powers should be set, as in the experimental setup a flat power of approximately -2 dBm per channel was used for all bands, which is almost certainly non-optimal following the discussion of Sec. 5.4. For the model the decision has been made to choose a middle ground between a flat input power approach and a more complex approach, such as an evolutionary algorithm. Instead, the LOGO power is calculated for each band, such that every channel in a given band is set to a flat and locally optimal power. This provides a spectrum which has a more optimal input power spectrum than that of a uniformly flat scenario, yet still gives comparable results to those measured within the experiment. The logo power for each band was found to be -1.2, -1.6, -1.3, and -1.0 dBm per channel, for the L-, C-, S-, and E-bands, respectively. The highest power is for the E-band, showing that a greater input power is required due to the fiber parameter characteristics, such as high α values in this spectral region.

Concerning the line description, the experimental setup shown in Fig. 5.1 is closely replicated, with two distinct transmission stages. First, the entire spectrum passes through a 70 km fiber span, which corresponds to the propagation part of the experiment. The signal is then split into its L-, C-, S-band and E-band constituent spectral regions, with the former passed through two 7.5 km fiber spans covering the L-, C-, S-bands to perform the Raman pump amplification, and the latter amplified separately solely using the GNPy library amplifier model.

For the spectral parameters a variety of CUTs have been selected for each band: 5 each in the L- and C- bands, 9 in the S-band, and 7 in the E-band, for a total of 26. These CUTs were placed such that one CUT was always present at the center of each band (where the NLI is anticipated to be the largest), and at the edges of each band (where inter-band contributions may be present), with the remaining CUTs being equally spaced within the rest of the spectrum, to ensure that the NLI of each band is well sampled. As a result, the choice of 9 CUTs arises from the S-band being separated into three regions to accommodate the Raman pumps, and with 7 present in the E-band due to its wide spectrum. The CUTs used for the simulation campaign differ from the ones used within the experiment, which were spaced more regularly and not always near the band edges. It is however possible to perform an

interpolation of the calculated SNR_{NL} on a per-band or sub-band basis, providing an estimation of the NLI at any required frequency, with a small amount of related uncertainty.

All channels have been transmitted with 16-QAM modulation formats, $R_s =$ 30 GBaud, channel bandwidths of 100 GHz, and channel roll-off values of 0.05, corresponding exactly to the configurations used for all channels within the experimental set-up. To permit simulation of the entire L-, C-, S-, E-band spectrum, it is necessary to use a configuration that does not propagate the full spectrum at once in order to reduce computational costs to feasible levels. Consequently, the limited-bandwidth SSFM configuration explained in Sec. 3.3.4 is used, with a 3 THz window centered around each CUT.

5.6 Results and Discussion

As a first step, the power profile at the inputs of the SMF, first IDF, second IDF, and the output of the second IDF is shown in Fig. 5.7. Starting with the input power spectrum, given by the blue dots, it is visible that each band has a different flat power that corresponds to its LOGO value. The signal then passes through the SMF fiber, producing a power profile given by the orange dots. Here, the impact of the fiber parameters is visible: as the frequency increases, a corresponding reduction in power is observed, which originates from the attenuation profile given in Fig. 5.2. Additionally, gaps within the S-band are present, which correspond to the guard bands where the Raman pumps are present within the second IDF, separating the S-band into the S_1, S_2, and S_3 sub-bands.

Next, the signal propagates through the first IDF, given by the green dots. During this transmission, the S-band is amplified, with small amounts of residual amplification also present within the L- and C-bands. This S-band amplification is uneven, arising due to the location and powers of the Raman pumps, but this behaviour is not undesirable, as during transmission through the second IDF, power will also be transferred from the S-band to the L- and C-bands as a result of SRS effects, creating a more even gain profile. When the spectrum propagates through the second IDF, the Raman pumps located within the S-band amplify the L- and C-bands, producing the final power profile, given by the red dots. The final power profile of the E-band is also included within this final spectrum, following the amplification process performed

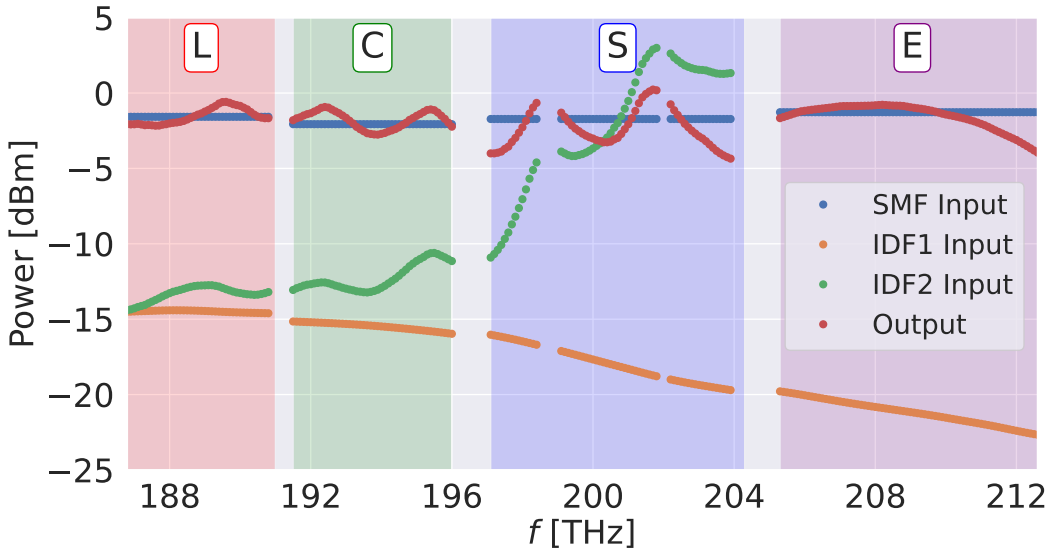

Fig. 5.7 The power profile, $\rho(z, f)$, of the propagated signal shown at the input of the line, and after each optical element.

within the GNPy library. Compared to the other bands, the BDFA provides the flattest power profile, which arises from the correspondingly flat gain and NF values for this device, visible in Fig. 5.6. It should be noted that this good performance is also partially due to this band being amplified separately, minimizing the effects of SRS power transfer to the other bands.

5.6.1 Simulated OSNR Results

The OSNR, and SNR_{NL} values for the entire fully loaded spectrum are provided in Fig. 5.8. Firstly, regarding the OSNR, this value has been calculated from the ASE noise that is generated during the propagation and amplification stages. To model the propagation stage, the initial contribution has been found by estimating the noise floor for each channel, which has been extracted from the input spectrum provided by the OSA placed at the first connection point in Fig. 5.1. To make the measured noise floor values better represent to the simulation scenario, for each band they have been re-scaled proportionally to the LOGO powers that have been used for the simulated transmission. To model the amplification stage, the GNPy Raman solver has been used to calculate the total ASE noise, for both the Raman pumping and BDFA amplification methods. It is visible that the OSNR is the highest

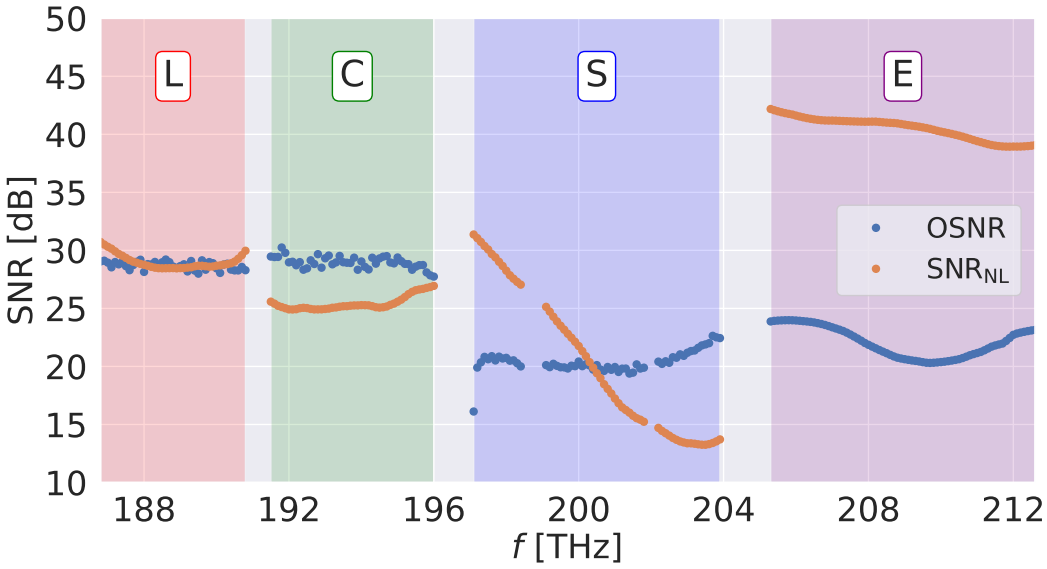

Fig. 5.8 The OSNR and SNR_{NL} values after propagation and amplification using the combined L-, C-, S-band Raman amplifier system and the E-band BDFA.

in the L- and C-bands, which is entirely a result of the channels within these bands having lower noise floors, therefore generating less ASE noise during propagation. The opposite reason explains the S-band having the lowest noise floor, whereas the OSNR in the E-band is dominated by the ASE noise that is generated during the BDFA amplification process.

5.6.2 Simulated NLI Results

Regarding the SNR_{NL}, for simplicity, this value has been calculated in the L-, C-, and S-bands, by summing the separate contributions from the SMF and IDF. Formally, this approach neglects to include any coherency which would occur as a result of phase noise correlation between the two stages, however, this contribution is likely to be insignificant, as propagation is only performed over a total distance of 85 km, and the incoherent XPM contribution is dominant at a symbol rate of 30 GBaud. For the E-band, the SNR_{NL} value is purely the NLI that is generated during transmission through the SMF, as the NLI generated during the BDFA amplification process is negligible. It should be noted that the SNR_{NL} values are presented as a curve by performing a quadratic interpolation between the SSFM results, for each CUT, within each band or sub-band.

In terms of the behaviour of the $\mathrm{SNR_{NL}}$ contributor, the E-band exhibits significantly better performance than all other bands, simply due to the NLI generated within the BDFA amplification being negligible. On the other hand, the worst and most uneven performance is observed within the S-band, and the reason for this behaviour can be explained by analysing the power profile evolution in Fig. 5.6. Considering that the XPM is the dominant contribution for any given CUT, the leading term of the NLI contribution therefore scales with respect to $P_{\mathrm{CUT}}P_{\mathrm{ch}}^2$, for all interfering channels. This means that a greater amount of power at a given channel generates a greater amount of NLI for all neighbouring channels. The NLI generated within the S-band is therefore large, primarily due to the Raman pump amplification being performed first in this band, which causes the S-band to enter the second IDF with a large amount of power. This is also evident by considering that the best performance within the S-band corresponds to the region with the lowest gain after transmission through the first IDF.

Better performance in the L- and C- bands is seen for precisely the opposite reason: as the Raman pump amplification of these bands is performed last, the majority of their propagation is performed at relatively low powers, meaning that the NLI generation is minimal. Furthermore, it is also evident that the C-band suffers from the ripples of the S-band amplification performed within the first IDF, whereas the L-band being affected the least causes it to have the overall best performance.

5.6.3 Comparing GSNRs

As described in Eq. 2.20, the GSNR may be found by taking the inverse sums of the OSNR and $\mathrm{SNR_{NL}}$ contributors. To properly compare the experimentally-measured GSNR value with the simulated GSNR, it is necessary to include the impairments which are present within the system due to RX limitations. To create a final figure of merit, a total GSNR which includes these impairments, denoted $\mathrm{GSNR_{TOT}}$, may be found from:

$$\mathrm{GSNR_{TOT}} = \left(\mathrm{GSNR_{SIM}^{-1}} + \mathrm{GSNR_{SYS}^{-1}}\right)^{-1}, \tag{5.1}$$

where $\mathrm{GSNR_{SIM}}$ corresponds to the simulated GSNR, and $\mathrm{GSNR_{SYS}}$ is the system GSNR, which gives the measured RX impairment for each CUT. A characterisation of the RX impairment after transmission through the 70 km SMF fiber span has

been provided from the experimental data, providing a $GSNR_{SYS}$ value for every experimental CUT location.

In addition to including the system impairments, the losses due to connectors and RX-side devices should also be included within the final figure of merit. The measured loss induced by these elements has been incorporated into the power profile evolution as a flat reduction of 0.7 dB between the TX and the SMF, 0.7 dB between the SMF and first IDF, and 1.4 dB between the output of the second IDF and the RX, giving a total reduction of 2.8 dB overall.

A comparison between $GSNR_{TOT}$ and the experimentally-measured GSNR is given in Fig. 5.9. As a first observation, it can be seen that for all bands except the S-band, $GSNR_{SYS}$ is the leading contributor to $GSNR_{TOT}$. For example, the maximum $GSNR_{TOT}$ value is approximately 20 dB compared to OSNR and SNR_{NL} values values of 25 – 30 dB within the L- and C-bands. This impairment is explained by the lack of device maturity within a wideband scenario such as this, as mentioned within Chapter 1 A large improvement in system performance could therefore be achieved from improvements in device performance, which will be anticipated from future research developments.

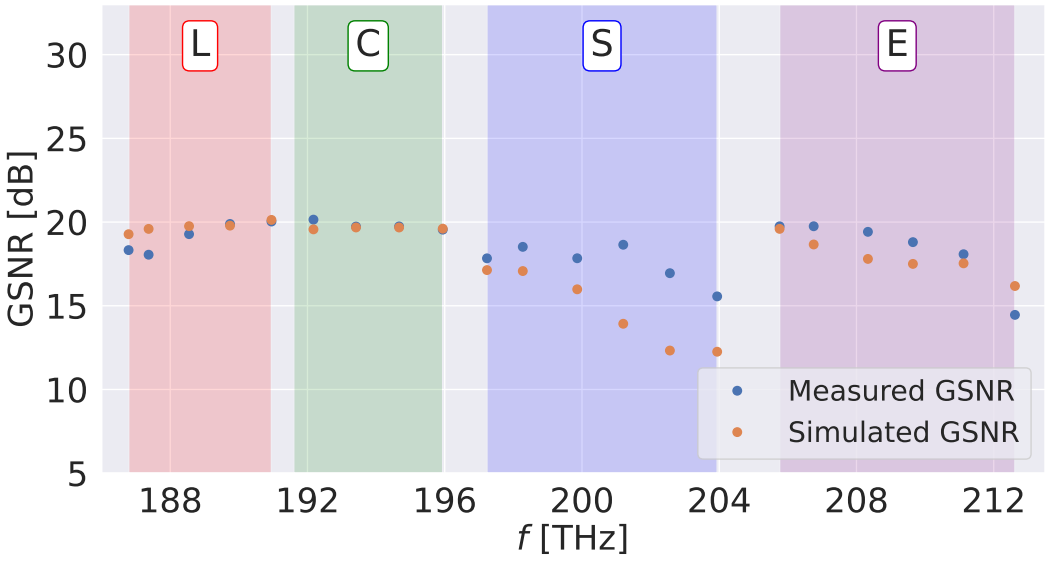

Fig. 5.9 The experimentally achieved SNR and numerically calculated GSNR values after propagation and amplification using the combined L-, C-, S-band Raman amplifier system and the E-band BDFA.

A second observation is that the simulated GSNRs in the L-, C-, and E-bands are similar to that of the measured GSNRs, with a maximum divergence of approximately 2 dB, 0.5 dB, and 2 dB for the least accurate predictions in each band, respectively. Furthermore, most of these values are conservative, except for the first three CUTs within the L-band, and the last CUT within the E-band. For these L-band CUTs, this discrepancy may be explained by small differences in the experimental and simulated Raman pump powers within the second amplification stage, whereas the discrepancy for the E-band CUT may be due to poor experimental performance at the band extremes.

The S-band, however, is a different story, as it has values that are up to approximately 3 dB lower than the experimental result within the S_2 and S_3 sub-band regions. This difference can primarily be explained by the absence of E-band impairments during the experimental transmission; as only three channels were transmitting at any given time within the experimental campaign, the effects of SRS power transfer from the E- to the S-band in this case have been minimal. Lower SRS power transfer from the E- to S-band consequently causes less NLI to be produced in the S-band, therefore resulting in a better S-band performance. This observation is supported by considering that the area around the peak of the SRS efficiency given in Fig. 2.6 corresponds closely to the difference between the S- and E-band channels.

5.7 Optimising Wideband Amplification

Besides a desire for lower RX impairments, it is visible in Figs. 5.6 and 5.9 that a significant amount of NLI has been generated in the S-band during the amplification process. The question now turns to how this NLI may be reduced or prevented, in order to seek the best possible performance within a future L-, C-, S-, E-band transmission scenario, or beyond. As mentioned in the previous subsection, the large amount of NLI generated within the S-band is primarily due to the Raman amplification being performed first within the S-band, causing this band to have a high level of power when entering the second IDF, corresponding producing a high NF and a large, uneven gain profile. Having a large S-band power in turn induces a power transfer cascade from the S-band to the C- and L-bands due to the SRS effect, which benefits these bands by enabling them to have lower input power values, reducing the NLI that they generate during SMF propagation.

Considering an idealised scenario, performing per-channel power optimisation may help to alleviate this issue by finding a balance between the NLI generation and SRS effect. Unfortunately, the presence of multiple transmission stages (propagation and dual-stage amplification) creates a scenario where there are multiple interlinked system parameters which interact in a complex, nonlinear way, meaning that evolutionary algorithms may not provide adequate performance, and instead machine learning input power optimisation may be desired. Furthermore, with the current amplification set-up, the optimal input power profile may still not yield idealised performance, and a reconsideration of the amplifier set-up might provide greater optimisation. By performing the Raman amplification in the opposite order, i.e. first amplifying the L- and C-bands, followed by the S-band, it is evident that the issue of high power in the input of the second IDF is simply shifted to the L- and C-bands, potentially worsening this problem.

From these considerations, some other approaches are envisaged as routes of investigation to improve the overall system performance, all of which ideally include a dedicated input power optimisation algorithm. As mentioned within Chapter. 1, TDFAs may be used to perform amplification in the S-band, but are still undergoing research and development and currently have higher NF values than commercially-available EDFAs or BDFAs [72, 73]. Despite this, even a high NF and lower amount of gain for the S-band spectrum may provide adequate performance, on account of the NLI generation within the Raman amplifier being avoided entirely for this band. A second option is that EDFAs may be used to amplify the C- and L-bands, and the Raman amplifier can be kept for the S-band, but only performed as a single stage after all other bands have been amplified. This would eliminate the problem of the S-band having a high input power, but may have unforeseen effects upon the C- and L-bands, potentially worsening their performance due to unwanted power transfer or the presence of ripples from the Raman amplification process.

One more suggestion is that each band could simply be amplified separately with the current amplification regime, minimising SRS effects, and allowing each band to be optimised separately, before being recombined at the end of transmission. Unfortunately, this idea seems unfeasible from a practical point of view, as it is expected to increasing experiment complexity and require a larger number of devices, potentially imparting even greater impairments, along with the likelihood that this implementation would not be an attractive in-field deployment option. It is unknown which of these approaches would yield the best GSNR, and the question of how best

to perform amplification in a L-, C-, S-, E-band transmission scenario, or greater, remains open, and is proposed here as a promising avenue for future work, in order to best realise feasible, high-capacity wideband transmission.

Chapter 6

Conclusion

In this thesis a comprehensive overview of NLI generation in disaggregated and wideband optical network architectures has been presented. First, a fully disaggregated, semi-analytical model has been presented, which has been derived from the PMD-Manakov equation with the assumption of AWGN channels, following a similar methodology to the model. This disaggregated GN model was consequently verified for a variety of partially-disaggregated C-band network infrastructures. The model was implemented using a wideband-enabled version of the open-source GNPy library as a base framework, and validated through comparison to SSFM simulations. When considering disaggregated network segments, issues in QoT estimation may arise due to history of the LP passing through the segment being unknown. By progressively applying Gaussian predistortion to the signal, the behaviour of the Gaussianisation effect upon the signal was characterised, demonstrating that, as a worst-case scenario, the disaggregated GN model may always be used to provide an upper bound for the NLI accumulation.

Next, non-uniform network segments were investigated, where the length and chromatic dispersions of the fiber spans were changed throughout a link. These simulation results have demonstrated that changes the accumulated dispersion affects the maximum amount of NLI which can be generated for a given fiber span, which causes jumps in the accumulations of the SPM and XPM impairments. By including a factor that accounts for the coherent accumulation of the SPM, the disaggregated GN model was able to provide conservative $\mathrm{SNR}_{\mathrm{NL}}$ predictions; differences in final

GSNR after 15 spans of transmission were fractions of a dB, for a system operating at its optimal working point.

The final investigation for a disaggregated transmission scenario concerned links which feature in-line dispersion compensation provided by DCUs. Small amounts of residual dispersion arising from mismatches between the fiber and DCU dispersion values was found to significantly affect the accumulation of the NLI. Besides the disaggregated GN model serving as a conservative upper bound for all scenarios, prediction improvements are possible by including information about the macroscopic behaviour of this effect, which was characterised for a broad range of scenarios, and shown to scale with the spectral and fiber parameters of the first few fiber spans.

Following these results, attention was turned towards modelling an experimental L-, C-, S-, E-band transmission scenario that has been performed by collaborators at Aston University. The behaviour of the SNR_{NL} and ASE noise contributors to the overall QoT impairment have been investigated, showing that the greatest contributor to the NLI in this scenario is due to the amplification strategy, which is found to be a delicate issue for wideband propagation. Besides this, the predicted impairment was shown to be close to the experimental results, with a maximal divergence between the two scenarios of approximately 2 dB, across the entire L-, C-, S-, E-band spectrum.

6.1 Future Works

The future works which to be undertaken after conclusion of this project may broadly be separated into the topics of NLI investigations within disaggregated network scenarios, and the optimisation of wideband transmission. Concerning the former, the results of Chapter. 4 have shown that, with use of a spectrally and spatially disaggregated model, it is possible to estimate the QoT of a disaggregated network on a span-by-span basis, including for architectures where IMDD and coherent signals are being transmitted simultaneously. The greatest observed discrepancies have been the jumps in SNR values when moving from one distinct OLS configuration to another, including for changes in dispersion compensation, and the affects that arise due to the so-called Gaussianisation of the signal. Although, as demonstrated, it is possible to put an upper bound on these effects, their evolution has not yet been fully captured.

A full characterisation of these additional impairments would provide a disaggregated model with the highest possible level of flexibility, where flex-grid, flex-rate transmission scenarios over OLSs with arbitrary configurations could be modelled with minimal margins. Quantifying the behaviour of these effects is a promising future work; the large problem space of OLS configurations and how the evolution of these effects relates to them presents an appealing avenue of investigation for machine learning techniques. Applying this model to an existing deployed network architecture would also serve as an appealing project, providing experimental validation. Additionally, some recent works have shown that Volterra filters are an effective tool for characterisation of a nonlinear impairment, and a potential application of them could be to quantify the evolution of these disaggregated impairments [196, 197].

Regarding optimisation of wideband transmission, the results in Chapter 5 have demonstrated that amplification and power management within a wideband scenario is a complex topic which will need to be properly addressed when network operators perform wideband network upgrades, particularly into the S-band, and beyond. To ensure that NLI generation is minimised during the amplification process, it is crucial that propagation does not occur with high power values, such as at the input of a Raman amplification stage. A thorough investigation should therefore be performed upon a wide variety of L-, C-, S-, E-band amplification strategies, which may include changing the configurations of the Raman pump stages, investigating use of TDFAs in the S-band, or limiting Raman amplification to the S-band. Additionally, the experimental and modelling scenario of Chapter 2 neglects to include the O-band, on account of devices within this bandwidth being at a much lower level of maturity. As mentioned within Chapter 1, the O-band also presents a greater challenge than the other bands considered within this project, as the zero-dispersion point of commonly used optical fibers is present within this band. A future work is therefore adapting the models used within this project to be able to provide NLI estimations in areas where the fiber dispersion is close to or at zero.

Calculating the NLI impairment with the SSFM library provided satisfactory results for a L-, C-, S-, E-band transmission scenario; another future work would be to investigate the accuracy of the disaggregated GN model implementation with the semi-analytical solution presented in Chapter. 2. This would fully verify the disaggregated GN model upon both disaggregated and wideband architectures, providing a model of wideband transmission impairments at much faster speeds and with a greater flexibility than the result provided by the SSFM.

References

[1] Andrea D'Amico, Stefano Straullu, Antonino Nespola, Ihtesham Khan, Elliot London, Emanuele Virgillito, Stefano Piciaccia, Aberto Tanzi, Gabriele Galimberti, and Vittorio Curri. Using machine learning in an open optical line system controller. *Journal of Optical Communications and Networking*, 12(6):C1–C11, 2020.

[2] Elliot London, Emanuele Virgillito, Andrea D'Amico, Antonio Napoli, and Vittorio Curri. Simulative assessment of non-linear interference generation within disaggregated optical line systems. *OSA continuum*, 3(12):3378–3389, 2020.

[3] Andrea D'Amico, Stefano Straullu, Giacomo Borraccini, Elliot London, Stefano Bottacchi, Stefano Piciaccia, Alberto Tanzi, Antonino Nespola, Gabriele Galimberti, Scott Swail, and Vittorio Curri. Enhancing lightpath qot computation with machine learning in partially disaggregated optical networks. *IEEE Open Journal of the Communications Society*, 2:564–574, 2021.

[4] Andrea D'Amico, Elliot London, Bertrand Le Guyader, Florian Frank, Esther Le Rouzic, Erwan Pincemin, Nicolas Brochier, and Vittorio Curri. Experimental validation of gnpy in a multi-vendor flex-grid flex-rate wdm optical transport scenario. *Journal of Optical Communications and Networking*, 14(3):79–88, 2022.

[5] Andrea D'Amico, Bruno Correia, Elliot London, Emanuele Virgillito, Giacomo Borraccini, Antonio Napoli, and Vittorio Curri. Scalable and disaggregated ggn approximation applied to a c+ l+ s optical network. *Journal of Lightwave Technology*, 2022.

[6] Elliot London, Andrea D'Amico, Emanuele Virgillito, Antonio Napoli, and Vittorio Curri. Modelling non-linear interference in non-periodic and disaggregated optical network segments. *Optics Continuum*, 1(4):793–803, 2022.

[7] Rasoul Sadeghi, Bruno Correia, Elliot London, Antonio Napoli, Nelson Costa, João Pedro, and Vittorio Curri. Performance comparison of optical networks exploiting multiple and extended bands and leveraging reinforcement learning. In *2023 International Conference on Optical Network Design and Modeling (ONDM)*, pages 1–6. IEEE, 2023.

[8] Andrea D'Amico, Elliot London, Emanuele Virgillito, Antonio Napoli, and Vittorio Curri. Quality of transmission estimation for planning of disaggregated optical networks. In *2020 International Conference on Optical Network Design and Modeling (ONDM)*, pages 1–3. IEEE, 2020.

[9] Andrea D'Amico, Elliot London, Bertrand Le Guyader, Florian Frank, Esther Le Rouzic, Erwan Pincemin, Nicolas Brochier, and Vittorio Curri. Gnpy experimental validation on flex-grid, flex-rate wdm optical transport scenarios. In *Optical Fiber Communication Conference*, pages W1G–2. Optical Society of America, 2021.

[10] Emanuele Virgillito, Elliot London, Andrea D'Amico, Bruno Correia, Antonio Napoli, and Vittorio Curri. Single-vs. multi-band optimized power control in c+ l wdm 400g line systems. In *2021 Optical Fiber Communications Conference and Exhibition (OFC)*, pages 1–3. IEEE, 2021.

[11] Andrea D'Amico, Elliot London, Emanuele Virgillito, Antonio Napoli, and Vittorio Curri. Inter-band gsnr degradations and leading impairments in c+ l band 400g transmission. In *2021 International Conference on Optical Network Design and Modeling (ONDM)*, pages 1–3. IEEE, 2021.

[12] Rasoul Sadeghi, Bruno Correia, Emanuele Virgilito, Elliot London, Nelson Costa, João Pedro, Antonio Napoli, and Vittorio Curri. Optimized translucent s-band transmission in multi-band optical networks. In *2021 European Conference on Optical Communication (ECOC)*, pages 1–4. IEEE, 2021.

[13] Elliot London, Emanuele Virgillito, Andrea D'Amico, Antonio Napoli, and Vittorio Curri. Observing cross-channel nli generation in disaggregated optical line systems. In *Asia Communications and Photonics Conference*, pages W3B–3. Optical Society of America, 2021.

[14] Vjaceslavs Bobrovs, Sandis Spolitis, and Girts Ivanovs. Latency causes and reduction in optical metro networks. In *Optical Metro Networks and Short-Haul Systems VI*, volume 9008, pages 91–101. SPIE, 2014.

[15] Jean-Marie Beaufils. How do submarine networks web the world? *Optical fiber technology*, 6(1):15–32, 2000.

[16] Cisco. Cisco visual networking index: Forecast and methodology. https://www.cisco.com/c/en/us/solutions/service-provider/visual-networking-index-vni/index.html, 2018. [Online; accessed 02-March-2023].

[17] Visual Network Index Cisco. Cisco visual networking index: forecast and methodology 2016–2021. *CISCO White paper*, 2017.

[18] Blesson Varghese and Rajkumar Buyya. Next generation cloud computing: New trends and research directions. *Future Generation Computer Systems*, 79:849–861, 2018.

[19] Panagiotis Sarigiannidis, Thomas Lagkas, Stamatia Bibi, Apostolos Ampatzoglou, and Paolo Bellavista. Hybrid 5g optical-wireless sdn-based networks, challenges and open issues. *IET Networks*, 6(6):141–148, 2017.

[20] Federico Boccardi, Robert W Heath, Angel Lozano, Thomas L Marzetta, and Petar Popovski. Five disruptive technology directions for 5g. *IEEE communications magazine*, 52(2):74–80, 2014.

[21] Gunasekaran Manogaran, Tahani Baabdullah, Danda B Rawat, and P Mohamed Shakeel. Ai-assisted service virtualization and flow management framework for 6g-enabled cloud-software-defined network-based iot. *IEEE Internet of Things Journal*, 9(16):14644–14654, 2021.

[22] Abdelhak Bentaleb, Christian Timmerer, Ali C Begen, and Roger Zimmermann. Bandwidth prediction in low-latency chunked streaming. In *Proceedings of the 29th ACM workshop on network and operating systems support for digital audio and video*, pages 7–13, 2019.

[23] Liyang Sun, Tongyu Zong, Siquan Wang, Yong Liu, and Yao Wang. Towards optimal low-latency live video streaming. *IEEE/ACM Transactions on Networking*, 29(5):2327–2338, 2021.

[24] Thomas Favale, Francesca Soro, Martino Trevisan, Idilio Drago, and Marco Mellia. Campus traffic and e-learning during covid-19 pandemic. *Computer networks*, 176:107290, 2020.

[25] Russell J Zwanka and Cheryl Buff. Covid-19 generation: A conceptual framework of the consumer behavioral shifts to be caused by the covid-19 pandemic. *Journal of International Consumer Marketing*, 33(1):58–67, 2021.

[26] Abdalmuttaleb Musleh Alsartawi, Mohamed Abdel Aziz Hegazy, and Karim Hegazy. Guest editorial: The covid-19 pandemic: a catalyst for digital transformation. *Managerial Auditing Journal*, 37(7):769–774, 2022.

[27] Erik Brynjolfsson, John J Horton, Adam Ozimek, Daniel Rock, Garima Sharma, and Hong-Yi TuYe. Covid-19 and remote work: an early look at us data. Technical report, National Bureau of Economic Research, 2020.

[28] Timm Böttger, Ghida Ibrahim, and Ben Vallis. How the internet reacted to covid-19: A perspective from facebook's edge network. In *Proceedings of the ACM Internet Measurement Conference*, pages 34–41, 2020.

[29] Anja Feldmann, Oliver Gasser, Franziska Lichtblau, Eric Pujol, Igmar Poese, Christoph Dietzel, Daniel Wagner, Matthias Wichtlhuber, Juan Tapiador, Narseo Vallina-Rodriguez, et al. Implications of the covid-19 pandemic on the internet traffic. In *Broadband Coverage in Germany; 15th ITG-Symposium*, pages 1–5. VDE, 2021.

[30] Polina Bayvel, Robert Maher, Tianhua Xu, Gabriele Liga, Nikita A Shevchenko, Domaniç Lavery, Alex Alvarado, and Robert I Killey. Maximizing the optical network capacity. *Philosophical Transactions of the Royal Society A: Mathematical, Physical and Engineering Sciences*, 374(2062):20140440, 2016.

[31] Glenn Wellbrock and Tiejun J Xia. How will optical transport deal with future network traffic growth? In *2014 The European Conference on Optical Communication (ECOC)*, pages 1–3. IEEE, 2014.

[32] Daniela Moniz, Victor Lopez, and João Pedro. Design strategies exploiting c+ l-band in networks with geographically-dependent fiber upgrade expenditures. In *Optical Fiber Communication Conference*, pages M2G–3. Optical Society of America, 2020.

[33] Peter J Winzer, David T Neilson, and Andrew R Chraplyvy. Fiber-optic transmission and networking: the previous 20 and the next 20 years. *Optics express*, 26(18):24190–24239, 2018.

[34] Yvan Pointurier. Design of low-margin optical networks. *IEEE/OSA Journal of Optical Communications and Networking*, 9(1):A9–A17, 2017.

[35] David J Ives, Polina Bayvel, and Seb J Savory. Routing, modulation, spectrum and launch power assignment to maximize the traffic throughput of a nonlinear optical mesh network. *Photonic Network Communications*, 29(3):244–256, 2015.

[36] Samuel LI Olsson, Junho Cho, Sethumadhavan Chandrasekhar, Xi Chen, Peter J Winzer, and Sergejs Makovejs. Probabilistically shaped pdm 4096-qam transmission over up to 200 km of fiber using standard intradyne detection. *Optics express*, 26(4):4522–4530, 2018.

[37] Xi Chen, Junho Cho, Andrew Adamiecki, and Peter Winzer. 16384-qam transmission at 10 gbd over 25-km ssmf using polarization-multiplexed probabilistic constellation shaping. In *45th European Conference on Optical Communication (ECOC 2019)*, pages 1–4. IET, 2019.

[38] Andrew D Ellis, Jian Zhao, and David Cotter. Approaching the non-linear shannon limit. *Journal of lightwave technology*, 28(4):423–433, 2009.

[39] Antonio Napoli, Nelson Costa, Johannes K Fischer, Joao Pedro, Silvio Abrate, Nicola Calabretta, Wladek Forysiak, Erwan Pincemin, Juan PF-P Gimenez, Chris Matrakidis, et al. Towards multiband optical systems. In *Photonic Networks and Devices*, pages NeTu3E–1. Optical Society of America, 2018.

[40] Johannes K Fischer, Mattia Cantono, Vittorio Curri, Ralf-Peter Braun, Nelson Costa, João Pedro, Erwan Pincemin, Philippe Doaré, Claude Le Bouëtté, and Antonio Napoli. Maximizing the capacity of installed optical fiber infrastructure via wideband transmission. In *2018 20th International Conference on Transparent Optical Networks (ICTON)*, pages 1–4. IEEE, 2018.

[41] Fukutaro Hamaoka, Masanori Nakamura, Seiji Okamoto, Kyo Minoguchi, Takeo Sasai, Asuka Matsushita, Etsushi Yamazaki, and Yoshiaki Kisaka. Ultra-wideband wdm transmission in s-, c-, and l-bands using signal power optimization scheme. *Journal of Lightwave Technology*, 37(8):1764–1771, 2019.

[42] Yan Ososkov, Aleksandr Khegai, Sergei Firstov, Konstantin Riumkin, Sergey Alyshev, Alexander Kharakhordin, Alexey Lobanov, Alexey Guryanov, and Mikhail Melkumov. Pump-efficient flattop o+ e-bands bismuth-doped fiber amplifier with 116 nm–3 db gain bandwidth. *Optics Express*, 29(26):44138–44145, 2021.

[43] Jay W Dawson, Leily S Kiani, Paul H Pax, Graham S Allen, Derrek R Drachenberg, Victor V Khitrov, Diana Chen, Nick Schenkel, Matthew J Cook, Robert P Crist, et al. E-band nd 3+ amplifier based on wavelength selection in an all-solid micro-structured fiber. *Optics express*, 25(6):6524–6538, 2017.

[44] Uiara Celine de Moura, Ann Margareth Rosa Brusin, Andrea Carena, Darko Zibar, and Francesco Da Ros. Simultaneous gain profile design and noise figure prediction for raman amplifiers using machine learning. *Optics Letters*, 46(5):1157–1160, 2021.

[45] Chandra B Gaur, Vladimir Gordienko, Florent Bessin, and Nick J Doran. Dual-band amplification of downstream l-band and upstream c-band signals by fopa in extended reach pon. In *2020 European Conference on Optical Communications (ECOC)*, pages 1–4. IEEE, 2020.

[46] Jeremie Renaudier, Aymeric Arnould, Amirhossein Ghazisaeidi, Dylan Le Gac, Patrick Brindel, Elie Awwad, Mathilde Makhsiyan, Karim Mekhazni, Fabrice Blache, Aurelien Boutin, et al. Recent advances in 100+ nm ultra-wideband fiber-optic transmission systems using semiconductor optical amplifiers. *Journal of Lightwave Technology*, 38(5):1071–1079, 2020.

[47] André Souza, Bruno Correia, Nelson Costa, João Pedro, and João Pires. Accurate and scalable quality of transmission estimation for wideband optical systems. In *2021 IEEE 26th International Workshop on Computer Aided Modeling and Design of Communication Links and Networks (CAMAD)*, pages 1–6. IEEE, 2021.

[48] Daniel Semrau, Robert Killey, and Polina Bayvel. Achievable rate degradation of ultra-wideband coherent fiber communication systems due to stimulated raman scattering. *Optics express*, 25(12):13024–13034, 2017.

[49] Vittorio Curri, Mattia Cantono, and Roberto Gaudino. Elastic all-optical networks: A new paradigm enabled by the physical layer. how to optimize network performances? *Journal of Lightwave Technology*, 35(6):1211–1221, 2017.

[50] Marc De Leenheer, Tom Tofigh, and Guru Parulkar. Open and programmable metro networks. In *Optical Fiber Communication Conference*, pages Th1A–7. Optical Society of America, 2016.

[51] Peter Xiang Gao, Akshay Narayan, Sagar Karandikar, Joao Carreira, Sangjin Han, Rachit Agarwal, Sylvia Ratnasamy, and Scott Shenker. Network requirements for resource disaggregation. In *OSDI*, volume 16, pages 249–264, 2016.

[52] Jose Alberto Hernandez, Marco Quagliotti, Emilio Riccardi, Victor Lopez, Oscar Gonzalez de Dios, and Ramon Casellas. A techno-economic study of optical network disaggregation employing open source software business models for metropolitan area networks. *IEEE Communications Magazine*, 58(5):40–46, 2020.

[53] Lluís Gifre, Jose-Luis Izquierdo-Zaragoza, Marc Ruiz, and Luis Velasco. Autonomic disaggregated multilayer networking. *Journal of Optical Communications and Networking*, 10(5):482–492, 2018.

[54] João Santos, Nelson Costa, and João Pedro. On the impact of deploying optical transport networks using disaggregated line systems. *Journal of Optical Communications and Networking*, 10(1):A60–A68, 2018.

[55] Luis Velasco, A Chiadò Piat, O Gonzlez, A Lord, A Napoli, P Layec, D Rafique, Antonio D'Errico, D King, M Ruiz, et al. Monitoring and data analytics for optical networking: benefits, architectures, and use cases. *IEEE Network*, 33(6):100–108, 2019.

[56] Amaro de Sousa, Paulo Monteiro, and Carlos Borges Lopes. Lightpath admission control and rerouting in dynamic flex-grid optical transport networks. *Networks*, 69(1):151–163, 2017.

[57] Danish Rafique and Luis Velasco. Machine learning for network automation: overview, architecture, and applications [invited tutorial]. *Journal of Optical Communications and Networking*, 10(10):D126–D143, 2018.

[58] Diego Kreutz, Fernando MV Ramos, Paulo Esteves Verissimo, Christian Esteve Rothenberg, Siamak Azodolmolky, and Steve Uhlig. Software-defined networking: A comprehensive survey. *Proceedings of the IEEE*, 103(1):14–76, 2014.

[59] Alexander Gelberger, Niv Yemini, and Ran Giladi. Performance analysis of software-defined networking (sdn). In *2013 IEEE 21st International Symposium on Modelling, Analysis and Simulation of Computer and Telecommunication Systems*, pages 389–393. IEEE, 2013.

[60] Nicola Sambo et al. Next generation sliceable bandwidth variable transponders. *IEEE Communications Magazine*, 53(2):163–171, 2015.

[61] Luay Alahdab, Esther Le Rouzic, Cédric Ware, Julien Meuric, Ahmed Triki, Jean-Luc Augé, and Thierry Marcot. Alien wavelengths over optical transport networks. *Journal of optical communications and networking*, 10(11):878–888, 2018.

[62] Andrew Lord, Paul Wright, and Yu Rong Zhou. Alien waves: technology, benefits and standardisation. In *2012 International Conference on Photonics in Switching (PS)*, pages 1–3. IEEE, 2012.

[63] Nazila Hashemi, Pooyan Safari, Behnam Shariati, and Johannes Karl Fischer. Vertical federated learning for privacy-preserving ml model development in partially disaggregated networks. In *2021 European Conference on Optical Communication (ECOC)*, pages 1–4. IEEE, 2021.

[64] Alessio Ferrari, Antonio Napoli, Johannes K Fischer, Nelson Costa, Joao Pedro, Nicola Sambo, Erwan Pincemin, Bernd Sommerkohrn-Krombholz, and Vittorio Curri. Upgrade capacity scenarios enabled by multi-band optical systems. In *2019 21st International Conference on Transparent Optical Networks (ICTON)*, pages 1–4. IEEE, 2019.

[65] Felton A Flood. L-band erbium-doped fiber amplifiers. In *Optical Fiber Communication Conference*, page WG1. Optical Society of America, 2000.

[66] HB Choi, JM Oh, D Lee, SJ Ahn, BS Park, and SB Lee. Simple and efficient l-band erbium-doped fiber amplifiers for wdm networks. *Optics Communications*, 213(1-3):63–66, 2002.

[67] Tanjila Ahmed, Abhijit Mitra, Sabidur Rahman, Massimo Tornatore, Andrew Lord, and Biswanath Mukherjee. C+ l-band upgrade strategies to sustain traffic growth in optical backbone networks. *Journal of Optical Communications and Networking*, 13(7):193–203, 2021.

[68] Valey Kamalov, Vinayak Dangui, Tad Hofmeister, Bikash Koley, Chris Mitchell, Matt Newland, John O'Shea, Cody Tomblin, Vijay Vusirikala, and Xiaoxue Zhao. Lessons learned from open line system deployments. In *2017 Optical Fiber Communications Conference and Exhibition (OFC)*, pages 1–3. IEEE, 2017.

[69] Mattia Cantono, Rene Schmogrow, Matt Newland, Vijay Vusirikala, and Tad Hofmeister. Opportunities and challenges of c+ l transmission systems. *Journal of Lightwave Technology*, 38(5):1050–1060, 2020.

[70] Mohammed N Islam. Raman amplifiers for telecommunications. *IEEE Journal of selected topics in Quantum Electronics*, 8(3):548–559, 2002.

[71] Tadashi Sakamoto. S-band fiber optic amplifiers. In *Optical Fiber Communication Conference*, page TuQ1. Optical Society of America, 2001.

[72] Pavel Peterka, Basile Faure, Wilfried Blanc, M Karasek, and Bernard Dussardier. Theoretical modelling of s-band thulium-doped silica fibre amplifiers. *Optical and Quantum Electronics*, 36:201–212, 2004.

[73] Abdel Hakeim M Husein and Fady I El-Nahal. Optimizing the thulium doped fiber amplifier (tdfa) gain and noise figure for s-band 16× 10 gb/s wdm systems. *Optik*, 124(19):4052–4057, 2013.

[74] Vitaly Mikhailov, MA Melkumov, Daryl Inniss, AM Khegai, KE Riumkin, SV Firstov, FV Afanasiev, Man F Yan, Yingzhi Sun, Jiawei Luo, et al. Simple broadband bismuth doped fiber amplifier (bdfa) to extend o-band transmission reach and capacity. In *Optical Fiber Communication Conference*, pages M1J–4. Optical Society of America, 2019.

[75] Aleksandr Donodin, Vladislav Dvoyrin, Egor Manuylovich, Lukasz Krzczanowicz, Wladek Forysiak, Mikhail Melkumov, Valery Mashinsky, and Sergei Turitsyn. Bismuth doped fibre amplifier operating in e-and s-optical bands. *Optical Materials Express*, 11(1):127–135, 2021.

[76] NK Thipparapu, Y Wang, S Wang, AA Umnikov, P Barua, and JK Sahu. Bi-doped fiber amplifiers and lasers. *Optical Materials Express*, 9(6):2446–2465, 2019.

[77] Jing Shao, Xiaojun Liang, and Shiva Kumar. Comparison of split-step fourier schemes for simulating fiber optic communication systems. *IEEE Photonics Journal*, 6(4):1–15, 2014.

[78] Dario Pilori, Mattia Cantono, Andrea Carena, and Vittorio Curri. Ffss: The fast fiber simulator software. In *2017 19th International Conference on Transparent Optical Networks (ICTON)*, pages 1–4. IEEE, 2017.

[79] Simone Musetti, Paolo Serena, and Alberto Bononi. On the accuracy of split-step fourier simulations for wideband nonlinear optical communications. *Journal of Lightwave Technology*, 36(23):5669–5677, 2018.

[80] Akbar Ghaffarpour Rahbar. Review of dynamic impairment-aware routing and wavelength assignment techniques in all-optical wavelength-routed networks. *IEEE Communications Surveys & Tutorials*, 14(4):1065–1089, 2011.

[81] Fabio Pittalà, Georg Böcherer, Patrick Schulte, Maximilian Schaedler, Stefano Calabrò, Bofang Zheng, Changsong Xie, and Maxim Kuschnerov. 64 tb/s dwdm transmission over 100 km g. 654d fiber using super c-band erbium-doped fiber amplification. In *Optical Fiber Communication Conference*, pages W3C–4. Optica Publishing Group, 2022.

[82] Rasoul Sadeghi, Bruno Correia, Nelson Costa, João Pedro, Antonio Napoli, and Vittorio Curri. Extending the c+ l system bandwidth versus exploiting part of the s-band: Network capacity and interface count comparison. In *European Conference and Exhibition on Optical Communication*, pages We1B–2. Optica Publishing Group, 2022.

[83] Andrew Lord, Yu Rong Zhou, Rich Jensen, Annalisa Morea, and Marc Ruiz. Evolution from wavelength-switched to flex-grid optical networks. *Elastic*

Optical Networks: Architectures, Technologies, and Control, pages 7–30, 2016.

[84] Luis Velasco, Miroslaw Klinkowski, Marc Ruiz, and Jaume Comellas. Modeling the routing and spectrum allocation problem for flexgrid optical networks. *Photonic Netw. Commun.*, 24(3):177–186, 2012.

[85] Alessio Ferrari, Antonio Napoli, Johannes Karl Fischer, Nelson Manuel Simes da Costa, Andrea D'Amico, Joao Pedro, Wladek Forysiak, Erwan Pincemin, Andrew Lord, Alexandros Stavdas, et al. Assessment on the achievable throughput of multi-band ITU-T G. 652. D fiber transmission systems. *Journal of Lightwave Technology*, 2020.

[86] Emanuele Virgillito, Andrea Castoldi, Andrea D'Amico, Stefano Straullu, Silvio Abrate, Rosanna Pastorelli, and Vittorio Curri. Propagation effects in mixed 10g-100g dispersion managed optical links. In *2019 21st International Conference on Transparent Optical Networks (ICTON)*, pages 1–4. IEEE, 2019.

[87] Xiang Liu and S Chandrasekhar. High spectral-efficiency mixed 10g/40g/100g transmission. In *Asia Optical Fiber Communication and Optoelectronic Exposition and Conference*, page SuA2. Optica Publishing Group, 2008.

[88] Avishek Nag and Massimo Tornatore. Transparent optical network design with mixed line rates. In *2008 2nd International Symposium on Advanced Networks and Telecommunication Systems*, pages 1–3. IEEE, 2008.

[89] Eugen Lach and Wilfried Idler. Modulation formats for 100g and beyond. *Optical Fiber Technology*, 17(5):377–386, 2011.

[90] Peter J Winzer and Ren-Jean Essiambre. Advanced modulation formats for high-capacity optical transport networks. *Journal of Lightwave Technology*, 24(12):4711–4728, 2006.

[91] Govind P Agrawal. Nonlinear fiber optics. In *Nonlinear Science at the Dawn of the 21st Century*, pages 195–211. Springer, 2000.

[92] Tingye Li. *Optical fiber communications: fiber fabrication*. Elsevier, 2012.

[93] Bob Chomycz. *Planning fiber optics networks*. McGraw-Hill Education, 2009.

[94] Kyozo Tsujikawa, Katsusuke Tajima, and Jian Zhou. Intrinsic loss of optical fibers. *Optical Fiber Technology*, 11(4):319–331, 2005.

[95] Masataka Nakazawa. Rayleigh backscattering theory for single-mode optical fibers. *JOSA*, 73(9):1175–1180, 1983.

[96] R-J Essiambre, Peter Winzer, Jake Bromage, and Chul Han Kim. Design of bidirectionally pumped fiber amplifiers generating double rayleigh backscattering. *IEEE Photonics Technology Letters*, 14(7):914–916, 2002.

[97] SAE Lewis, SV Chernikov, and JR Taylor. Characterization of double rayleigh scatter noise in raman amplifiers. *IEEE Photonics Technology Letters*, 12(5):528–530, 2000.

[98] Oliver Humbach, H Fabian, U Grzesik, U Haken, and W Heitmann. Analysis of oh absorption bands in synthetic silica. *Journal of non-crystalline solids*, 203:19–26, 1996.

[99] MICHAEL Bredol, Dieter Leers, Lex Bosselaar, and M Hutjens. Improved model for oh absorption in optical fibers. *Journal of Lightwave Technology*, 8(10):1536–1540, 1990.

[100] S Walker. Rapid modeling and estimation of total spectral loss in optical fibers. *Journal of lightwave technology*, 4(8):1125–1131, 1986.

[101] K Inada. A new graphical method relating to optical fiber attenuation. *Optics Communications*, 19(3):437–439, 1976.

[102] Giacomo Borraccini, Andrea D'Amico, Stefano Straullu, Antonino Nespola, Stefano Piciaccia, Alberto Tanzi, Gabriele Galimberti, Stefano Bottacchi, Scott Swail, and Vittorio Curri. Cognitive and autonomous QoT-driven optical line controller. *Journal of Optical Communications and Networking*, 13(10):E23–E31, 2021.

[103] Emanuele Virgillito, Andrea Castoldi, Stefano Straullu, Rosanna Pastorelli, and Vittorio Curri. Qot computation for 100g lightpaths routed on 10g-loaded dispersion-managed network segments. In *2021 International Conference on Electrical, Communication, and Computer Engineering (ICECCE)*, pages 1–6. IEEE, 2021.

[104] Detlef Gloge. Weakly guiding fibers. *Applied optics*, 10(10):2252–2258, 1971.

[105] RH Stolen and A Ashkin. Optical kerr effect in glass waveguide. *Applied Physics Letters*, 22(6):294–296, 1973.

[106] Pierluigi Poggiolini. The GN model of non-linear propagation in uncompensated coherent optical systems. *Journal of Lightwave Technology*, 30(24):3857–3879, 2012.

[107] P Poggiolini and Y Jiang. Recent advances in the modeling of the impact of nonlinear fiber propagation effects on uncompensated coherent transmission systems. *Journal of Lightwave Technology*, 35(3):458–480, 2016.

[108] Vittorio Curri. Software-defined wdm optical transport in disaggregated open optical networks. In *2020 22nd International Conference on Transparent Optical Networks (ICTON)*, pages 1–4. IEEE, 2020.

[109] Vittorio Curri, Andrea Carena, Pierluigi Poggiolini, Gabriella Bosco, and Fabrizio Forghieri. Extension and validation of the GN model for non-linear interference to uncompensated links using Raman amplification. *Optics express*, 21(3):3308–3317, 2013.

[110] Andrea Carena, Vittorio Curri, Gabriella Bosco, Pierluigi Poggiolini, and F Forghieri. Modeling of the impact of nonlinear propagation effects in uncompensated optical coherent transmission links. *Journal of Lightwave technology*, 30(10):1524–1539, 2012.

[111] Mattia Cantono, Dario Pilori, Alessio Ferrari, Clara Catanese, Jordane Thouras, Jean-Luc Augé, and Vittorio Curri. On the interplay of nonlinear interference generation with stimulated raman scattering for QoT estimation. *Journal of Lightwave Technology*, 36(15):3131–3141, 2018.

[112] Pontus Johannisson and Magnus Karlsson. Perturbation analysis of nonlinear propagation in a strongly dispersive optical communication system. *Journal of Lightwave Technology*, 31(8):1273–1282, 2013.

[113] P Serena and A Bononi. On the accuracy of the gaussian nonlinear model for dispersion-unmanaged coherent links. *PDM*, 25:30, 2013.

[114] GitHub repository of GNPy. https://github.com/Telecominfraproject/oopt-gnpy. [Online; accessed 02-May-2023].

[115] Alessio Ferrari, Mark Filer, Karthikeyan Balasubramanian, Yawei Yin, Esther Le Rouzic, Jan Kundrát, Gert Grammel, Gabriele Galimberti, and Vittorio Curri. Gnpy: an open source application for physical layer aware open optical networks. *Journal of Optical Communications and Networking*, 12(6):C31–C40, 2020.

[116] Jan Kundrát, Andrea Campanella, Esther Le Rouzic, Alessio Ferrari, Ondřej Havliš, Michal Hažlinskỳ, Gert Grammel, Gabriele Galimberti, and Vittorio Curri. Physical-layer awareness: Gnpy and onos for end-to-end circuits in disaggregated networks. In *Optical Fiber Communication Conference*, pages M3Z–17. Optica Publishing Group, 2020.

[117] A Bononi, P Serena, N Rossi, E Grellier, and F Vacondio. Modeling nonlinearity in coherent transmissions with dominant intrachannel-four-wave-mixing. *Optics Express*, 20(7):7777–7791, 2012.

[118] Antonio Mecozzi and René-Jean Essiambre. Nonlinear shannon limit in pseudolinear coherent systems. *Journal of Lightwave Technology*, 30(12):2011–2024, 2012.

[119] Marco Secondini and Enrico Forestieri. Analytical fiber-optic channel model in the presence of cross-phase modulation. *IEEE Photonics Technology Letters*, 24(22):2016–2019, 2012.

[120] Ronen Dar, Meir Feder, Antonio Mecozzi, and Mark Shtaif. Pulse collision picture of inter-channel nonlinear interference in fiber-optic communications. *Journal of Lightwave Technology*, 34(2):593–607, 2016.

[121] Nicola Rossi, Paolo Serena, and Alberto Bononi. Symbol-rate dependence of dominant nonlinearity and reach in coherent wdm links. *Journal of Lightwave Technology*, 33(14):3132–3143, 2015.

[122] Marco Secondini and Enrico Forestieri. On xpm mitigation in wdm fiber-optic systems. *IEEE Photonics Technology Letters*, 26(22):2252–2255, 2014.

[123] Ronen Dar, Meir Feder, Antonio Mecozzi, and Mark Shtaif. Properties of nonlinear noise in long, dispersion-uncompensated fiber links. *Optics Express*, 21(22):25685–25699, 2013.

[124] Emanuele Virgillito, Andrea D'Amico, Alessio Ferrari, and Vittorio Curri. Observing and modeling wideband generation of non-linear interference. In *2019 21st International Conference on Transparent Optical Networks (ICTON)*, pages 1–4. IEEE, 2019.

[125] Andrea Carena, Gabriella Bosco, Vittorio Curri, Yanchao Jiang, Pierluigi Poggiolini, and Fabrizio Forghieri. EGN model of non-linear fiber propagation. *Optics express*, 22(13):16335–16362, 2014.

[126] David N Payne, Arthur J Barlow, and JJ Ramskov Hansen. Development of low-and high-birefringence optical fibers. *IEEE Transactions on microwave theory and techniques*, 30(4):323–334, 1982.

[127] Andrea Galtarossa, Luca Palmieri, Marco Schiano, and Tiziana Tambosso. Statistical characterization of fiber random birefringence. *Optics Letters*, 25(18):1322–1324, 2000.

[128] D Breuer, H-J Tessmann, A Gladisch, HM Foisel, G Neumann, H Reiner, and H Cremer. Measurements of pmd in the installed fiber plant of deutsche telekom. In *2003 Digest of LEOS Summer Topical Meeting (Cat. No. 03TH8701)*, pages MB2–1. IEEE, 2003.

[129] Gerard J Foschini, RM Jopson, Lynn E Nelson, and Herwig Kogelnik. The statistics of pmd-induced chromatic fiber dispersion. *Journal of lightwave technology*, 17(9):1560, 1999.

[130] Henrik Sunnerud, Chongjin Xie, Magnus Karlsson, Robert Samuelsson, and Peter A Andrekson. A comparison between different pmd compensation techniques. *Journal of Lightwave Technology*, 20(3):368–378, 2002.

[131] Ezra M Ip and Joseph M Kahn. Fiber impairment compensation using coherent detection and digital signal processing. *Journal of Lightwave Technology*, 28(4):502–519, 2009.

[132] Jake Bromage. Raman amplification for fiber communications systems. *journal of lightwave technology*, 22(1):79–93, 2004.

[133] Gabriella Bosco. Complexity versus accuracy tradeoffs in nonlinear fiber propagation models. In *Optical Fiber Communication Conference*, pages W4H–1. Optica Publishing Group, 2023.

[134] Antonino Nespola, M Huchard, Gabriella Bosco, Andrea Carena, Y Jiang, Pierluigi Poggiolini, and Fabrizio Forghieri. Experimental validation of the egn-model in uncompensated optical links. In *2015 Optical Fiber Communications Conference and Exhibition (OFC)*, pages 1–3. IEEE, 2015.

[135] P Poggiolini, Y Jiang, A Carena, and F Forghieri. A simple and accurate closed-form egn model formula. *arXiv preprint arXiv:1503.04132*, 2015.

[136] MA Amirabadi, MH Kahaei, SA Nezamalhosseini, F Arpanaei, and A Carena. Closed-form egn model for fmf systems. In *Asia Communications and Photonics Conference*, pages T4A–33. Optica Publishing Group, 2021.

[137] M Ranjbar Zefreh, Andrea Carena, Fabrizio Forghieri, Stefano Piciaccia, and Pierluigi Poggiolini. A gn/egn-model real-time closed-form formula tested over 7,000 virtual links. In *45th European Conference on Optical Communication (ECOC 2019)*, pages 1–4. IET, 2019.

[138] Mattia Cantono, Dario Pilori, Alessio Ferrari, and Vittorio Curri. Introducing the generalized gn-model for nonlinear interference generation including space/frequency variations of loss/gain. *arXiv preprint arXiv:1710.02225*, 2017.

[139] M Cantono, A Ferrari, D Pilori, E Virgillito, JL Augé, and V Curri. Physical layer performance of multi-band optical line systems using raman amplification. *Journal of Optical Communications and Networking*, 11(1):A103–A110, 2019.

[140] Ronen Dar, Meir Feder, Antonio Mecozzi, and Mark Shtaif. Inter-channel nonlinear interference noise in wdm systems: Modeling and mitigation. *Journal of Lightwave Technology*, 33(5):1044–1053, 2014.

[141] Vinicius Oliari, Erik Agrell, and Alex Alvarado. Regular perturbation on the group-velocity dispersion parameter for nonlinear fibre-optical communications. *Nature communications*, 11(1):1–11, 2020.

[142] Geeta Arora, Richa Rani, and Homan Emadifar. Numerical solutions of nonlinear schrodinger equation with applications in optical fiber communication. *Optik*, 266:169661, 2022.

[143] Paolo Serena and Alberto Bononi. An alternative approach to the gaussian noise model and its system implications. *Journal of Lightwave Technology*, 31(22):3489–3499, 2013.

[144] Paolo Serena, Chiara Lasagni, Simone Musetti, and Alberto Bononi. On numerical simulations of ultra-wideband long-haul optical communication systems. *Journal of Lightwave Technology*, 38(5):1019–1031, 2019.

[145] Abhijit Mitra, Daniel Semrau, Nishant Gahlawat, Anand Srivastava, Polina Bayvel, and Andrew Lord. Effect of channel launch power on fill margin in c+ l band elastic optical networks. *Journal of Lightwave Technology*, 38(5):1032–1040, 2019.

[146] Daniel Semrau, Eric Sillekens, Robert I Killey, and Polina Bayvel. The isrs gn model, an efficient tool in modeling ultra-wideband transmission in point-to-point and network scenarios. In *2018 European Conference on Optical Communication (ECOC)*, pages 1–3. IEEE, 2018.

[147] Daniel Semrau, Robert I Killey, and Polina Bayvel. The gaussian noise model in the presence of inter-channel stimulated raman scattering. *Journal of Lightwave Technology*, 36(14):3046–3055, 2018.

[148] Chiara Lasagni, Paolo Serena, and Alberto Bononi. A Raman-aware enhanced GN-model to estimate the modulation format dependence of the snr tilt in C+L band. In *45th European Conference on Optical Communication (ECOC 2019)*, pages 1–4. IET, 2019.

[149] Henrique Buglia, Mindaugas Jarmolovičius, Anastasiia Vasylchenkova, Eric Sillekens, Lidia Galdino, Polina Bayvel, and Robert Killey. A closed-form expression for the isrs gn model supporting distributed raman amplification. In *Optical Fiber Communication Conference*, pages W2A–29. Optica Publishing Group, 2023.

[150] Lidia Galdino, Daniel Semrau, Maria Ionescu, Adrian Edwards, Wayne Pelouch, Steve Desbruslais, Jeanne James, Eric Sillekens, Domaniç Lavery, Stuart Barnes, et al. Study on the impact of nonlinearity and noise on the performance of high-capacity broadband hybrid raman-edfa amplified system. *Journal of Lightwave Technology*, 37(21):5507–5515, 2019.

[151] Salma Escobar-Landero, Xiaohui Zhao, Abel Lorences-Riesgo, Dylan Le Gac, Yann Frignac, and Gabriel Charlet. Modeling and optimization of experimental s+ c+ l wdm coherent transmission system. In *Optical Fiber Communication Conference*, pages Th3F–4. Optica Publishing Group, 2023.

[152] Daniel Semrau, Eric Sillekens, Robert I Killey, and Polina Bayvel. The benefits of using the s-band in optical fiber communications and how to get there. In *2020 IEEE Photonics Conference (IPC)*, pages 1–2. IEEE, 2020.

[153] Antonino Nespola, Stefano Straullu, Andrea Carena, Gabriella Bosco, Roberto Cigliutti, Vittorio Curri, Pierluigi Poggiolini, Masaaki Hirano, Yoshinori Yamamoto, Takashi Sasaki, et al. GN-model validation over seven fiber types in uncompensated PM-16QAM Nyquist-WDM links. *IEEE Photonics Technology Letters*, 26(2):206–209, 2013.

[154] Mark Filer, Mattia Cantono, Alessio Ferrari, Gert Grammel, Gabriele Galimberti, and Vittorio Curri. Multi-vendor experimental validation of an open source qot estimator for optical networks. *Journal of Lightwave Technology*, 36(15):3073–3082, 2018.

[155] Han Sun, Mehdi Torbatian, Mehdi Karimi, Robert Maher, Sandy Thomson, Mohsen Tehrani, Yuliang Gao, Ales Kumpera, George Soliman, Aditya Kakkar, et al. 800G DSP ASIC design using probabilistic shaping and digital sub-carrier multiplexing. *Journal of Lightwave Technology*, 2020.

[156] Dietrich Marcuse, CR Manyuk, and Ping Kong Alexander Wai. Application of the manakov-pmd equation to studies of signal propagation in optical fibers with randomly varying birefringence. *Journal of Lightwave Technology*, 15(9):1735–1746, 1997.

[157] Karsten Rottwitt, Jake Bromage, Andrew J Stentz, Lufeng Leng, Malcolm E Lines, and Henrik Smith. Scaling of the Raman gain coefficient: applications to germanosilicate fibers. *Journal of lightwave technology*, 21(7):1652, 2003.

[158] A Carena, G Bosco, V Curri, P Poggiolini, and F Forghieri. Impact of the transmitted signal initial dispersion transient on the accuracy of the GN-model of non-linear propagation. In *39th European Conference and Exhibition on Optical Communication (ECOC 2013)*, pages 1–3. IET, 2013.

[159] David J Ives, Polina Bayvel, and Seb J Savory. Adapting transmitter power and modulation format to improve optical network performance utilizing the gaussian noise model of nonlinear impairments. *Journal of Lightwave Technology*, 32(21):3485–3494, 2014.

[160] Dan L Philen, Ian A White, Jane F Kuhl, and Stephen C Mettler. Single-mode fiber otdr: Experiment and theory. *IEEE Transactions on Microwave Theory and Techniques*, 30(10):1487–1496, 1982.

[161] Ankush Mahajan, Konstantinos Christodoulopoulos, Ricardo Martínez, Salvatore Spadaro, and Raul Muñoz. Modeling edfa gain ripple and filter penalties with machine learning for accurate qot estimation. *Journal of Lightwave Technology*, 38(9):2616–2629, 2020.

[162] Alessio Ferrari, Giacomo Borraccini, and Vittorio Curri. Observing the generalized snr statistics induced by gain/loss uncertainties. In *45th European Conference on Optical Communication (ECOC 2019)*, pages 1–4. IET, 2019.

[163] Shengxiang Zhu, Craig Gutterman, Alan Diaz Montiel, Jiakai Yu, Marco Ruffini, Gil Zussman, and Daniel Kilper. Hybrid machine learning edfa model. In *Optical Fiber Communication Conference*, pages T4B–4. Optical Society of America, 2020.

[164] Emmanuel Seve, Jelena Pesic, and Yvan Pointurier. Accurate qot estimation by means of a reduction of edfa characteristics uncertainties with machine learning. In *2020 International Conference on Optical Network Design and Modeling (ONDM)*, pages 1–3. IEEE, 2020.

[165] Giacomo Borraccini, Renato Ambrosone, Alessio Giorgetti, Stefano Straullu, Francesco Aquilino, Emanuele Virgillito, Andrea D'Amico, Rocco D'Ingillo,

Nicola Sambo, Filippo Cugini, et al. Disaggregated optical network orchestration based on the physical layer digital twin. In *Optical Fiber Communication Conference*, pages Tu3D–4. Optica Publishing Group, 2023.

[166] Danshi Wang, Zhiguo Zhang, Min Zhang, Meixia Fu, Jin Li, Shanyong Cai, Chunyu Zhang, and Xue Chen. The role of digital twin in optical communication: fault management, hardware configuration, and transmission simulation. *IEEE Communications Magazine*, 59(1):133–139, 2021.

[167] M Devigili, M Ruiz, N Costa, A Napoli, J Pedro, and L Velasco. Dual time and frequency domain optical layer digital twin. In *European Conference and Exhibition on Optical Communication*, pages Tu5–42. Optica Publishing Group, 2022.

[168] Vittorio Curri. Gnpy model of the physical layer for open and disaggregated optical networking. *Journal of optical communications and networking*, 14(6):C92–C104, 2022.

[169] Jan Kundrát, Esther Le Rouzic, Jonas Mårtensson, Stefan Melin, Andrea D'Amico, Gert Grammel, Gabriele Galimberti, and Vittorio Curri. Gnpy: Lessons learned and future plans. In *European Conference and Exhibition on Optical Communication*, pages We3B–6. Optica Publishing Group, 2022.

[170] Simone Gaiarin, Francesco Da Ros, Rasmus T Jones, and Darko Zibar. End-to-end optimization of coherent optical communications over the split-step fourier method guided by the nonlinear fourier transform theory. *Journal of Lightwave Technology*, 39(2):418–428, 2020.

[171] M Aleshams, A Zarifkar, and MH Sheikhi. Split-step fourier transform method in modeling of pulse propagation in dispersive nonlinear optical fibers. In *Proceedings of CAOL 2005. Second International Conference on Advanced Optoelectronics and Lasers, 2005.*, volume 2, pages 124–126. IEEE, 2005.

[172] Mehdi Dehghan and Ameneh Taleei. A compact split-step finite difference method for solving the nonlinear schrödinger equations with constant and variable coefficients. *Computer Physics Communications*, 181(1):43–51, 2010.

[173] Frederick Tappert. Numerical solutions of the korteweg-de vries equation and its generalizations by the split-step fourier method. *Nonlinear Wave Motion*, 15:215–216, 1974.

[174] Marek Jaworski. Step-size distribution strategies in ssfm simulation of dwdm links. In *2008 2nd ICTON Mediterranean Winter*, pages 1–6. IEEE, 2008.

[175] Chien-Yu Lin, Rameez Asif, Michael Holtmannspoetter, and Bernhard Schmauss. Step-size selection for split-step based nonlinear compensation with coherent detection in 112-gb/s 16-qam transmission. *Chinese Optics Letters*, 10(2):020605, 2012.

[176] Paul Heckbert. Fourier transforms and the fast fourier transform (fft) algorithm. *Computer Graphics*, 2:15–463, 1995.

[177] Faster Finite Fourier Transforms MATLAB. https://uk.mathworks.com/company/newsletters/articles/faster-finite-fourier-transforms-matlab.html, 2023. [Online; accessed 18-May-2023].

[178] Stephan Hellerbrand and Norbert Hanik. Fast implementation of the split-step fourier method using a graphics processing unit. In *2010 Conference on Optical Fiber Communication (OFC/NFOEC), collocated National Fiber Optic Engineers Conference*, pages 1–3. IEEE, 2010.

[179] Syed Muhammad Bilal, Chris RS Fludger, Vittorio Curri, and Gabriella Bosco. Multistage carrier phase estimation algorithms for phase noise mitigation in 64-quadrature amplitude modulation optical systems. *Journal of Lightwave Technology*, 32(17):2973–2980, 2014.

[180] Andrew Viterbi. Nonlinear estimation of PSK-modulated carrier phase with application to burst digital transmission. *IEEE Transactions on Information theory*, 29(4):543–551, 1983.

[181] R Pastorelli, S Piciaccia, G Galimberti, E Self, M Brunella, G Calabretta, F Forghieri, D Siracusa, A Zanardi, E Salvadori, et al. Optical control plane based on an analytical model of non-linear transmission effects in a self-optimized network. In *39th European Conference and Exhibition on Optical Communication (ECOC 2013)*, pages 1–3. IET, 2013.

[182] Emanuele Virgillito, Andrea Castoldi, Andrea D'Amico, Stefano Straullu, Rudi Bratovich, Fransisco M Rodriguez, Andrea Bovio, Rosanna Pastorelli, and Vittorio Curri. Spatially disaggregated modelling of self-channel nli in mixed fibers optical transmission. In *2022 European Conference on Optical Communication (ECOC)*, pages 1–4. IEEE, 2022.

[183] Masoud Vejdannik and Ali Sadr. Channel power optimization in wdm systems using co-evolutionary genetic algorithm. *Optical Switching and Networking*, 43:100637, 2022.

[184] Seb J Savory, Robert J Vincent, and David J Ives. Design considerations for low-margin elastic optical networks in the nonlinear regime. *Journal of Optical Communications and Networking*, 11(10):C76–C85, 2019.

[185] Bruno Correia, Rasoul Sadeghi, Emanuele Virgillito, Antonio Napoli, Nelson Costa, João Pedro, and Vittorio Curri. Optical power control strategies for optimized c+ l+ s-bands network performance. In *Optical Fiber Communication Conference*, pages W1F–8. Optica Publishing Group, 2021.

[186] Zhuili Huang, Liang Dou, Jingchi Cheng, Chongjin Xie, Chao Lu, and Alan Pak Tao Lau. Performance improvements by dynamic amplifier reconfigurations for c+ l-band optical networks in the presence of stimulated raman

scattering. *Journal of Optical Communications and Networking*, 15(6):344–356, 2023.

[187] Yihao Zhang, Xiaomin Liu, Ruoxuan Gao, Lilin Yi, Weisheng Hu, and Qunbi Zhuge. Raman pump optimization for maximizing capacity of c+ l optical transmission systems. *Journal of Lightwave Technology*, 40(24):7814–7825, 2022.

[188] Sam Nallaperuma, Nikita A Shevchenko, and Seb J Savory. Parameter optimisation for ultra-wideband optical networks in the presence of stimulated raman scattering effect. In *2021 International Conference on Optical Network Design and Modeling (ONDM)*, pages 1–6. IEEE, 2021.

[189] H Buglia, E Sillekens, A Vasylchenkova, P Bayvel, and L Galdino. On the impact of launch power optimization and transceiver noise on the performance of ultra-wideband transmission systems. *Journal of Optical Communications and Networking*, 14(5):B11–B21, 2022.

[190] Huaijian Luo, Jianing Lu, Zhuili Huang, Changyuan Yu, and Chao Lu. Optimization strategy of power control for c+ l+ s band transmission using a simulated annealing algorithm. *Optics Express*, 30(1):664–675, 2022.

[191] Bahadır Hiçdurmaz. Determination of the optimal input channel powers using particle swarm optimization algorithm in a wdm system with in-line optical amplifiers. *Optical Fiber Technology*, 77:103254, 2023.

[192] Teng Wang, Wantao Li, Roberto Quaglia, and Pere L Gilabert. Machine-learning assisted optimisation of free-parameters of a dual-input power amplifier for wideband applications. *Sensors*, 21(8):2831, 2021.

[193] Aleksandr Donodin, Vladislav Dvoyrin, Egor Manuylovich, Ian Phillips, Wladek Forysiak, Mikhail Melkumov, Valery Mashinsky, and Sergei Turitsyn. 4-channel e-band data transmission over 160 km of smf-28 using a bismuth-doped fibre amplifier. In *Optical Fiber Communication Conference*, pages Tu1E–3. Optica Publishing Group, 2021.

[194] Md Asif Iqbal, Paul Harper, and Wladek Forysiak. Improved design of ultra-wideband discrete raman amplifier with low noise and high gain. In *Nonlinear Photonics*, pages NpTh1H–2. Optical Society of America, 2018.

[195] Lukasz Krzczanowicz, Mohammad Ahmad Zaki Al-Khateeb, Md Asif Iqbal, Ian Phillips, Paul Harper, and Wladek Forysiak. Performance estimation of discrete raman amplification within broadband optical networks. In *Optical Fiber Communication Conference*, pages Tu3F–4. Optica Publishing Group, 2019.

[196] Gabriel Saavedra, Gabriele Liga, and Polina Bayvel. Volterra-assisted optical phase conjugation: A hybrid optical-digital scheme for fiber nonlinearity compensation. *Journal of Lightwave Technology*, 37(10):2467–2479, 2019.

[197] Zhaoyi Pan, Benoît Châtelain, Mathieu Chagnon, and David V Plant. Volterra filtering for nonlinearity impairment mitigation in dp-16qam and dp-qpsk fiber optic communication systems. In *Optical Fiber Communication Conference*, page JThA040. Optical Society of America, 2011.

[198] Emile Archambault, Nabih Alloune, Marija Furdek, Zhenyu Xu, Christine Tremblay, Ajmal Muhammad, Jiajia Chen, Lena Wosinska, Paul Littlewood, and Michel P Bélanger. Routing and spectrum assignment in elastic filterless optical networks. *IEEE/ACM Transactions On Networking*, 24(6):3578–3592, 2016.

[199] Ping Kong Alexander Wai and CR Menyak. Polarization mode dispersion, decorrelation, and diffusion in optical fibers with randomly varying birefringence. *Journal of Lightwave Technology*, 14(2):148–157, 1996.

[200] Dario Pilori, Mattia Cantono, Alessio Ferrari, Andrea Carena, and Vittorio Curri. Observing the effect of polarization mode dispersion on nonlinear interference generation in wide-band optical links. *OSA continuum*, 2(10):2856–2863, 2019.

[201] David W Boertjes, Michael Reimer, and David Côté. Practical considerations for near-zero margin network design and deployment. *Journal of Optical Communications and Networking*, 11(9):C25–C34, 2019.

[202] Polyzois Soumplis, Konstantinos Christodoulopoulos, Marco Quagliotti, Annachiara Pagano, and Emmanouel Varvarigos. Network planning with actual margins. *Journal of Lightwave Technology*, 35(23):5105–5120, 2017.

[203] Gordon A Thomas, Boris I Shraiman, Paul F Glodis, and Michael J Stephen. Towards the clarity limit in optical fibre. *Nature*, 404(6775):262–264, 2000.

[204] Daniel Semrau, Eric Sillekens, Polina Bayvel, and Robert I Killey. Modeling and mitigation of fiber nonlinearity in wideband optical signal transmission. *Journal of Optical Communications and Networking*, 12(6):C68–C76, 2020.

[205] Andrea Carena, Gabriella Bosco, Vittorio Curri, Pierluigi Poggiolini, M Tapia Taiba, and F Forghieri. Statistical characterization of PM-QPSK signals after propagation in uncompensated fiber links. In *36th European Conference and Exhibition on Optical Communication*, pages 1–3. IEEE, 2010.

[206] Mohsen Riahi Manesh, Adnan Quadri, Sriram Subramaniam, and Naima Kaabouch. An optimized snr estimation technique using particle swarm optimization algorithm. In *2017 IEEE 7th Annual Computing and Communication Workshop and Conference (CCWC)*, pages 1–6. IEEE, 2017.

[207] Data sheet for the ITU-T G.652 fiber type, corresponding to standard single mode fiber. https://www.itu.int/rec/dologin_pub.asp?lang=e&id=T-REC-G.652-201611-I!!PDF-E&type=items, 2016. [Online; accessed 02-May-2023].

[208] K. Roberts et al. Beyond 100 gb/s: capacity, flexibility, and network optimization. *IEEE/OSA Journal of Optical Communications and Networking*, 9(4):C12–C23, 2017.

[209] Infinera. Infinera sets highest-performance 600g transmission record. https://www.infinera.com/press-release/infinera-sets-highest-performance-600g-transmission-record, 2019. [Online; accessed 02-March-2023].

[210] Charalampos Papapavlou, Konstantinos Paximadis, Dimitrios Uzunidis, and Ioannis Tomkos. Toward sdm-based submarine optical networks: A review of their evolution and upcoming trends. In *Telecom*, volume 3, pages 234–280. MDPI, 2022.

[211] Masahiko Jinno, Hidehiko Takara, Bartlomiej Kozicki, Yukio Tsukishima, Yoshiaki Sone, and Shinji Matsuoka. Spectrum-efficient and scalable elastic optical path network: architecture, benefits, and enabling technologies. *IEEE communications magazine*, 47(11):66–73, 2009.

[212] Mark Filer, Hacene Chaouch, and Xiaoxia Wu. Toward transport ecosystem interoperability enabled by vendor-diverse coherent optical sources over an open line system. *IEEE/OSA Journal of Optical Communications and Networking*, 10(2):A216–A224, 2018.

[213] Pierluigi Poggiolini, G Bosco, A Carena, V Curri, Y Jiang, and F Forghieri. The gn-model of fiber non-linear propagation and its applications. *Journal of lightwave technology*, 32(4):694–721, 2013.

[214] Jean-Luc Auge, Gert Grammel, Esther Le Rouzic, Vittorio Curri, Gabriele Galimberti, and James Powell. Open optical network planning demonstration. In *Optical Fiber Communication Conference*, pages M3Z–9. Optical Society of America, 2019.

[215] Takeshi Hoshida, Vittorio Curri, Lidia Galdino, David T Neilson, Wladek Forysiak, Johannes K Fischer, Tomoyuki Kato, and Pierluigi Poggiolini. Ultrawideband systems and networks: Beyond c+ l-band. *Proceedings of the IEEE*, 110(11):1725–1741, 2022.

[216] Ernst-Georg Neumann. *Single-mode fibers: fundamentals*, volume 57. Springer, 2013.

[217] Emilio Riccardi, Paul Gunning, Óscar González de Dios, Marco Quagliotti, Víctor López, and Andrew Lord. An operator view on the introduction of white boxes into optical networks. *Journal of Lightwave Technology*, 36(15):3062–3072, 2018.

[218] Jan Kundrát, Ondřej Havliš, Jaroslav Jedlinskỳ, and Josef Vojtěch. Opening up roadms: Let us build a disaggregated open optical line system. *Journal of Lightwave Technology*, 37(16):4041–4051, 2019.

[219] Antonio Mecozzi and Francesco Matera. Polarization scattering by intra-channel collisions. *Optics express*, 20(2):1213–1218, 2012.

[220] Metodi Plamenov Yankov, Pawel Marcin Kaminski, Henrik Enggaard Hansen, and Francesco Da Ros. Snr optimization of multi-span fiber optic communication systems employing edfas with non-flat gain and noise figure. *Journal of Lightwave Technology*, 39(21):6824–6832, 2021.

[221] Seb J Savory, Giancarlo Gavioli, Robert I Killey, and Polina Bayvel. Electronic compensation of chromatic dispersion using a digital coherent receiver. *Optics express*, 15(5):2120–2126, 2007.

[222] John R Barry, Edward A Lee, and David G Messerschmitt. *Digital communication*. Springer Science & Business Media, 2012.

[223] Steven Gringeri, Bert Basch, Vishnu Shukla, Roman Egorov, and Tiejun J Xia. Flexible architectures for optical transport nodes and networks. *IEEE Communications Magazine*, 48(7):40–50, 2010.

[224] Curtis R Menyuk and Brian S Marks. Interaction of polarization mode dispersion and nonlinearity in optical fiber transmission systems. *Journal of Lightwave Technology*, 24(7):2806–2826, 2006.

[225] Ian H Malitson. Interspecimen comparison of the refractive index of fused silica. *Josa*, 55(10):1205–1209, 1965.

[226] Pratim Hazarika, Mingming Tan, Aleksandr Donodin, Shabnam Noor, Ian Phillips, Paul Harper, Jeffery S Stone, Ming Jun Li, and Wladek Forysiak. E-, s-, c-and l-band coherent transmission with a multistage discrete raman amplifier. *Optics Express*, 30(24):43118–43126, 2022.

[227] Alessio Ferrari, Emanuele Virgillito, and Vittorio Curri. Band-division vs. space-division multiplexing: a network performance statistical assessment. *Journal of Lightwave Technology*, 38(5):1041–1049, 2020.

[228] Antonio Napoli, Nicola Calabretta, Johannes K Fischer, Nelson Costa, Silvio Abrate, Joao Pedro, Victor Lopez, Vittorio Curri, Darko Zibar, Erwan Pincemin, et al. Perspectives of multi-band optical communication systems. In *2018 23rd Opto-Electronics and Communications Conference (OECC)*, pages 1–2. IEEE, 2018.

[229] Victor Lopez, Benyuan Zhu, Daniela Moniz, Nelson Costa, Joao Pedro, Xian Xu, Ales Kumpera, Lee Dardis, Jeff Rahn, and Steve Sanders. Optimized design and challenges for C&L band optical line systems. *Journal of Lightwave Technology*, 38(5):1080–1091, 2020.

[230] Hanan A Alkhidhr. Closed-form solutions to the perturbed nlse with kerr law nonlinearity in optical fibers. *Results in Physics*, 22:103875, 2021.

[231] Zaiyun Zhang and Jianguo Wu. Generalized (*G*'/*G*)-expansion method and exact traveling wave solutions of the perturbed nonlinear schrödinger's equation with kerr law nonlinearity in optical fiber materials. *Optical and Quantum Electronics*, 49:1–15, 2017.

[232] Dimitris Uzunidis, Chris Matrakidis, A Stavdas, and Andrew Lord. Power optimization strategy for multi-band optical systems. In *2020 European Conference on Optical Communications (ECOC)*, pages 1–4. IEEE, 2020.

[233] Matthias Gunkel, Arnold Mattheus, Felix Wissel, Antonio Napoli, João Pedro, Nelson Costa, Talha Rahman, Gianluca Meloni, Francesco Fresi, Filippo Cugini, et al. Vendor-interoperable elastic optical interfaces: Standards, experiments, and challenges. *Journal of Optical Communications and Networking*, 7(12):B184–B193, 2015.